UNIVERSITY OF CALIFORNIA SAN DIEGO

Dynamics of the Southern Ocean from observations in Drake Passage

A dissertation submitted in partial satisfaction of the
requirements for the degree
Doctor of Philosophy

in

Oceanography

by

Manuel Othon Gutierrez Villanueva

Committee in charge:

Teresa K. Chereskin, Co-Chair
Janet Sprintall, Co-Chair
Sarah T. Gille
Jennifer MacKinnon
Sarah Purkey
Sutanu Sarkar

2022

The dissertation of Manuel Othon Gutierrez Villanueva is approved, and it is acceptable in quality and form for publication on microfilm and electronically.

University of California San Diego

2022

DEDICATION

To my parents, Amelia and Felix,

and my siblings Felix Gilberto and Claudia Amelia,

for their support, patience and love.

EPIGRAPH

I wish it need not have happened in my time, said Frodo.

So do I, said Gandalf, *and so do all who live to see such times.*

But that is not for them to decide.

All we have to decide is what to do with the time that is given us.

—J.R.R. Tolkien, *The Fellowship of the Ring*

TABLE OF CONTENTS

LIST OF FIGURES

LIST OF TABLES

ACKNOWLEDGEMENTS

First, I want to thank my co-advisors, Teri Chereskin and Janet Sprintall for their valuable support and guidance in both academics and life. Their wisdom, patience, advice, and encouragement have allowed to develop my own scientific creativity and articulate and organize my ideas in a very succinct way. I will never forget when I use to say *this will be a short meeting* and we end up spending a couple of hours.

I gratefully appreciate the scientific discussion and advice from my committee members, Sarah Gille, Sarah Purkey, Jennifer Mackinnon, and Sutanu Sarkar. Their valuable time, comments, and questions regarding my thesis work and professional career. Their work ethics and professional career are an example of success in academia which I shall follow.

To all my professors at SIO for shedding their expertise and knowledge in the field which has made me a better scientist. Special acknowledgment goes to Dan Rudnick who I had the privilege to work for him as TA; I have drawn inspiration from his teaching style and work ethic.

To the PO-CS 2015 cohort, thanks for the fun and not-so-fun times spent in our first year in NH301. I am really in debt to my friends in Mexico for their support throughout my life. The invaluable time I spent with my housemates Andre, May-Linn, Lara, Amalia, Arash, Gregor, Hereroa, Michelle, and Anthony. Thanks for all the good times, especially during the pandemic, watching sports and series, cooking, socializing, outdooring, etc. To the Kelp Forest Experiment team, Noel, Bethan and Alex, for all the hours we share preparing and executing our experiment. Matthew Alford and Uwe Send deserve recognition for their guidance and enthusiasm in the Kelp Forest experiment. Additionally, all the awesome people I met during the sCONE and S4P cruises deserve to be mentioned.

To the SIO department, especially to Gilbert Bretado, Tomomi Ushii, Shelley Weisel, Will Rivera, Maureen McGreevy, and Di Chen. To the RV R.G. Sproul and RVIB Nathaniel B. Palmer crews for making the cruises happen and all the scientific crew involved in collecting the ancillary data used for this thesis and other experiments.

Words are not enough to thank Dr. Alejandro Cruz Rosas and Dr. Maricela Ortega. I am indebted for all the guidance, support, and words of relief you provided during the last year of my PhD.

Finally, I thank my family who has been there for me even in the most difficult times. I am proud of you and every single goal you have accomplished.

My research and education were funded by the National Council for Science and Technology (Conacyt), UC Mexus, the National Science Foundation, and UC Ship Funding programs.

Chapter 2, in full, is a reprint of the material as it appears in Gutierrez-Villanueva, Manuel O., Teresa K. Chereskin, and Janet Sprintall (2020). Upper-Ocean Eddy Heat Flux across the Antarctic Circumpolar Current in Drake Passage from Observations: Time-Mean and Seasonal Variability, Journal of Physical Oceanography 50, 9: 2507-2527, https://doi.org/10.1175/JPO-D-19-0266.1. The dissertation/thesis author was the primary researcher and first author.

Chapter 3, in full, is a reprint of the material as it appears in Gutierrez-Villanueva, M. O., Chereskin, T. K., Sprintall, J., and Goff, J. A. (2022). Turbulent mixing and lee-wave radiation in Drake Passage: Sensitivity to topography. Journal of Geophysical Research: Oceans, 127, e2021JC018103, https://doi.org/10.1029/2021JC018103. The dissertation/thesis author was the primary investigator and author of this paper.

Chapter 4, in part, is currently being prepared for submission for publication of the material. Gutierrez-Villanueva M. O., T. K. Chereskin and J. Sprintall. The dissertation/thesis author was the primary investigator and author of this material.

VITA

2010	B. S. in Oceanography, Universidad Autonoma de Baja California, Ensenada, Mexico
2013	M. S. in Physical Oceanography, Centro de Investigacion Cientifica y Estudios Superiores de Ensenada (CICESE), Mexico.
2022	Ph. D. in Oceanography, University of California San Diego

PUBLICATIONS

Gutierrez-Villanueva, M. O., Chereskin, T. K., Sprintall, J., and Goff, J. A. (2022). Turbulent mixing and lee-wave radiation in Drake Passage: Sensitivity to topography. Journal of Geophysical Research: Oceans, 127, e2021JC018103, https://doi.org/10.1029/2021JC018103.

Gutierrez-Villanueva, Manuel O., Teresa K. Chereskin, and Janet Sprintall (2020). Upper-Ocean Eddy Heat Flux across the Antarctic Circumpolar Current in Drake Passage from Observations: Time-Mean and Seasonal Variability, Journal of Physical Oceanography 50, 9, 2507-2527, https://doi.org/10.1175/JPO-D-19-0266.1.

Gutiérrez, Manuel O., Manuel López, Julio Candela, Rubén Castro, Affonso Mascarenhas, and Curtis A. Collins (2014). Effect of coastal-trapped waves and wind on currents and transport in the Gulf of California. Journal of Geophysical Research: Oceans, 119 (8), 5123-5139, doi: https://doi.org/10.1002/2013JC009538.

ABSTRACT OF THE DISSERTATION

Dynamics of the Southern Ocean from observations in Drake Passage

by

Manuel Othon Gutierrez Villanueva

Doctor of Philosophy in Oceanography

University of California San Diego, 2022

Teresa K. Chereskin, Co-Chair
Janet Sprintall, Co-Chair

The Antarctic Circumpolar Current (ACC) and the Southern Ocean meridional overturning circulation are dynamically linked through interactions between the mean flow, eddies, and mixing by breaking internal lee waves over rough topography. However, quantifying the time-mean and the spatio-temporal variability of the ACC transport, eddy fluxes, and small-scale mixing remains challenging as observations are scarce. This thesis work analyzes the mean eddy heat flux, finescale internal-wave-driven turbulence, and transport of the ACC in Drake Passage, and it examines the possible physical processes driving the spatial and temporal variability of these quantities.

First, the eddy heat flux as a function of ACC streamlines is quantified using a unique 20-year time series of upper ocean temperature and velocity transects with unprecedented horizontal resolution. Using the time-varying streamlines, the across-ACC eddy heat flux is maximum poleward in the south flank of the Subantarctic Front and it reduces towards the south, becoming statistically insignificant in the Polar Front. These results indicate heat convergence south of the Subantarctic Front.

Second, a unique four-year time series of stratification and near-bottom currents, and finestructure density and velocity profiles were employed to estimate the expected linear lee-wave energy and infer turbulent dissipation due to breaking internal waves. In contrast to idealized numerical predictions of 50% local dissipation of lee-wave energy, less than 10% dissipated locally regardless of the abyssal hill topographic representation.

Third, the high-spatial-resolution time series of temperature, salinity, and velocity are used to identify trends in the Drake Passage total and geostrophic transport in the upper kilometer. We uniquely found that the Subantarctic Front and Polar Front, the two major ACC fronts, have significantly accelerated during the last decade whereas the area between these fronts and between the Polar Front and the Southern ACC Front has decelerated. These opposite trends compensate such that no significant trend is discernible in the total and geostrophic transport integrated across Drake Passage. We suggest the acceleration of the fronts is driven by an increase in the eddy activity in between the fronts.

Chapter 1

Introduction

The Southern Ocean (SO), the ocean south of 40 °S, is especially sensitive to changing climate. For instance, ocean temperatures have warmed significantly more than the global ocean over the past several decades [Böning et al., 2008; Gille, 2002, 2008; Shi et al., 2021]. Recent studies point out that the increase ocean temperatures in the SO have increased mainly due to increasing in the heat uptake of the ocean from the atmosphere. Similarly, observations in the SO show intensified westerly winds associated with a positive trend of the southern annular mode (SAM) index [Fay et al., 2014; Marshall and Shutts, 1981], the leading mode of atmospheric variability in the SO, in response to both depletion of the atmospheric ozone and increase in the greenhouse gas emissions over the last decades. Additionally, recent studies have found freshening at circumpolar scales from intermediate waters (2000 m) to the surface since 1950 that has impacted the stratification in the SO [Durack and Wijffels, 2010; Swart et al., 2018]. These complex sets of forcing and changes have profound implications for the global climate and ice melting, thus sea level rise. Hence, understanding how the SO is responding to these changes is paramount to understand future scenarios.

The SO has two circulation patterns: 1) the Antarctic Circumpolar Current (ACC), and 2) the meridional overturning circulation (Fig. 1.1). The ACC flows from west to east unbounded

around Antarctica and navigates through Drake Passage, the narrowest continental choke point in the SO. The ACC is composed of multiple fronts which mark boundaries between different water masses separated by velocity jets. The fact that the wind-driven ACC flows unbounded allows the fronts to extend vertically to almost the ocean floor. The ACC fronts' tilted isopycnals store potential energy that is released through baroclinic instabilities, which feeds into the vigorous eddy field [Rintoul, 2018]. On the other hand, the SO overturning circulation refers to the meridional flow of dense deep and bottom waters away from their sources and a compensating return flow of less dense upper-ocean waters. Two major meridional overturning circulation cells are found in the SO: the upper cell comprises the surface northward Ekman transport balanced by the deep poleward eddy flow along isopycnals. Below the upper cell, dense waters formed by air-sea heat and salt/freshwater fluxes over the Antarctic continental shelf sink and flow over the shelf breaks. The dense water moves through the ocean's abyssal basins and is returned to the deep and intermediate waters through turbulent mixing across density layers. Eddy fluxes, Ekman transport, and turbulent mixing act at different depths and transport different water masses. Both the ACC and the overturning circulation redistribute heat, freshwater, gases, and nutrients throughout the global oceans and play a fundamental role in the global climate. Quantifying eddy fluxes, turbulent mixing and the ACC transports, and their spatial-temporal variability requires densely sampled and simultaneous observations.

Overall the SO is a meagerly sampled section of the global oceans as it represents a challenge to observe due to inhospitable conditions and remoteness; the investigation of the processes driving the overturning circulation components and changes in the ACC temperature and salinity structure remains challenging as observations are scarce. However, Drake Passage has been the subject of several oceanographic campaigns during the last 30 years, e.g. the Laurence M. Gould (LMG) time series and the World Ocean Circulation Experiment (WOCE), Climate and Ocean Variability, Predictability, and Change (CLIVAR), and Global Ocean Ship-based Hydrographic Investigations Program (GO-SHIP) repeated hydrography transects. Of particular

note, the 20-year-long LMG time series is a unique sampling mode with *unprecedented* temporal and spatial resolution on the order of the first baroclinic Rossby radius ($\leq O(10)$ km) in the SO. These observations provide an opportunity to characterize the mean and eddy temperature and velocity fields with statistical significance. With the aid of these time series along with supplementary observational data, this thesis work analyses the mean eddy heat flux, internal-wave-driven turbulent mixing, and transport of the ACC in Drake Passage, and examines the possible physical processes and factors driving the spatial and temporal variability of these quantities.

Eddy heat flux plays a fundamental role in the SO meridional overturning circulation, providing the only mechanism for poleward heat transport below the Ekman layer at the latitudes of Drake Passage. However, quantifying this heat transport along with its spatial distribution and temporal variability remain open questions. Chapter 2 of this thesis employs the 20-year-long time series of upper-ocean temperature and velocity to estimate the time-mean eddy heat flux across the ACC as a function of the ACC fronts by employing two frameworks: time-mean and time-varying (mean plus daily maps of sea surface height) streamline. Moreover, this chapter analyzes which of these frameworks provides the best estimate for the across-stream eddy heat flux component, that is, the component that yields the net eddy heat flux that results only from the horizontally divergent component [Marshall and Shutts, 1981]. We compare our estimates to historical eddy heat flux estimates in the ACC [e.g. Lenn et al., 2011; Phillips and Rintoul, 2000; Sekma et al., 2013; Watts et al., 2016]. The time series also provides the unique opportunity to explore the seasonal cycle of the eddy heat flux.

Chapter 3 studies the relationship between internal lee-wave energy radiation and turbulent mixing due to breaking internal waves near the bottom. Radiation and breaking of internal lee waves (waves locked in phase generated in the lee of rough topography) are thought to play a significant role in the energy and heat budget of the SO. Of particular interest is to quantify the amount of lee-wave energy from the near-bottom geostrophic ACC flow that dissipates locally.

To quantify this, linear lee-wave theory [Bell Jr, 1975] is estimated using a unique four-year time series of stratification and near-bottom currents from an array of Current and Pressure measuring Inverted Echo Sounders [CPIES; Tracey et al., 2013]. Finestructure temperature, salinity, and velocity profiles at CPIES locations were used to estimate turbulent mixing by breaking internal waves using a finescale parameterization [Polzin et al., 2014]. Previous authors [Trossman et al., 2015; Yang et al., 2018] suggested that estimates of lee-wave energy radiation and near-bottom turbulent dissipation in the ACC potentially come to a close agreement by employing a two-dimensional anisotropic abyssal hill topography. This thesis work tests this hypothesis by estimating energy radiation by employing a two-dimensional anisotropic abyssal hill topography [Goff, 2020].

Drake Passage has historically provided an ideal location for monitoring the ACC transport as it represents the narrowest constriction through which the ACC flows. Drake Passage transport serves as a valuable metric for validating ocean and climate models. Whether the Drake Passage transport has accelerated over the last decades and what physical mechanisms drive this possible trend remain unclear. Using the Argo database in combination with the geostrophic velocities from altimetry, Shi et al. [2021] find a small, but significant acceleration of the upper 1500 m currents in the SO north of the Subantarctic Front over the last 15 years. Nonetheless, the authors do not find an acceleration of the Drake Passage transport, similar to observations in Drake Passage that did not find acceleration of the Drake Passage transport [Chidichimo et al., 2014; Cunningham et al., 2003; Koenig et al., 2014]. Chapter 4 estimates trends in the Drake Passage transport for the last two decades. To do this, the high-along-track resolution time series of velocity, temperature, and salinity were employed to estimate time series of total and geostrophic (referenced to 760 m) velocity, hence, transport. Here we argue that the trend in the transport integrated across Drake Passage shows no significant trend, as opposing regional trends within the Drake Passage are found to compensate. We estimate trends in the geostrophic and total transport integrated across Drake Passage, and as a function of the ACC fronts. The temperature

and salinity transects are used to understand how the baroclinic structure of the ACC across Drake Passage has changed, and how it relates to the trends in total velocity.

Finally, Chapter 5 draws out the significance of the major contributions of this thesis work and brings forward the remaining questions that deserve further investigation.

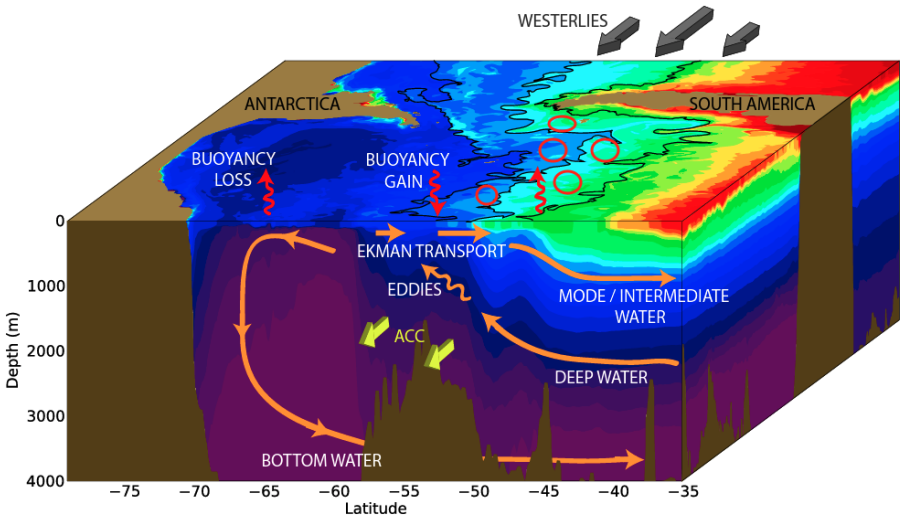

Figure 1.1: A schematic of the Southern Ocean main circulation patterns adapted from Morrison et al. [2015]. Gray thick arrows show the westerly wind stress over the Southern Ocean. The heavy yellow arrows denote the eastward flow of the Antarctic Circumpolar Current. The overturning circulation is indicated by orange arrows, with wavy arrows intended to represent transport by eddies. The meridional transport is largely along layers of constant density, represented by the colored surfaces. Vertical curly red arrows at the sea surface indicate air–sea buoyancy exchange (upward arrows mean a buoyancy loss by the ocean). Red ovals show mesoscale eddies within the ACC fronts (black contours).

Chapter 2

Eddy heat flux across the Antarctic Circumpolar Current

2.1 Abstract

Eddy heat flux plays a fundamental role in the Southern Ocean meridional overturning circulation, providing the only mechanism for poleward heat transport above the topography and below the Ekman layer at the latitudes of Drake Passage. Models and observations identify Drake Passage as one of a handful of hot spots in the Southern Ocean where eddy heat transport across the Antarctic Circumpolar Current (ACC) is enhanced. Quantifying this transport however, together with its spatial distribution and temporal variability, remain open questions. This study quantifies eddy heat flux as a function of ACC streamlines using a unique 20-year time series of upper ocean temperature and velocity transects with unprecedented horizontal resolution. Eddy heat flux is calculated using both time-mean and time-varying streamlines to isolate the dynamically important across-ACC heat flux component. The time-varying streamlines provide the best estimate of the across-ACC component because they track the shifting and meandering of the ACC fronts. The depth-integrated (0-900 m) across-stream eddy heat flux is maximum

poleward in the south flank of the Subantarctic Front (-0.10 ± 0.05 GW m^{-1}) and reduces towards the south, becoming statistically insignificant in the Polar Front, indicating heat convergence south of the Subantarctic Front. The time series provides an uncommon opportunity to explore the seasonal cycle of eddy heat flux. Poleward eddy heat flux in the Polar Front Zone is enhanced during austral fall-winter, suggesting a seasonal variation in eddy-driven upwelling and thus the meridional overturning circulation.

2.2 Introduction

The Southern Ocean meridional overturning circulation plays a fundamental role in the global climate and transfers heat, salt, and biochemical tracers across the eastward-flowing Antarctic Circumpolar Current (ACC). Meridional transport in the Southern Ocean requires crossing the intense zonal ACC jets that represent strong physical barriers for the cross-frontal exchange of particles or tracers. Eddies break these barriers by flattening the isopycnals and weakening the potential vorticity gradients, allowing particles to cross the fronts. In particular, eddy-driven heat transport provides the sole mechanism for poleward heat transport at depths above submerged topography at the latitudes of Drake Passage [e.g. Meredith et al., 2011, and references in there]. This poleward heat transport balances the surface northward Ekman heat transport and air-sea heat fluxes. Quantifying the amount of heat transferred poleward by eddies, therefore, is crucial for understanding the Southern Ocean heat budget.

Although the classical zonally-averaged theory has provided many insights into ACC dynamics [Marshall and Radko, 2003], the Southern Ocean and the ACC are highly heterogeneous. Satellite altimetry, numerical models and the global array of Argo floats reveal that the distribution of eddy activity is concentrated in a handful of eddy hot spots downstream of abrupt bottom topography and in western boundary currents [e.g. Abernathey and Cessi, 2014; Chapman and Sallée, 2017; Foppert et al., 2017; Thompson and Naveira Garabato, 2014]. Direct eddy heat flux

estimates in these hot spots [Bryden, 1979; Ferrari et al., 2014; Lenn et al., 2011; Nowlin Jr. et al., 1985; Phillips and Rintoul, 2000; Walkden et al., 2008; Watts et al., 2016], enable understanding of the contribution of the eddies to the meridional overturning circulation but leave open the question of how representative these estimates are for the Southern Ocean. Neutrally buoyant floats [Gille, 2003] and Argo floats [Chapman and Sallée, 2017] have provided global eddy heat flux estimates in the Southern Ocean, but the coarse temporal and spatial sampling smooths the spatial distribution and reduces the magnitude of these heat flux estimates. Overall, quantifying the amount of heat transported by eddies across the ACC requires densely sampled and simultaneous velocity and temperature observations to obtain statistically significant estimates, which remains a challenge as these types of observations in the Southern Ocean are scarce.

A problematic aspect of the eddy heat flux calculation is that net flux results only from the horizontally divergent component. As discussed by Marshall and Shutts [1981], the eddy heat flux vector can be decomposed into the sum of two components: a rotational component that circulates around eddy potential energy contours and a divergent component that represents the dynamically-important net down-gradient heat flux. Neglecting the distinction between rotational and divergent components can erroneously indicate a higher rate of baroclinic conversion of potential to kinetic energy than is present. Nevertheless, reducing the rotational component from observations remains nontrivial. Several authors have used different methods to calculate the divergent component. For instance, Lenn et al. [2011] used a time-mean streamwise coordinate system to estimate the across-stream eddy heat flux component from 7 years of along-track temperature and current velocity observations in Drake Passage. Phillips and Rintoul [2000] used daily shear-coordinates to isolate the across-stream component from an array of four current meter moorings deployed for 2 years south of Tasmania. Following Marshall and Shutts [1981], Cronin and Watts [1996] estimated the divergent component in the Gulf Stream as the residual of the eddy heat flux vector projected along temperature variance contours minus the total eddy heat flux vector. Bishop et al. [2013] showed that the barotropic (depth independent; in this case,

near-bottom current) component naturally captures the full divergent component with a small rotational residual in the Kuroshio Extension. Watts et al. [2016] applied this technique in Drake Passage; they concluded that baroclinic instabilities were the leading mechanism for the large heat flux events that occurred when the barotropic component crossed the baroclinic component at an angle resulting in a deviation from the vertically-aligned equivalent barotropic flow. Their 4-year time series captured these short 4-6 day events and produced stable estimates over 2-year subsets. However, their results have a spatial resolution of 40-60 km, coarser than the first baroclinic Rossby radius (20-10 km) at that latitude range [Chelton et al., 1998]. Foppert et al. [2017] used 23 years of altimetric sea surface height (SSH) variance as a proxy for downgradient eddy heat flux, but again the SSH maps have coarse spatial resolution $O(100)$ km.

Mesoscale eddies contribute to the stratification and ventilation of the thermocline in the Southern Ocean. However, the magnitude of their contribution to the seasonal variation of the upper-ocean heat content is not well understood. Recent studies in Drake Passage from observations showed that half of the variance of the seasonal upper-ocean heat content is explained by the air-sea heat fluxes [Stephenson et al., 2012] which, combined with the eddy advection and interannual variability, accounted for $\sim 84\%$ of the variance [Stephenson et al., 2013]. Since the air-sea heat fluxes account for most of the seasonal variability of the upper-ocean heat content in Drake Passage, the implication is that the contribution of mesoscale eddies plays a minimal role. However, air-sea flux products are poorly constrained in the Southern Ocean due to the severe undersampling compared to other regions of the world oceans. Also, eddy heat diffusion and advection processes could potentially play an important role in the Southern Ocean eddy hot spots. The lack of long-term observations in these regions impedes us from understanding the potential role of eddies in the seasonal variations of the upper ocean heat budget.

Drake Passage is a known hot spot of eddy activity [e.g. Thompson and Naveira Garabato, 2014; Thompson and Sallée, 2012]. In this study, we use a unique 20-year time series of nearly-repeated upper-ocean temperature and velocity transects in Drake Passage with an unprecedented

spatial resolution of the order of the first baroclinic Rossby radius. These observations provide an opportunity to characterize both the mean and eddy temperature and velocity fields with statistical significance. The eddy heat flux across the ACC within Drake Passage is estimated relative to the position of the major ACC fronts. Lenn et al. [2011] previously calculated the time-mean eddy heat flux using the Drake Passage temperature and velocity transects over the upper 250 m depth range for the period September 1999 to October 2006. In this paper, we extend the Lenn et al. [2011] estimates both in depth (to 900 m) and in time (September 1999 to December 2014). Furthermore, in addition to a time-mean streamwise coordinate system [Lenn et al., 2011], we also adopt a time-varying, synoptic streamwise coordinate system to decompose the eddy heat flux vector into the rotational along-stream component and the divergent across-stream component; it is the divergent component that represents the true net heat flux across the ACC. The synoptic coordinate system combined with the high spatial resolution of the Drake Passage transects allows the study of the effect of the shifting and meandering of the ACC fronts on the cross-frontal eddy heat flux. Finally, the 20-year time series uniquely enables us to estimate the mean eddy kinetic energy (EKE) and to explore the seasonality of the eddy heat flux and EKE relative to the position of the ACC fronts.

Our results focus on the across-stream eddy heat flux which gives rise to a local net poleward heat transport from eddies. We also present the along-stream eddy heat flux to gauge its magnitude in comparison to the across-stream component. The along-stream component is thought to be dynamically unimportant because it recirculates heat along the re-entrant path of the ACC. This path is not purely zonal, however; the ACC traverses hundreds of kilometers meridionally as it travels from its southernmost point at about 65°S in the Southeast Pacific to its northernmost point at about 45°S in the Brazil-Malvinas Confluence. The ACC temperature changes along this path, with warming across the Confluence and along the Agulhas Extension and cooling along the high-latitude Pacific segment; consequently warm and cold waters advect respectively poleward and equatorward, with negligible meridional mass transport, resulting in a

net poleward heat transport [Sun and Watts, 2002]. Air-sea interaction and mesoscale eddies play essential roles in changing the along-path ACC temperature. The along-stream eddy heat flux contributes to this larger-scale ACC heat transport.

2.3 Data sets

2.3.1 The Drake Passage observations

Underway upper-ocean velocity and temperature were collected aboard the Antarctic Research and Supply Vessel (ARSV) Laurence M. Gould (LMG) that transits between South America and the Antarctic Peninsula (Fig. 2.1). Details of the different data sets can be found in Table 2.1. In this study, we use the 150 kHz Acoustic Doppler Current Profiler (ADCP; NB150) time series which has been described by Lenn et al. [2007]. In summary, starting in September 1999 the NB150 time series provides velocity measurements in the upper 300 meters at 8-m vertical resolution. In addition, since November 2004 a 38 kHz ADCP (OS38) started sampling velocity at a vertical resolution of 24 m extending to 1222-m depth. Here we use only the upper 900-m and 250-m since the velocity profiles are gappier below this depth for the OS38 and NB150 ADCP, respectively; also, the temperature data only spans the upper 890 m (described below). From September 1999 - December 2014, 326 NB150 and 204 OS38 ADCP transects are available (Table 2.1). In contrast, Lenn et al. [2011] used 156 NB150 velocity transects.

Velocity data were processed using the Common Ocean Data Access System (CODAS) software [Firing et al., 2012]; velocities were transformed from ship-relative to absolute ocean currents using the GPS position and attitude measurements. Because the sonar wells are filled with an antifreeze mixture, a speed of sound correction is made using measured sound velocity from a probe mounted in the NB150 well. The OS38 uses a phased array transducer that does not require a sound speed correction. The OS38 does, however, require an additional correction to account for residual ADCP transducer misalignment that we estimated from minimizing transport

bias as in Firing et al. [2011]. The absolute velocity is averaged over 300 seconds corresponding to $\sim$5 km along-track horizontal resolution. Barotropic tidal currents were removed from the absolute velocity by subtracting the tidal prediction of the TPXO7.2 tide model [Egbert et al., 1994]. Baroclinic tides and ageostrophic Ekman currents were not removed from the velocity data as they have relatively small amplitudes $< O(10)$ cm s^{-1} in Drake Passage [Lenn et al., 2007; Lenn and Chereskin, 2009]; moreover, it is impractical to remove these flows within uncertainty for each transect.

On 6-7 LMG transects per year, 70 eXpendable Bathythermograph (XBT) probes were deployed that measure temperature in the upper 900-m (Table 2.1). The temperature profiles were averaged to 10-m depth bins. The spatial resolution is 6-10 km across the Subantarctic Front (SAF) and Polar Front (PF), and 10-15 km elsewhere [Sprintall, 2003]. All data were quality-controlled, and following Hanawa et al. [1995], the XBT data were corrected for the systematic fall rate error. Overall, there are 130 XBT transects from September 1996 - December 2016 that were used to calculate the time-mean temperature fields; 63 of these surveys coincide with the OS38 ADCP transects from November 2004 to December 2014, and 108 with the NB150 from September 1999 to December 2014. Lenn et al. [2011] used 38 concurrent XBT and NB150 velocity transects between September 1999 and October 2004.

2.3.2 Remotely sensed data

In this study we estimate the time-mean geostrophic streamfunction $\overline{\Psi}$ and the synoptic coordinate system Ψ^* using the SSALTO/DUACS daily maps of sea surface height (SSH) anomaly, objectively mapped from multiple satellite altimeters to a $0.25^{\circ} \times 0.25^{\circ}$ Cartesian grid, produced and distributed by the Copernicus Marine and Environmental Monitoring Service [CMEMS; Ducet et al., 2000]. The SSH anomalies are relative to a twenty-year mean of the sea surface height field. We only consider the SSH anomalies from September 1999 to December 2014, which covers our period of interest. We also use the Mean Dynamic Topography from Maximenko

et al. [2009] derived from a combination of 20 years of satellite altimetry, gravity measurements, and *in-situ* data.

2.4 Methods

2.4.1 Estimating mean temperature, and geostrophic velocity and streamfunction

The geographic coordinate system was rotated 24° counterclockwise to establish an along/across Drake Passage coordinate system. The area enclosed by the most repeated transects (Fig. 2.1) was gridded into horizontal boxes with a 25 km $\times$ 25 km resolution as in Lenn et al. [2011] and Firing et al. [2011]. The grid was employed for calculating the mean velocity and temperature fields at each depth bin.

For the mean velocity, the surface geostrophic velocity anomalies calculated from the daily SSH maps were subtracted from the ADCP velocities at each depth to reduce the eddy aliasing [Firing et al., 2011; Lenn et al., 2008]. The ADCP velocities from each transect were then averaged within the Drake Passage grid to produce one velocity profile per occupied grid box per transect. The velocity profiles in each grid were then averaged over all cruises to produce a record-length mean velocity profile per grid box. In the upper 24 m (42 m) where the NB150 (OS38) ADCP did not sample, a slab layer was assumed.

To calculate the Drake Passage mean geostrophic streamfunction $\overline{\Psi}$ and velocities $\overline{\mathbf{u}}$, we followed Firing et al. [2011] and Lenn et al. [2008]. The objective mapping constrained the mean velocity profiles and streamfunction to satisfy the geostrophic continuity relationship (i.e. $\nabla_h \cdot f\mathbf{U} = 0$, where f is the Coriolis parameter and $\mathbf{U}$ is the total velocity vector). First, the background-mean geostrophic velocities were calculated by taking spatial gradients from the Maximenko et al. [2009] mean dynamic topography and removing them from the mean velocity

profiles. The anomalies were objectively mapped assuming a Gaussian covariance function and an isotropic decorrelation scale of 70 km [Firing et al., 2014; Lenn et al., 2008] and a noise-to-signal ratio of 0.2. The decorrelation scales were varied by ± 15 km and the noise-to-signal ratio by ± 0.1, but the mapped geostrophic streamlines and velocities were not sensitive to these changes. A smaller decorrelation scale potentially affects the mapping error in the southern Drake Passage area ($y < -500$ km) where gaps between transects widen in the down-passage ($x-$axis) orientation. The mean dynamic topography from Rio and Hernandez [2004] was also tested, but the mapped mean streamfunction and velocities were insensitive to the choice of the background mean, as also noted by Firing et al. [2011]. Finally, the mean geostrophic streamfunction and velocities from the Maximenko et al. [2009] dynamic topography were added back to the mapped geostrophic streamfunction and velocity anomalies.

The same along/across Drake Passage 25 km $\times$ 25 km grid boxes used to construct the mean ADCP profiles were also used to calculate the mean temperature fields $\overline{T}$. All 130 XBT transects from September 1996 to December 2016 were used to construct the mean. Temperature profiles were first linearly interpolated to the same ADCP depth bins and for each grid box averaged by transect and then over the complete time period.

2.4.2 Estimating streamwise-averaged eddy heat flux

Temperature fluctuations T' were calculated at the location of each temperature profile T by removing the gridded time-mean temperature estimated for the grid box that contains the individual temperature profile: $T'(x,y,z,t) = T(x,y,z,t) - \overline{T}(x_g,y_g,z)$, where (x_g,y_g) correspond to the temperature profile's 25 km $\times$ 25 km grid box. Similarly, velocity fluctuations $\mathbf{u}'$ were obtained by removing their corresponding objectively-mapped time-mean geostrophic velocity vector $\overline{\mathbf{u}}$ from the instantaneous velocity vector $\mathbf{u}$ profile $\mathbf{u}'(x,y,z,t) = \mathbf{u}(x,y,z,t) - \overline{\mathbf{u}}(x_g,y_g,z)$.

Using the Drake Passage transect data, it is infeasible to decompose the eddy heat flux vector $\mathbf{u}'T'$ into rotational and divergent components following the method of Marshall and

Shutts [1981]. Instead, we use streamwise components for the heat flux decomposition. In a truly instantaneous streamwise coordinate system, the along stream $u'T'_{\Psi}$ contains all of the rotational component while the across-stream $v'T'_{\Psi}$ contains all of the divergent component, i.e., $v'T'_{\Psi}$ represents the net eddy heat flux across the ACC. However, the synoptic streamlines that we use are approximations to the true instantaneous streamlines at the time and location of the observations. We assume that the across-stream eddy heat flux component contains most of the divergent eddy heat flux plus some rotational residual. Likewise, the along-stream component contains most of the rotational eddy heat flux plus some divergent residual.

Time-mean streamwise coordinate system $\overline{\Psi}$

To obtain the streamwise-averaged eddy heat flux components using the time-mean coordinate system, we contoured $\overline{\Psi}$ at every depth with a streamline spacing of $\Delta\overline{\Psi} = 0.05$ m; the streamlines were selected between the maximum and minimum $\overline{\Psi}$ values (-0.575 m and -1.625 m, respectively) that can be mapped at the deepest bin (886 m) and are delimited by the 500-m isobath in the across Drake Passage direction (Fig. 2.2). Next, the individual velocity and temperature data positions that fell within a specific pair of streamlines $\overline{\Psi}_j$ and $\overline{\Psi}_{j+1}$ were determined for all transects, where $j = 1,\ 2, \cdots,\ M-1$ (M is the total number of open streamlines; $\overline{\Psi}_{j=1}$ is the northernmost streamline and $\overline{\Psi}_{j+1} = \overline{\Psi}_j - \Delta\overline{\Psi}$). Subsequently, for each individual temperature data location, the closest individual velocity data position was determined and the eddy heat flux vector was calculated and assigned to the temperature data position. The normal vector $\hat{\mathbf{n}} = \nabla\overline{\Psi}/|\nabla\overline{\Psi}|$ was bilinearly interpolated to the individual heat flux positions and the eddy heat flux vector rotated to an angle $\theta = \theta_{\hat{\mathbf{n}}} - \frac{\pi}{2}$, where $\theta_{\hat{\mathbf{n}}}$ represents the angle of the normal vector measured from the $+x$ axis. Using this rotation the along-stream and across-stream components are $u'T'_{\overline{\Psi}}$ and $v'T'_{\overline{\Psi}}$, respectively. Components were streamwise averaged at each depth per streamline for each transect. To obtain mean eddy heat flux estimates ($\overline{u'T'}_{\overline{\Psi}}, \overline{v'T'}_{\overline{\Psi}}$), each component per transect per streamline was averaged by combining all the available Drake

Passage transects. The standard errors $\hat{\sigma}$ were calculated for each eddy heat flux component as $\hat{\sigma} = \sigma/\sqrt{N}$ where σ and N are the standard deviations of each component and the number of degrees of freedom, respectively. Each concurrent temperature and velocity transect was assumed to represent one degree of freedom [Lenn et al., 2011].

Time-varying streamwise coordinate system Ψ^*

To estimate the effect of the temporal shifting of the ACC geostrophic streamlines in the eddy heat flux calculation (Fig. 2.2), a time-varying streamwise coordinate system Ψ^* was adopted. Ψ^* allowed us to track both the position of the ACC fronts and the orientation of the flow. We expanded the domain beyond that of $\overline{\Psi}$ and $\overline{T}$ (area enclosed by most repeated transects; filled contours in Fig. 2.2). The expanded domain allowed us to distinguish open streamlines from closed contours that might represent eddies (solid contours, Fig. 2.2). The synoptic streamlines were calculated as $\Psi^* = \overline{\Psi}^0_{-250} + \Psi^{ssh}$, where Ψ^{ssh} is an SSH anomaly map averaged over a 5-day window centered at the mean date of each transect and $\overline{\Psi}^0_{-250} = \frac{1}{250}\int_{-250}^{0} \overline{\Psi} dz$ is the objectively mapped mean streamfunction depth-averaged over the upper 250 m. We chose $\overline{\Psi}^0_{-250}$ since there is little vertical depth variation in the ACC in Drake Passage in the upper 250 m; moreover, $\overline{\Psi}^0_{-250}$ is consistent with the depth range of the temperature definitions for the ACC fronts [Orsi et al., 1995; Sprintall, 2003]. Away from the area enclosed by the most repeated transects, the Maximenko et al. [2009] mean dynamic topography was used for the time-mean streamlines (Fig. 2.2). The streamlines -0.35 m $\leq \Psi^* \leq -1.65$ m were mapped at $\Delta\Psi^* = 0.10$ m. A larger contour spacing was used than that adopted for the time-mean streamlines since the spacing between synoptic streamlines is smaller compared to that of $\overline{\Psi}$ (Fig. 2.2). This reduced the resolution by half but allowed at least one data point per pair of streamlines per transect.

The synoptic streamlines show high mesoscale activity including cold and warm core rings detaching from the ACC fronts and strong meandering of the fronts (Fig. 2.2). Data points that fall inside closed contours (rings) represent a challenge as to how to assign and bin them

into a unique contour interval. Since 31 of 63 transects from November 2004 to December 2014 sampled within rings or meanders, it is desirable to devise a consistent method for the streamwise binning, rotation and averaging of each eddy heat flux component.

Three methods were tested for the rotation, binning and averaging. Method 1 looks for velocity and temperature data falling within open streamlines, whereas methods 2 and 3 find data falling inside unique intersections between each transect and open streamlines moving in the down-along-transect or up-along-transect direction, respectively. Unique intersections were defined where each transect first intersects an open streamline moving in the along-transect direction; multiple intersections for a transect (i.e. crossing a specific contour more than once) were not allowed. We then calculated individual eddy heat flux vectors and rotated them into along-stream and across-stream components as in the time-mean streamlines, except when data points fell inside closed contours (method 1) or/and cross through strong meandering (method 2 or 3). In those cases, the normal vector was re-interpolated using an inverse distance weighting method using neighboring data points. Subsequently, the eddy heat flux vector was rotated using the re-interpolated normal vector angle, and binned and averaged per pair of streamlines.

Appendix A expands the steps followed in each method. Eddy heat flux estimates determined from each method are mostly sensitive in the northern half of Drake Passage (-0.50 m $> \overline{\Psi} > -1.10$ m). In the following, only results using method 1 are shown as methods 2 and 3 show a similar spatial distribution of the eddy heat flux components. Appendix B presents the depth-integrated components calculated using methods 2 and 3.

2.5 Mean fields of geostrophic streamfunction $\overline{\Psi}$ and temperature $\overline{T}$

Maps of the objectively mapped streamfunction $\overline{\Psi}$ for two different depths (70 and 838 m) are shown in Figures 2.3a,b. The instantaneous positions of the three major ACC fronts were

determined using subsurface temperature criteria [Orsi et al., 1995; Sprintall, 2003] calculated from the temperature transects [Lenn et al., 2011]; these criteria identify the main fronts uniquely and do not distinguish potential multiple jets associated with each front [e.g. Sokolov and Rintoul, 2009]. Consequently, we determined the range of streamlines associated with each front as the streamline values that fell between the 25th and 75th percentiles of the instantaneous positions of each front; the streamlines marking the energetic Polar Front Zone (PFZ) that lies between the SAF and PF are also given (Table 2.2). The SAF shows large meandering throughout the upper 900 m. The SAF has a northeast orientation following the bathymetry whereas the PF is quasi-aligned with the down-passage direction; its streamlines show convergence at -100 km $\leq x \leq 0$ km, implying that the PF mean velocity slightly increases (Figs. 2.3a,b). The three-dimensional structure of the time-mean ACC in Drake Passage is consistent with the equivalent barotropic structure of the ACC, i.e. streamlines are self-similar with depth, as also found by Lenn et al. [2008] and Firing et al. [2011]. The region between the PF and the Southern ACC Front (SACCF) is relatively quiescent, as the spacing between contours is the largest in the Drake Passage data-fan. The maps of geostrophic streamlines are within the prescribed noise-to-signal ratio (red line in Figs. 2.3a,b). Firing et al. [2011] calculated mean maps of geostrophic velocities and streamfunction using 105 OS38 velocity transects, i.e. half of the number of transects used in our work. However, their maps have gaps south of the PF as their mapping error was larger than their prescribed noise. By increasing the number of OS38 velocities transects by two-fold over those employed by Firing et al. [2011], we resolved the mean ACC structure in Drake Passage at each depth bin in the area enclosed by the most repeated transects (Fig. 2.1) and within the noise-to-signal ratio (Figs. 2.3a,b).

The mean temperature fields $\overline{T}$ at two different depths (70 and 838 m; Figs. 2.3c,d) show maximum temperatures located near the South American continental slope: Subantarctic Surface Water in the upper layer and Subantarctic Mode Water below. The 2° isotherm is located between $-400 \leq y \leq -350$ km, corresponding to the mean position of the PF [Sprintall, 2003]. The

position of the PF delimits the area where the Antarctic Surface Water (AASW) mass subducts and flows north underneath the Subantarctic Water [Orsi et al., 1995]. South of the PF, AASW is present as a subzero surface layer extending to 150 m [Sprintall, 2003]. Below the AASW, Upper Circumpolar Deep Water is found, and it is characterized by temperatures around 1.8 °C [Orsi et al., 1995].

2.6 Eddy heat flux estimates

This section presents the mean along/across stream eddy heat flux components and mean depth-integrated eddy heat flux components and their respective standard errors using the a) time-mean $\overline{\Psi}$ and b) synoptic Ψ^* streamwise coordinate system (method 1: area between a pair of streamlines). The mean eddy heat flux estimates ($\overline{\mathbf{u}'T'}_{\overline{\Psi}}$ and $\overline{\mathbf{u}'T'}_{\Psi^*}$) and standard errors ($\hat{\sigma}_{\overline{\mathbf{u}'T'}_{\overline{\Psi}}}$ and $\hat{\sigma}_{\overline{\mathbf{u}'T'}_{\Psi^*}}$) as a function of depth and streamline are given in °C m s^{-1}. The mean eddy heat flux estimates are equivalent to the average flux per area in kW m^{-2} when multiplied by ρC_p, where $\rho = 1030$ kg m^{-3} and $C_p = 4000$ J kg^{-1} K^{-1} are the seawater density and specific heat capacity, respectively. Depth-integrated estimates ($\rho C_p \int_{-H}^{0} \overline{\mathbf{u}'T'}_{\overline{\Psi}}\, dz$ and $\rho C_p \int_{-H}^{0} \overline{\mathbf{u}'T'}_{\Psi^*}\, dz$) are given in GW m^{-1}, which represent the average heat flux per ACC unit length in the upper 886 m. A positive along-stream and across-stream flux indicates downstream and equatorward eddy heat flux, respectively. Finally, only statistically significant estimates per area are shown.

2.6.1 Time-mean streamwise coordinate system $\overline{\Psi}$

The along-stream component $\overline{u'T'}_{\overline{\Psi}}$ (Fig. 2.4a) has the largest downstream heat flux in the northern flank of the PF (-0.90 m $\geq \overline{\Psi} \geq -1.00$ m; 0.14 °C m s^{-1}) with a second peak south of the PF (-1.25 m $\geq \overline{\Psi} \geq -1.35$ m) of 0.07 °C m s^{-1}. Both peaks are maximum in the upper 200 m and then decrease below. The SAF and the PFZ ($\overline{\Psi} > -0.80$ m) in general show upstream heat flux peaking near the surface (-0.07 to -1.00 ° C m s^{-1}); south of the PF, the

along-stream component also shows upstream heat flux but only in the upper 180 m and changes below to downstream eddy heat flux. The across-stream component $\overline{v'T'}_{\overline{\Psi}}$ is poleward in the SAF and PFZ throughout the sampled water column (Fig. 2.4b). The largest poleward heat flux in Drake Passage is found on the northern flank of the PF and in the southern half of the PFZ, with a peak value of -0.17 °C m s^{-1} in the upper 150 m and decreases with depth. Additionally, poleward flux (-0.08 to -0.03 °C m s^{-1}) is found within the PF (-1.15 m $\geq \overline{\Psi} \geq -1.25$ m) from 100-350 m depth. The SAF shows significant poleward flux (-0.05 to -0.02 °C m s^{-1}) throughout the sampled water column. The standard errors of each component ($\hat{\sigma}_{\overline{u'T'}_{\overline{\Psi}}}, \hat{\sigma}_{\overline{v'T'}_{\overline{\Psi}}}$) are high ($> 0.02$ °C m s^{-1}) from the surface down to 400 m depth between the SAF and the PF and shoaling poleward (Fig. 2.4c,d). The marginal to insignificant eddy heat flux and the smaller errors south of the PF suggest that there is less eddy activity in this area compared to within the main fronts further north. The along-stream standard error $\hat{\sigma}_{\overline{u'T'}_{\overline{\Psi}}}$ is largest near the surface on the southern flank of the PF (Fig. 2.4c). On the other hand, the across-stream standard error $\hat{\sigma}_{\overline{v'T'}_{\overline{\Psi}}}$ has a surface maximum (> 0.05 °C m s^{-1}) in the south flank of the PFZ (Fig. 2.4d) that is co-located with the maximum poleward heat flux in the ACC (Fig. 2.4b).

2.6.2 Synoptic streamwise coordinate system Ψ^*

In this section, mean eddy heat flux components and their respective standard errors for the synoptic streamlines Ψ^* employing method 1 (see Appendix A) are shown. The along-stream component $\overline{u'T'}_{\Psi^*}$ is significant downstream in the PF reaching up to 0.19 °C m s^{-1} at the surface, and in the SAF ranging from 0.08 at 150 m to 0.01 °C m s^{-1} below 600 m (Fig. 2.5a). In contrast, upstream heat flux is highest (-0.15 °C m s^{-1}) south of the PF only in the upper 400 m and significant in the northern flank of the PF between 200-400 m depth. The across-stream eddy heat flux component $\overline{v'T'}_{\Psi^*}$ (Fig. 2.5b) shows a different spatial distribution compared to that calculated with $\overline{\Psi}$ (Fig. 2.4b). A prominent large area of poleward heat flux is located in the SAF and the PFZ; the maximum poleward flux (-0.05 °C m s^{-1}) is in the PFZ between 150-250 m

depth. Everywhere else the across-stream component is marginally significant to insignificant, except for the equatorward heat flux in the SACCF below 200 m. In contrast to the time-mean streamlines (Fig. 2.4c,d), the largest errors (≥ 0.02°C m s^{-1}) for both components are located between the PFZ and within the PF; the standard errors near the surface in the PFZ and PF are the largest for the along-stream eddy heat flux component (Figs. 2.5c,d). Not surprisingly, these standard error patterns are a consequence of the increase in the area defined by the synoptic streamlines associated with the PFZ (therefore, in the number of individual eddy heat flux vectors falling within it) where individual transects cross through strong meandering or rings that have detached from the ACC fronts (Fig. 2.2).

Figure 2.6 shows the depth-integrated eddy heat flux components using both the time-mean and synoptic streamlines. For the time-mean case (Fig. 2.6 dashed lines), the depth-integrated along-stream component $\overline{u'T'}_{\overline{\Psi}}$ is upstream in the SAF (-0.12 ± 0.07 GW m^{-1}) and is significantly downstream at two locations: the largest peak is found on the northern flank of the PF (0.19 ± 0.08 GW m^{-1}), and the second peak is found south of the PF (0.06 ± 0.04 GW m^{-1}). The depth-integrated across-stream component for the time-mean streamlines $\overline{v'T'}_{\overline{\Psi}}$ shows significant poleward heat flux in the region -0.85 m $\geq \overline{\Psi} \geq -1.25$ m reaching -0.20 ± 0.10 GW m^{-1} on the southern flank of the PFZ. The SAF exhibits a marginally significant poleward heat flux, but it is a factor of 2 smaller than that in the northern flank of the PFZ. South of the PF, the across-stream component is statistically insignificant. The across-stream eddy heat flux component for the time-mean case $\overline{v'T'}_{\overline{\Psi}}$ suggests heat convergence in the SAF and south of the PF, and divergence into the PFZ. In contrast, for the synoptic streamwise coordinate system (Fig. 2.6 solid lines), the depth-integrated along-stream component $\overline{u'T'}_{\Psi^*}$ displays two significant downstream heat flux peaks: the largest occurs in the SAF (0.13 ± 0.08 GW m^{-1}) and a second peak occurs in the PF (0.08 ± 0.06 GW m^{-1}). Significant upstream flux occurs south of the PF (-0.07 ± 0.03 GW m^{-1}). For the across-stream component in the synoptic coordinate system $\overline{v'T'}_{\Psi^*}$ a single poleward heat flux peak (-0.10 ± 0.05 GW m^{-1}) is located in the southern flank of the SAF and

decreases away from it, such that the poleward heat flux becomes statistically insignificant south of the northern flank of the PF. The largest difference between the two streamwise coordinate systems lies in the amplitudes of the across-stream components in the northern flank the PF; the amplitude of the maximum poleward heat flux for the time-mean streamlines is reduced by 50% when employing the synoptic streamlines. Unlike the depth-integrated $\overline{v'T'}_{\overline{\Psi}}$, the spatial distribution of the depth-integrated $\overline{v'T'}_{\Psi^*}$ shows heat convergence south of the SAF.

2.6.3 Seasonal cycle of eddy heat flux and eddy kinetic energy

We explore the seasonal cycle of the eddy heat flux components in Drake Passage by calculating climatological three-month mean depth-integrated eddy heat flux components per pair of synoptic streamlines Ψ^*. We used three-month means to allow more transects, i.e. degrees of freedom, for the austral winter months when there are fewer transects. The NB150 ADCP time series was used as it provides 108 concurrent temperature and velocity transects, i.e. 45 more transects than the OS38 ADCP time series. As described in section 3, both $\mathbf{u}'$ and T' are relative to the time-mean $\overline{\mathbf{u}}$ and $\overline{T}$. No seasonal variation was found for the objectively mapped geostrophic streamlines and velocities (not shown). Each component was rotated, binned and averaged using the synoptic streamwise coordinate system as in Method 1 (see Appendix A) to yield 108 transects of streamwise-averaged eddy heat flux. For each climatological three-month window, an average was made of all transects found within the window and assigned to the central month to produce three-month mean eddy heat flux components per pair of streamlines per depth. Finally, these fields were depth-integrated and their 15-year mean depth-integrated eddy flux subtracted to produce the three-month depth-integrated anomalies $\rho C_p \int_{-250}^{0} \overline{\mathbf{u}'T'}^{a}_{\Psi^*} dz$. We only show statistically significant depth-integrated anomalies (Fig. 2.7a,b) relative to the mean depth-integrated components (Fig. 2.7c,d). Both eddy heat flux components show a seasonal cycle. The along-stream heat flux anomalies show upstream heat flux from August-December for almost all geostrophic streamlines; downstream eddy heat flux is ubiquitous from February-

June. The anomalies are maximum upstream and downstream in the southern flank of the PFZ for August-September and March-April, respectively (Fig. 2.7a). For the across-stream component, maximum poleward flux anomalies are found during the austral late fall and early winter (May-July) reaching -0.13 GW m^{-1} in the PFZ and northern flank of the PF (Fig. 2.7b).

The mean seasonal cycle of the depth-averaged three-month EKE anomalies $\mathrm{EKE}^{a}_{\Psi^*} = \frac{1}{250}\int_{-250}^{0} 0.5\overline{(u'^2+v'^2)}^{a}_{\Psi^*}$ (using the NB150 ADCP transects paired with an XBT transect) relative to the depth-averaged mean EKE is shown in Figure 2.8. In computing the EKE, we employed only those NB150 ADCP transects paired with an XBT transect to better compare with the three-month eddy heat flux anomalies (Fig. 2.7). However, the mean EKE calculated from the paired NB150 ADCP - XBT transects ($\overline{\mathrm{EKE}}^{xbt}_{\Psi^*}$; Fig. 2.8b gray dashed line) is not statistically different compared to that calculated from the full NB150 time series ($\overline{\mathrm{EKE}}_{\Psi^*}$; Fig. 2.8b black solid line). Similar to the across-stream eddy heat flux component, the seasonal cycle of $\mathrm{EKE}^{a}_{\Psi^*}$ between the SAF and PF is the largest. However, the maximum $\mathrm{EKE}^{a}_{\Psi^*}$ is shifted by two to three months with respect to the poleward eddy heat flux three-month anomalies (Fig. 2.7b). The positive EKE anomalies are maximum (~ 0.03 m^2 s^{-2}) during austral spring-summer in the PFZ (Fig. 2.8a). Anomalies are negative during austral fall-winter in the PFZ and at the northern flank of the SAF (Fig. 2.8a). South of the PF, the maximum amplitude of the seasonal cycle of the $\mathrm{EKE}^{a}_{\Psi^*}$ is reduced by a factor of 3.

2.7 Discussion

2.7.1 Comparisons of eddy heat flux estimates between methods

The along-stream eddy heat flux component shows two significant poleward peaks at the edges of the Polar Front for the time-mean streamlines (Fig. 2.6); the largest peak is found in the northern flank of the Polar Front whereas the second peak locates in the southern flank. These two peaks stem from the fact that the time-mean streamfunction masks movement of the front

such as the bi-modal position of the Polar Front inferred by Foppert et al. [2016]. The Polar Front alternated between two preferred locations, either north or south of 58.5 °S, the latitude where their observational array crossed the Shackleton Fracture Zone, spending little time in between. The downstream peaks on each of the Polar Front flanks are merged into a broad, significant downstream heat flux peak centered inside the Polar Front when the synoptic streamlines are employed. This single peak is likely consistent with the synoptic streamlines tracking the shifting position of the Polar Front.

Similar to the along-stream eddy heat flux component, the across-stream component shows two significant poleward peaks in the flanks of the Polar Front for the time-mean streamlines (Fig. 2.6). These double poleward peaks are consistent with Foppert et al. [2016] noting that both Polar Front locations have the necessary conditions for baroclinic instability. The enhanced poleward eddy heat flux in the northern flank of the Polar Front also corresponds with the northern Polar Front proximity to the Polar Front Zone, a more energetic region influenced by bathymetry and deep eddies [Chereskin et al., 2009] than the southern Polar Front location south of the Shackleton Fracture Zone (Fig. 2.1).

For the synoptic streamwise coordinate system, the across-stream component is poleward everywhere north of the Polar Front. In contrast, the across-stream component relative to the time-mean streamlines shows equatorward heat flux in the northern flank of the Polar Front Zone, and this is most likely due to contamination of the across-stream component by the rotational along-stream component. Downstream of the Shackleton Fracture Zone, the rotational component is associated with regions of equally strong equatorward and poleward eddy heat flux in the Polar Front Zone [Watts et al., 2016] because it is recirculating locally. The poleward eddy heat flux in the Polar Front relative to the time-mean streamlines is reduced by a factor of 2.5 when the synoptic streamlines are employed. As in the Polar Front Zone, this suggests that the across-stream component relative to the time-mean streamlines still has a significant and large contribution from the dynamically irrelevant rotational component that recirculates heat locally

and does not contribute to net downgradient eddy heat flux. As a consequence, choosing the time-mean geostrophic streamlines can overestimate the divergent component and give misleading convergence/divergence of heat transport across the ACC streamlines. In contrast to the time-mean streamlines, our results using the synoptic streamlines show heat convergence south of the Subantarctic Front and are consistent with Watts et al. [2016] and Foppert et al. [2017].

The above interpretation assumes that the synoptic streamlines reflect the upper baroclinic structure of the ACC and consequently, any rotation of the total current vector with depth arises from the interaction between the barotropic (depth-independent) flow crossing the baroclinic jet [Watts et al., 2016], i.e. the baroclinic current flows parallel to the front while the total current rotates due to the barotropic flow. Veering of the total current near the bottom has been observed in Drake Passage even downstream of the Shackleton Fracture Zone where bottom topography is smoother [Firing et al., 2016]. Consequently, eddies transport heat across the ACC front (i.e. down the mean temperature gradient) and release available potential energy from the front when the barotropic component of the flow crosses with optimal phasing. This phasing in which crests and troughs are accompanied by deep highs and lows, respectively, tilted ahead of them downstream is a signature of baroclinic instability [e.g. Vallis, 2017; Watts et al., 2016].

2.7.2 Comparisons with previous Southern Ocean eddy heat flux estimates

To facilitate the comparisons among the different estimates of eddy heat flux in the Southern Ocean, the across-stream eddy heat flux components are multiplied by ρC_p to express the calculated eddy heat flux as an average heat flux per unit area (Fig. 2.9). The across-stream components per unit area in the upper 900 m, using the time-mean and synoptic streamlines in the Subantarctic Front and Polar Front Zone, agree to within a factor of 3-5 with historical estimates in Drake Passage. However, the eddy heat flux estimate relative to the time-mean streamlines in the southern flank of the Polar Front Zone is maximum and poleward (~ -600 kW m^{-2}) for the entire Drake Passage area, 2.5 times larger than the poleward heat flux obtained by Lenn

et al. [2011] and 8 times larger than that of Ferrari et al. [2014] in the upper 200 m. Moreover, the largest peak found in the southern flank of the Polar Front Zone departs from the divergent eddy heat flux spatial distribution of Watts et al. [2016], which suggests the poleward flux in the Polar Front Zone using the time-mean streamlines is overestimated due to contamination by the rotational component. Lenn et al. [2011] found the largest poleward eddy heat flux occurred in the Southern ACC Front. This disparity with our results reflects the different binning and averaging methodologies and different mean temperatures used to calculate the temperature anomalies in each study. The across-stream eddy heat flux in the Polar Front for the synoptic streamlines is insignificant, implying that the Lenn et al. [2011] estimates might still have a contribution from the rotational component in their across-stream component relative to the time-mean streamlines.

Watts et al. [2016] found significant divergent, meridional eddy heat flux estimates were maximum in the Polar Front Zone. Their poleward heat flux ranges from -130 to -70 kW m^{-2} between 100 and 300 m, and from -50 to -10 kW m^{-2} between 700 and 900 m. The spatial distribution of the depth-integrated across-stream eddy heat flux component relative to the synoptic streamlines (Fig. 2.6) shows better agreement with that of Watts et al. [2016] than the across-stream component relative to the mean streamlines. The Watts et al. [2016] estimates are from along their main transect that spans Drake Passage (blue line in the inset, Fig. 2.9), which is located within our area of study (black triangle in the inset, Fig. 2.9). Our averaged across-stream flux component per ACC unit length calculated with the synoptic streamlines shows maximum poleward heat flux in the southern flank of the Subantarctic Front (-0.10 ± 0.05 GW m^{-1}) and decreases towards the south, becoming statistically insignificant at the northern flank of the Polar Front. This distribution agrees with the circumpolarly integrated divergent eddy heat flux distribution found by Foppert et al. [2017] using a power-law fit applied to altimetry SSH standard deviation. Our across-stream estimates are integrated over the upper 900 m while Watts et al. [2016] and Foppert et al. [2017] integrated from 150 m to 3500 m. In Watts et al. [2016], half of the full-depth divergent eddy heat flux was contained in the upper 1000 m. Assuming that our

depth-integrated across-stream component represents half of the full-depth eddy heat transport, we double our value to estimate the total poleward eddy heat transport across the Subantarctic Front as -0.20 GW m^{-1}.

North of the Polar Front, the Drake Passage temperature and velocity transects are located upstream of the Watts et al. [2016]'s observations, close to but still downstream of the Shackleton Fracture Zone where Foppert et al. [2017] obtained their inferred maximum poleward depth-integrated eddy heat flux (-0.20 to -0.25 GW m^{-1}), matching our extrapolated amplitudes in the south flank of the Subantarctic Front (Fig. 2.6). Our results and Foppert et al. [2017]'s are consistent with idealized channel numerical studies demonstrating that immediately downstream of a topographic ridge, eddy buoyancy flux is maximum and down-gradient, consistent with baroclinic instability processes [e.g. Abernathey and Cessi, 2014; Barthel et al., 2017; Youngs et al., 2017]. For the synoptic streamlines, the spatial distribution of the mean EKE (Fig. 2.8b) is similar to that of $\overline{v'T'}_{\Psi^*}$, i.e. maximum in the northern flank of Polar Front Zone and decreasing away from it (Fig. 2.6). As discussed by Marshall and Shutts [1981], the divergent, downgradient eddy heat flux is locally balanced by upward vertical eddy heat flux, i.e. the release of available potential energy is balanced by conversion to EKE. Assuming that our streamlines are parallel to the temperature contours, the maximum poleward eddy heat flux in the northern flank of the Polar Front Zone collocated with the maximum EKE is consistent with the conversion of potential energy to EKE. However, the EKE in Drake Passage is more spread out within the Polar Front Zone while the divergent eddy heat flux is concentrated in a region immediately downstream of the Shackleton Fracture Zone [Foppert, 2019; Foppert et al., 2017]. This suggests that other processes such as barotropic instability potentially play a role in setting the EKE distribution in Drake Passage. Both baroclinic and barotropic instability processes are found to co-exist in regions where the ACC encounters abrupt topography [e.g. Barthel et al., 2017; Foppert, 2019; Youngs et al., 2017].

2.7.3 Seasonality

The three-month eddy heat flux anomalies are poleward during austral fall-winter, peaking in July in the Polar Front, but are mainly insignificant over the rest of the year (Fig. 2.7). These poleward anomalies roughly coincide with the maximum ocean heat loss over Drake Passage during the austral winter [Dong et al., 2007; Stephenson et al., 2012]. The northward Ekman heat transport exhibits a seasonal cycle: maximum northward Ekman heat transport during late winter and minimum in summer [Dong et al., 2007]. Therefore, our results suggest that stronger-than-average northward Ekman heat transport is partially compensated by poleward eddy heat advection in fall-winter.

An interesting result stems from the mean EKE and the seasonal cycle of EKE anomalies (Fig. 2.8). In the northern Drake Passage, the positive EKE anomalies start in September-October in the southern flank of the Subantarctic Front, shifting southward to peak in January-February in the southern flank of the Polar Front Zone. Similarly, the negative EKE anomalies in the same front move southward starting in March-April and are maximum in May-June. Consequently, the mean maximum EKE located in the southern flank of the Subantarctic Front is shifted to the southern flank of the Polar Front Zone from austral spring to summer. Rocha et al. [2016] found no seasonal variability of the kinetic energy wavenumber spectra in the upper 250 m of Drake Passage using a subset of the Drake Passage velocity transects. Because wavenumber spectra show the distribution of velocity variance versus length scale rather than location, the seasonal cycle may not be apparent in spectra computed over all of Drake Passage because the seasonal cycle is not uniformly present in space (as shown in Fig. 2.8a).

The maximum EKE anomalies in the southern Polar Front Zone (Fig. 2.8a) are out of phase with respect to the maximum poleward eddy heat flux anomalies found in the northern flank of the Polar Front (Fig. 2.7b). Elucidating the specific process driving the seasonal variability of the EKE and eddy heat flux anomalies is beyond the scope of the present work. However, three mechanisms are possible candidates. First, we suggest that internal processes such as barotropic

and baroclinic instabilities could offer an explanation of the seasonal cycle. Stronger barotropic transfer of mean kinetic energy to EKE during the austral spring-summer could explain the larger EKE amplitude when baroclinic instabilities are absent. Mixed barotropic/baroclinic processes are known to modulate the EKE on seasonal time scales in the Kuroshio Current region [Yang and San Liang, 2018]. A second process is the imprint of the surface wind stress on the surface geostrophic mesoscale currents. Renault et al. [2017] made a global analysis of the atmosphere and ocean mesoscale activity and found that in western boundary currents and in the ACC eddy hot spots, mesoscale eddy currents are damped by transferring energy to the atmosphere (i.e. negative wind work). We expect that during the austral winter this energy sink is intensified (more negative wind work than average) as the wind stress variance over the ACC is maximum during the winter. This could explain the minimum $\mathrm{EKE}^{a}_{\Psi^*}$ during the austral late-fall and winter in the Polar Front Zone and Polar Front. Finally, a third mechanism stems from a larger stratification during the austral summer. This would act to potentially increase the horizontal density gradients near the surface due to the surface heat gain from the atmosphere. Consequently, this shoals the mixed layer and provides an intensification of the eddy velocities by thermal wind balance.

2.8 Summary and conclusions

In this study, we uniquely exploited the along-track high-spatial resolution (order first baroclinic Rossby radius) of the temperature and velocity transects to estimate the eddy heat flux and EKE relative to the ACC fronts in Drake Passage. The eddy heat flux components were calculated using both the time-mean and a time-varying streamwise coordinate system calculated by adding the altimetry daily maps of sea surface height to the time-mean streamfunction.

We have summarized the main results of the across-stream eddy heat flux component calculated using both streamwise coordinate systems in Figure 2.10 . The time-mean streamwise coordinate system potentially overestimates the across-stream eddy heat flux component, and

therefore also the net heat flux across the ACC in Drake Passage. The depth-integrated across-stream heat flux component using the time-mean streamlines (blue arrows in Fig. 2.10) is maximum and poleward in the southern flank of the Polar Front Zone (-0.19 ± 0.08 GW m^{-1}); a second smaller poleward peak is found in the southern Subantarctic Front (-0.12 ± 0.07 GW m^{-1}). Conversely, the synoptic streamlines show that the maximum poleward flux is located at the southern edge of the Subantarctic Front (-0.10 ± 0.05 GW m^{-1}) and its amplitude is reduced in the Polar Front Zone becoming statistically insignificant in the Polar Front (red arrows in Fig. 2.10). We conclude that the time-varying, synoptic streamlines provided the best estimate for the dynamically important divergent eddy heat flux component as they allowed for the tracking of the ACC streamlines. The time-mean streamlines do not effectively remove the rotational component from the across-stream component. As a consequence, the time-mean streamlines overestimate the conversion from mean to available potential energy in the southern flank of the Polar Front Zone.

Despite the high spatial resolution of the transects, the mean across-stream eddy heat flux south of the Polar Front for both streamwise coordinate systems is insignificant, as also found by Sekma et al. [2013] and Watts et al. [2016] (non-filled arrows in Fig. 2.10). This result points to mechanisms other than mesoscale eddies as being responsible for the poleward heat transport in this region in order to balance the ocean heat loss to the atmosphere. Potential candidates are poleward mean heat transport due to the non-equivalent barotropic structure [Peña-Molino et al., 2014] of the ACC and/or mean poleward heat transport due to the temperature changes along the ACC streamlines [Sun and Watts, 2002]. Alternatively, the insignificant eddy heat flux across the ACC south of the Polar Front could stem from the location of the sampling fan relative to the Shackleton Fracture Zone; the transects lie over a smooth topographic plain, upstream of abrupt topography. Therefore, we would not expect enhanced poleward eddy heat flux due to baroclinic instabilities as found in the northern half of the sampling fan, i.e. downstream of the Shackleton Fracture Zone.

The unprecedented 20 years of high-spatial-resolution temperature and velocity transects in the upper 300 m spanning the entire Drake Passage presented an uncommon opportunity to explore the seasonal cycle of the EKE and eddy heat flux components. The eddy heat flux components and EKE for the time-varying streamlines undergo a spatially asymmetric seasonal variability, with a stronger seasonal cycle in the northern Drake Passage streamlines (from the Polar Front towards the north) than in the southern streamlines. The maximum mean EKE located in the northern Polar Front Zone is enhanced during the austral spring and shifts to the southern flank of the Polar Front Zone in summer. In contrast, the across-stream eddy heat flux is maximum poleward during the fall-winter season in the northern flank of the Polar Front. Mixed barotropic/baroclinic instabilities, wind damping, and stratification are among the potential processes driving the EKE and eddy heat flux seasonal variability. Eddies provide the closure to the Southern Ocean meridional overturning circulation; near the surface, eddies oppose the northward Ekman heat transport whereas deeper in the ocean, eddies are the main mechanism driving upwelling of deep waters along isopycnals. In this context, our results suggest that the eddy-driven upwelling of deep waters has a seasonal component, which is enhanced during austral fall-winter. Also, we suggest that eddy heat advection plays an important role in the Drake Passage upper-ocean heat budget by partially compensating the stronger-than-average northward Ekman heat transport in fall-winter. Our results may have implications for the carbon and nutrient cycles in Drake Passage, which have large seasonal and spatial variations [Freeman et al., 2019]. More observations and research on these topics are pivotal to fully understand the present and future changes of the Southern Ocean carbon-nutrient cycle and heat budget and to help elucidate the ACC dynamics.

2.9 Acknowledgments

We acknowledge the National Science Foundation's Office of Polar Programs Antarctic Division (ANT) and Division of Ocean Sciences (OCE) for support of the Drake Passage time series and this research through grants ANT-1542902 and OCE-1755529. MOGV acknowledges support from a UC Mexus-Conacyt fellowship. XBT temperature data were made available by the Scripps High-Resolution XBT program (http://www-hrx.ucsd.edu). The XBT probes are provided by NOAA's Global Ocean Monitoring and Observing Program through Award NA15OAR4320071. ADCP time series were acquired and processed by the Chereskin Lab at Scripps Institution of Oceanography (http://adcp.ucsd.edu/lmgould/) and can be downloaded from the Joint Archive for Shipboard ADCP (JASADCP) (http://ilikai.soest.hawaii.edu/sadcp/). The SSALTO/DUACS altimeter products were produced and distributed by the Copernicus Marine and Environment Monitoring Service (CMEMS) (http://www.marine.copernicus.eu). The Maximenko et al. [2009] mean dynamic topography for the period 1992-2012 is available at http://apdrc.soest.hawaii.edu/projects/DOT. We are also grateful to the captain and crew of the ARSV *Laurence M. Gould* and the Antarctic Support Contractor for their excellent technical and logistical support. The authors thank the two anonymous reviewers and the editor whose comments and suggestions greatly improved the manuscript.

Chapter 2, in full, is a reprint of the material as it appears in Gutierrez-Villanueva, Manuel O., Teresa K. Chereskin, and Janet Sprintall (2020). Upper-Ocean Eddy Heat Flux across the Antarctic Circumpolar Current in Drake Passage from Observations: Time-Mean and Seasonal Variability, Journal of Physical Oceanography 50, 9: 2507-2527, https://doi.org/10.1175/JPO-D-19-0266.1.The dissertation/thesis author was the primary researcher and first author.

Table 2.1: The Drake Passage datasets.

Instrument	*XBT*	*NB150 ADCP (150 kHz)*	*OS38 ADCP (38 kHz)*
Depth range (m)	0-900	24-320	42-1222
Maximum depth used (m)	890	250	900
Gridded depth resolution (m)	10	8	24
Along-track resolution (km)	6-10[a] 10-15[b]	5	5
Sampling period	Sep 1996 - Dec 2016	Sep 1999 - Dec 2014	Nov 2004 - Dec 2014
Number of cruises	130	326	204
XBT-ADCP paired transects	-	108	63

[a]Across the Subantarctic Front and Polar Front.
[b]Elsewhere in Drake Passage.

Table 2.2: Mean streamfunction $\overline{\Psi}$ intervals and latitude range for the ACC fronts. Both streamfunction and latitude values correspond to the values that fall between the 25th and 75th percentiles of the instantaneous positions of each front. Streamfunction values of each front are relative to the mean streamfunction $\overline{\Psi}$ averaged between 200-300 m depth.

	Subantarctic Front (SAF)	Polar Front Zone (PFZ)	Polar Front (PF)	Southern ACC Front (SACCF)
$\overline{\Psi}$ (m)	$-0.50 \geq \overline{\Psi} \geq -0.70$	$-0.70 > \overline{\Psi} > -1.10$	$-1.10 \geq \overline{\Psi} \geq -1.30$	$-1.55 \geq \overline{\Psi} \geq -1.65$
Latitude range	$-55.54^\circ \geq$ lat $\geq -56.15^\circ$	$-56.15^\circ >$ lat $> -58.01^\circ$	$-58.01^\circ \geq$ lat$\geq -58.90^\circ$	$-61.04^\circ \geq$ lat $\geq -62.45^\circ$

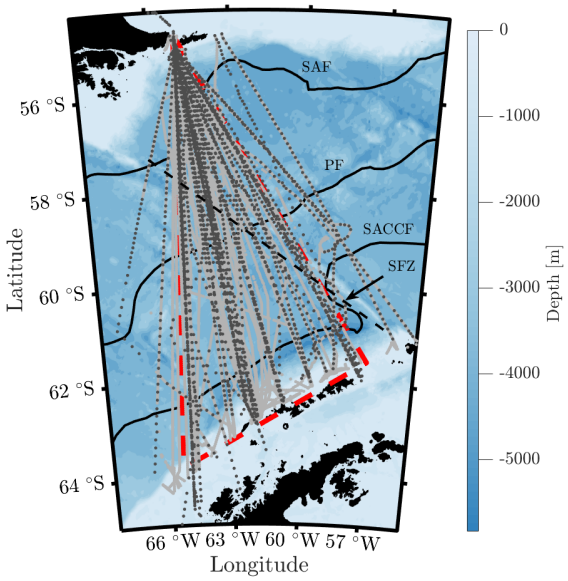

Figure 2.1: Map showing the LMG transects in Drake Passage with bathymetry from Smith and Sandwell [1997]. Dark and light gray lines show the XBT and underway ADCP velocity transects, respectively. Red dashed lines show the area enclosed by the most repeated transects. Solid black lines show the location of the major Antarctic Circumpolar Current (ACC) fronts [Orsi et al., 1995]: Subantarctic Front (SAF), Polar Front (PF) and Southern ACC Front (SACCF). The dashed black line marks the axis of the Shackleton Fracture Zone (SFZ).

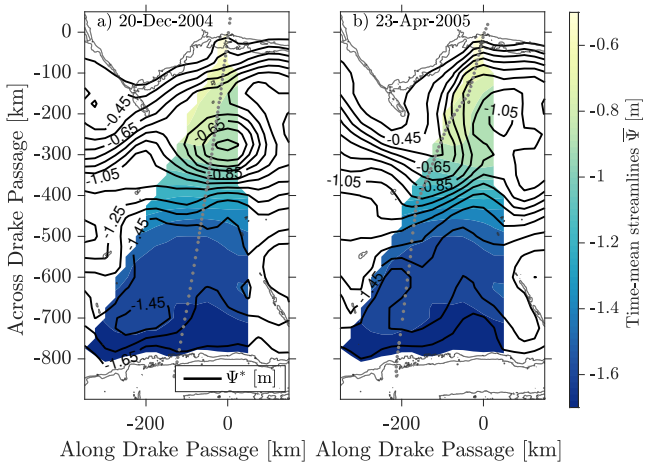

Figure 2.2: Maps of time-mean $\overline{\Psi}$ (colorbar) and time-varying Ψ^* (black solid lines) geostrophic streamfunction for (a) 19-December-2004 and (b) 23-April-2005. Streamlines are contoured at 0.10 m intervals. XBT profile positions (gray dots) and 500 m and 1000 m isobaths (thin gray lines) are indicated.

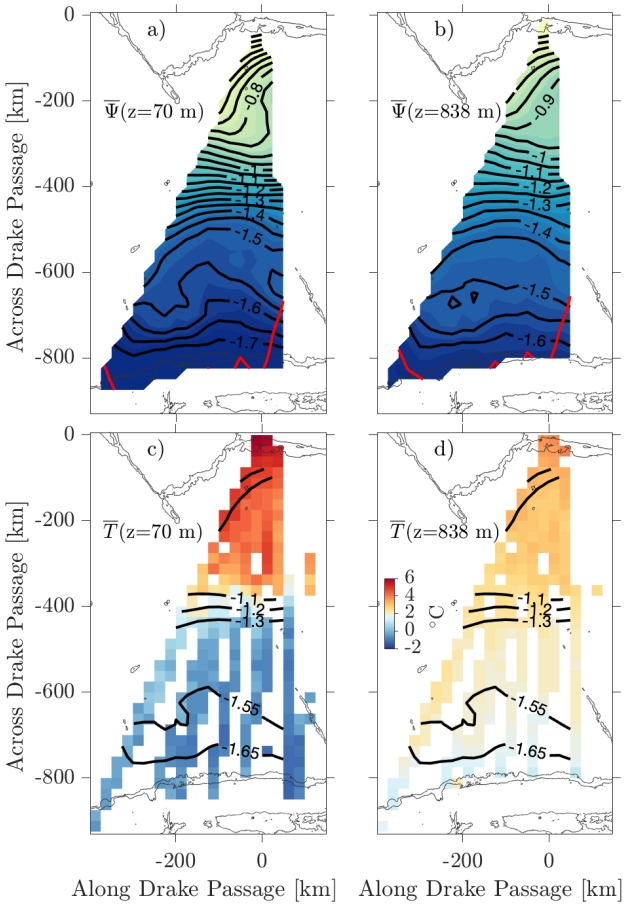

Figure 2.3: (a)-(b) Mean geostrophic streamfunction $\overline{\Psi}$ and (c)-(d) temperature $\overline{T}$ fields calculated from the LMG observations at (a),(c) 70 m; (b),(d) 838 m. Streamfunction in (a)-(b) is contoured at $\Delta\Psi = 0.05$ m within the area enclosed by the most repeated transects (Fig. 1). Red solid line shows the mapping error $E = 0.20$. The x and y axis are kilometers along and across-passage, respectively. Missing data are the blank grid boxes. The 500 m and 1000 m isobaths are contoured (light gray). Black solid contours in (c)-(d) correspond to the time-mean streamline boundaries of each ACC front averaged between 200-300 m depth (see Table 2.2).

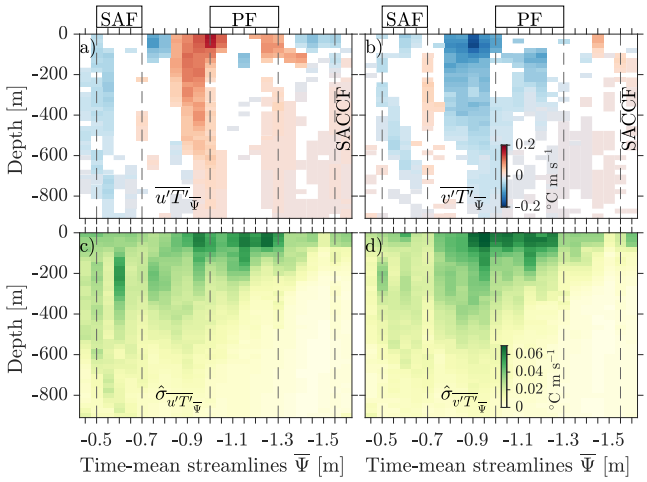

Figure 2.4: (a) Along-stream $\overline{u'T'}_{\overline{\Psi}}$ and (b) across-stream $\overline{v'T'}_{\overline{\Psi}}$ eddy heat flux components, respectively, calculated in a time-mean streamwise coordinate system $\overline{\Psi}$. Positive along-stream and across-stream values indicate downstream and equatorward heat flux, respectively. Only statistically significant eddy heat flux estimates are shown. (c) Along-stream $\hat{\sigma}_{\overline{u'T'}_{\overline{\Psi}}}$ and (d) across-stream $\hat{\sigma}_{\overline{v'T'}_{\overline{\Psi}}}$ standard errors. Eddy heat flux components and their standard errors are plotted at $\Delta\overline{\Psi} = 0.05$ m. Streamfunction values for the ACC fronts are shown in dashed lines (Table 2.2). SAF, PF and SACCF correspond to the Subantarctic Front, Polar Front and Southern ACC Front, respectively. Streamfunction decreases moving poleward.

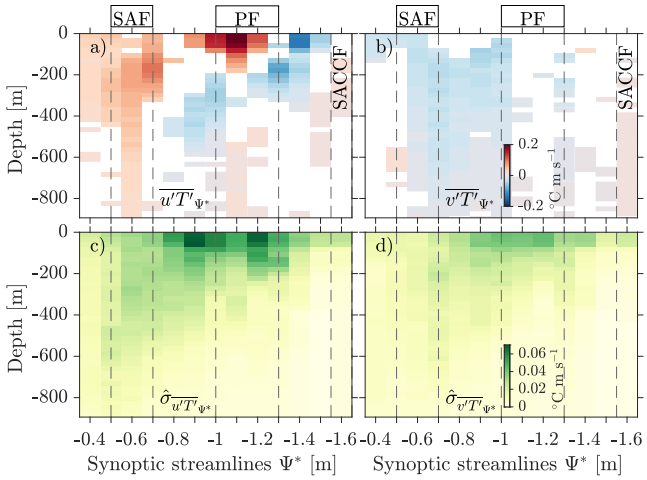

Figure 2.5: (a) Along-stream $\overline{u'T'}_{\Psi^*}$ and (b) across-stream $\overline{v'T'}_{\Psi^*}$ eddy heat flux components, respectively, calculated in a time-varying (synoptic) streamwise coordinate system Ψ^*. Positive along-stream and across-stream values indicate downstream and equatorward heat flux, respectively. Only statistically significant eddy heat flux estimates are shown. (c) Along-stream $\hat{\sigma}_{\overline{u'T'}_{\Psi^*}}$ and (d) across-stream $\hat{\sigma}_{\overline{v'T'}_{\Psi^*}}$ standard errors. Eddy heat flux components and their standard errors are plotted at $\Delta\Psi^* = 0.10$ m.

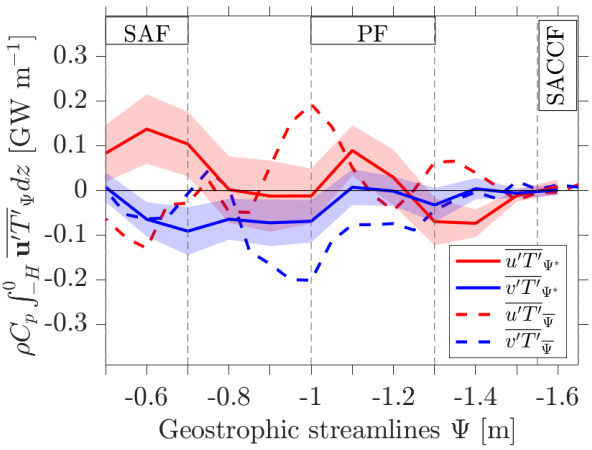

Figure 2.6: Depth-integrated along-stream $\overline{u'T'}_{\Psi^*}$ (solid red) and across-stream $\overline{v'T'}_{\Psi^*}$ (solid blue) eddy heat flux components in a synoptic streamwise coordinate system Ψ^*. Shaded areas show the standard error. Depth-integrated along-stream $\overline{u'T'}_{\overline{\Psi}}$ (dashed red) and across-stream $\overline{v'T'}_{\overline{\Psi}}$ (dashed blue) components in a time-mean streamwise coordinate system $\overline{\Psi}$. Eddy heat flux components are shown at $\Delta\overline{\Psi} = 0.05$ and $\Delta\Psi^* = 0.10$ m for the time-mean and synoptic streamlines, respectively.

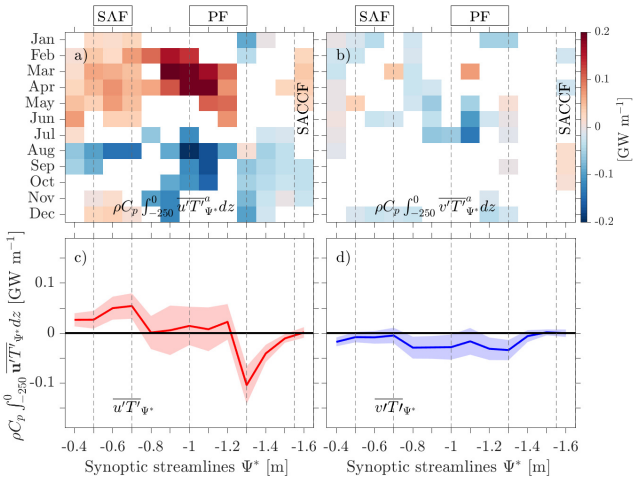

Figure 2.7: Three-month mean depth-integrated eddy heat flux anomalies for the (a) along-stream component $\overline{u'T'}^{a}_{\Psi^*}$ and (b) across-stream component $\overline{v'T'}^{a}_{\Psi^*}$. Three-month anomalies are relative to the 15-year mean of the (c) along-stream $\overline{u'T'}_{\Psi^*}$ and (d) across-stream $\overline{v'T'}_{\Psi^*}$ component. Positive along-stream and across-stream values indicate downstream and equatorward heat flux, respectively. Only statistically significant anomalies are shown. Shaded areas in (c)-(d) show the standard errors.

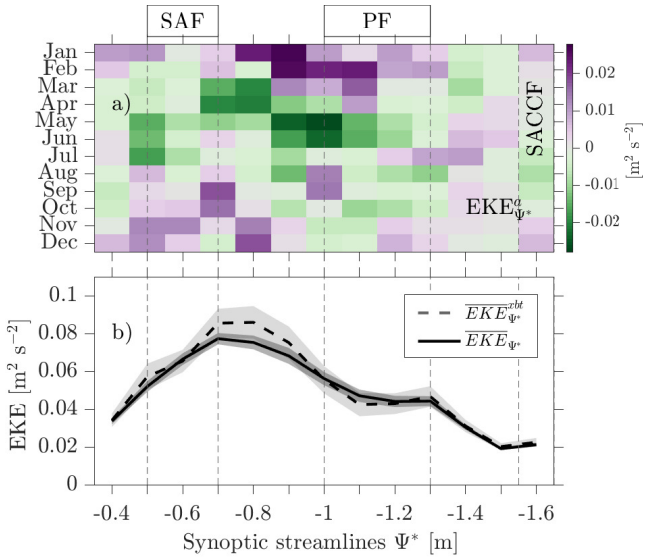

Figure 2.8: (a) Three-month mean depth-averaged eddy kinetic energy anomalies $EKE^{a}_{\Psi^*}$ calculated relative to the (b) depth-averaged mean eddy kinetic energy determined using the NB150 ADCP transects paired with the XBT transects $\overline{EKE}^{xbt}_{\Psi^*}$ (gray dashed line). The 15-year mean eddy kinetic energy calculated using all available NB150 ADCP transects $\overline{EKE}_{\Psi^*}$ (black solid line) is plotted. Shaded areas show the standard error of each mean depth-averaged eddy kinetic energy.

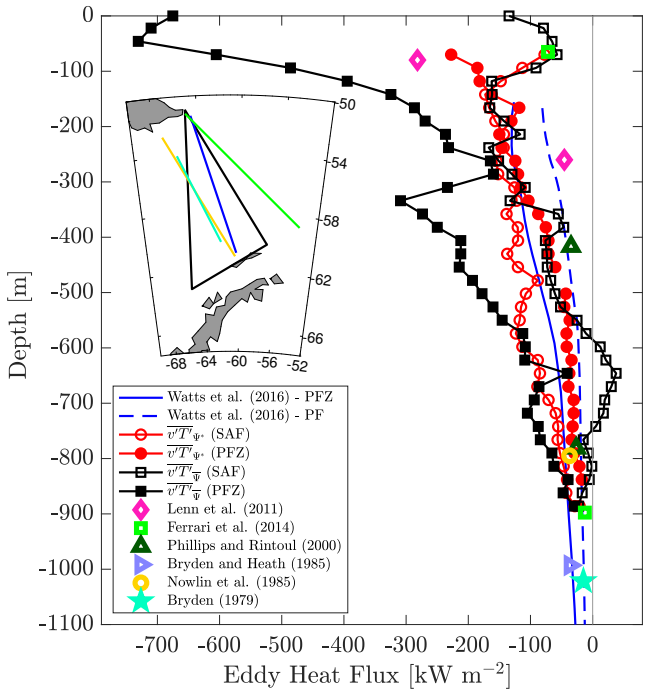

Figure 2.9: Historical eddy heat flux estimates from observations in the ACC (symbols). Black squared profiles show this study's across-stream eddy heat flux estimates calculated using the time-mean streamfunction $\overline{v'T'}_{\overline{\Psi}}$ in the Subantartic Front (open) and Polar Front Zone (filled). Red circled profiles correspond to this study's across-stream heat flux estimates calculated using the synoptic streamlines $\overline{v'T'}_{\Psi^*}$ in the Subantartic Front (open) and Polar Front Zone (filled). Our estimates were multiplied by ρC_p. Blue solid and dashed profiles show the Watts et al. [2016] divergent meridional eddy heat flux in the Polar Front Zone and Polar Front, respectively. The small inset shows the color-coded locations of historical eddy heat flux estimates in Drake Passage, as referenced in the legend. The black triangle in the inset shows the area enclosed by the most repeated transects in this study. Adapted from Watts et al. [2016].

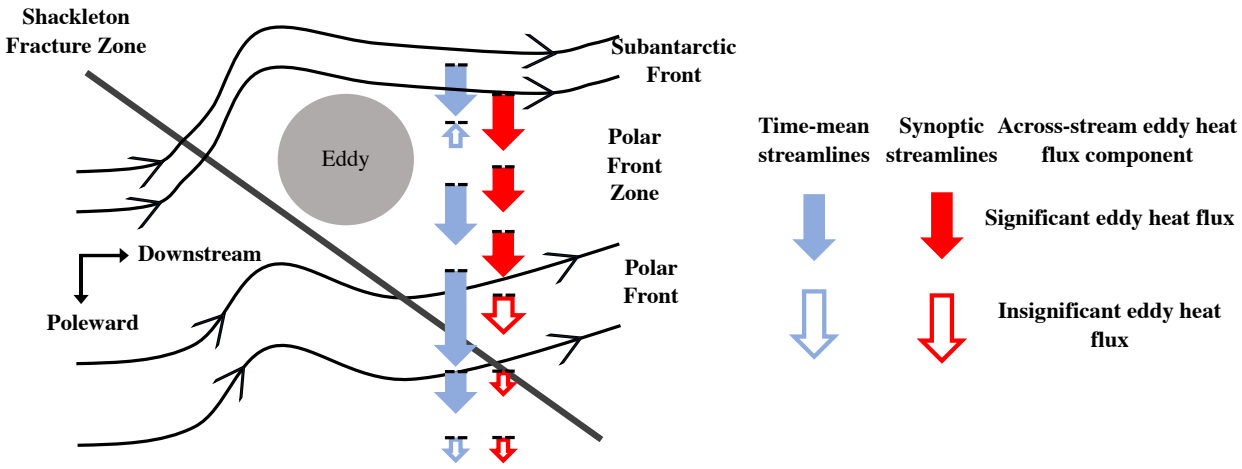

Figure 2.10: Plan view schematic of the eddy heat flux across the ACC fronts in Drake Passage depth-integrated over the upper 900 m (see Fig. 2.6). Blue and red arrows represent the depth-integrated across-stream eddy heat flux component using the time-mean streamlines $\overline{\Psi}$ and synoptic streamlines Ψ^*, respectively. Filled arrows indicate significant eddy heat flux whereas non-filled arrows show insignificant eddy heat flux. Longer arrows indicate a larger across-stream eddy heat flux. Black solid contours show the streamlines of the indicated ACC fronts. Dashed horizontal lines show the location from which the arrow originates from. The diagonal line indicates the axis orientation of the Shackleton Fracture Zone. Gray-filled circle indicates where significant eddy activity is found.

Chapter 3

Turbulent mixing and lee-wave energy radiation: sensitivity to topography

3.1 Abstract

Radiation and breaking of internal lee waves are thought to play a significant role in the energy and heat budget of the Southern Ocean. Open questions remain, however, regarding the amount of energy converted from the deep flows of the Antarctic Circumpolar Current (ACC) into lee waves and how much of this energy dissipates locally. This study estimated the linear lee-wave energy radiation using a unique four-year time series of stratification and near-bottom currents from an array of Current and Pressure measuring Inverted Echo Sounders (CPIES) spanning Drake Passage. Lee-wave energy was calculated from two 2D anisotropic and one 1D isotropic abyssal hill topographies. Lee-wave energy radiation from all three topographies was largest in the Polar Front Zone, associated with strong deep meandering of the ACC fronts. Both baroclinic and barotropic instabilities appeared to modulate the conversion to lee waves in the Polar Front Zone. Finestructure temperature, salinity and velocity profiles at the CPIES locations were used to estimate turbulent dissipation due to breaking internal waves by employing a finescale

parameterization. High dissipation near the bottom was consistent with upward-propagating, high-frequency lee waves as found by earlier studies. In contrast to idealized numerical predictions of 50% local dissipation of lee wave energy, this study found less than 10% dissipated locally, similar to some other studies. Improving the representation of the abyssal hills by accounting for anisotropy did not reduce the discrepancy between radiated lee-wave energy and local dissipation. Instead, alternative fates must be considered for the excess radiated lee-wave energy.

3.2 Introduction

Small-scale turbulent mixing plays a dominant role in the Southern Ocean overturning circulation and Antarctic Circumpolar Current (ACC) dynamics, impacting the distribution of heat, carbon, nutrients, and other tracers in the global ocean. Dense waters formed in the Antarctic continental margins sink and flow over the continental shelf breaks, moving through the Southern Ocean's abyssal basins. These dense waters are returned to the deep and intermediate layers ($1500 - 3000$ m depth) through turbulent mixing across density layers. From an energetics point of view, turbulent mixing is a pathway to dissipation for the energy input from tides, wind, and geostrophic flows. Sparse observations of turbulent mixing in the Southern Ocean, however, preclude a complete understanding of the physical processes modulating the spatial and temporal variability of turbulent mixing. Such understanding is required to develop realistic parameterizations of mixing for numerical models. As a result, ocean climate models have inaccurate representations of the mixing field, potentially leading to an imprecise picture of the Southern Ocean's meridional overturning circulation in models.

Turbulent mixing is enhanced at locations in the Southern Ocean where the ACC encounters rough topography [e.g. Garabato et al., 2004; Ledwell et al., 2011; Meyer et al., 2015; Sheen et al., 2013; St. Laurent et al., 2012; Thompson et al., 2007; Waterman et al., 2014]. The interaction of the ACC geostrophic flow with rough topography favors the generation of

internal lee waves [Cusack et al., 2017]. Lee waves (waves locked in phase) can transport and redistribute energy and momentum from the flow. Lee waves may exert a non-negligible drag on the ACC's momentum balance [Naveira Garabato et al., 2013] and play a fundamental role in the abyssal water mass transformation through wave breaking, and therefore diapycnal mixing [Nikurashin and Ferrari, 2013]. Furthermore, recent studies demonstrate that internal lee waves are an essential mechanism by which mesoscale eddies lose energy; the estimated energy loss to linear waves in the Southern Ocean is significantly larger for the eddy field (0.12 TW) compared to the time-mean flow [0.04 TW; Yang et al., 2018].

Significant uncertainties remain regarding the amount of lee-wave energy that is dissipated locally over rough topography. More lee-wave energy radiation than local dissipation is often predicted by linear theory when using in situ observations and near-bottom turbulent dissipation rates within the ACC fronts [Sheen et al., 2013; Waterman et al., 2014]. Also, the near-bottom dissipation rates estimated by finescale parameterizations based on weakly nonlinear wave-wave interactions are often over-predicted compared to the direct estimates of turbulent dissipation rates from Vertical Microstructure Profilers [VMPs; Sheen et al., 2013; Takahashi and Hibiya, 2019; Waterman et al., 2014]. Waterman et al. [2014] suggested several mechanisms not encapsulated in the finescale parameterizations that could potentially explain the over-prediction of the dissipation rate: wave advection by the geostrophic flow [Zheng and Nikurashin, 2019], waves encountering critical layers, and re-absorption of the lee-wave energy into the geostrophic flow [Kunze and Lien, 2019]. This bias suggests that the discrepancy between the expected lee-wave energy radiation and local dissipation estimated by finescale parameterizations could be higher than that from direct estimates of dissipation.

Several authors [Sheen et al., 2013; Trossman et al., 2015; Waterman et al., 2014] integrated their turbulent dissipation estimates over the 1000 m closest to the bottom, since Nikurashin and Ferrari [2010b] showed with their numerical simulations that internal-wave energy dissipation is enhanced in the bottom kilometer. However, Baker and Mashayek [2021] recently showed

with a linear model that bottom-generated upward-propagating lee waves can reflect downwards from a reflective upper boundary in the absence of critical layers. Their numerical simulations showed that the inclusion of the upper boundary enhances near surface vertical velocities and the turbulent dissipation due to breaking waves. Moreover, in more realistic simulations using typical stratification and current profiles for Drake Passage, the lee-wave energy and dissipation increase due to a more vigorous energy transfer from the sheared currents to the wave field. Hence, the Baker and Mashayek [2021] results suggest the treatment of the lee-wave radiation and dissipation problem as a full water-column process.

A critical aspect of estimating the energy conversion from geostrophic flows to lee waves is the characterization of the abyssal sea topography. Many authors [Nikurashin and Ferrari, 2013; Sheen et al., 2013; Waterman et al., 2013] use the Bell Jr [1975] linear theory and assume a one-dimensional, isotropic representation of abyssal hill topography using the spectral model of Goff and Jordan [1988]. Although Nikurashin and Ferrari [2011] state that the assumption of isotropy has no effect on their global estimates of energy radiation into lee waves, more recent estimates [Trossman et al., 2015; Yang et al., 2018] indicate that results may be sensitive to anisotropy. In fact, these latter studies also suggest that the excess of predicted local energy conversion into lee waves relative to observed near-bottom energy dissipation rates, as found in Sheen et al. [2013] and Waterman et al. [2014], could be attributed to the assumption of isotropy. Further comparisons between lee-wave radiation estimated using linear theory and high-resolution anisotropic bathymetry with near-bottom turbulent dissipation rates are needed to test this sensitivity.

Measurements resolving turbulence have been challenging to achieve in the Southern Ocean since they rely on specialized ship-deployed instruments. Direct estimates of turbulent dissipation are scarce and limited in space and time, making it difficult to obtain stable mean mixing estimates. During the Diapycnal and Isopycnal Mixing Experiment in the Southern Ocean (DIMES) experiment (2010-2011), sections upstream and downstream of Drake Passage were

surveyed using various platforms (e.g. VMPs, dyes, finestructure casts). However, these sections were single one-time semi-synoptic surveys. In this paper we will estimate dissipation rates of turbulent kinetic energy dissipation ε using a shear-strain finescale parameterization [Polzin et al., 2014] by exploiting a series of annually-repeated full-depth conductivity-temperature-depth (CTD) and Lowered Acoustic Doppler Current Profiler (LADCP) casts taken in Drake Passage in late austral spring from 2007 to 2011 (Fig. 3.1). Drake Passage is an identified hot spot of internal wave generation and turbulent mixing due to breaking internal waves [Sheen et al., 2013]. We will assess the relationship of finescale turbulent mixing and internal wave properties (frequency and energy propagation) under different regimes, including the background stratification, current speed, the position of the ACC fronts, and topography. Our study will also employ a unique 4-year time series of bottom-moored Current and Pressure recording Inverted Echo Sounders (CPIES) that span Drake Passage (Fig. 3.1) to produce a time series of lee-wave energy radiation. A spatially-denser subset of the CPIES array located downstream of the Shackleton Fracture Zone (Fig. 3.1) is used to determine the relationship between the mesoscale field (via the geostrophic streamfunction and its derivatives), the turbulent mixing due to breaking internal waves, and the radiation of lee waves.

We expect that lee waves are generated in Drake Passage by the interaction of the near-bottom ACC flow with the abyssal topography. A few studies have used single full-depth in situ CTD/LADCP casts to estimate the energy radiation into lee waves and compared it to their depth-integrated (to 1000 m above the bottom) dissipation rates [Sheen et al., 2013, 2014; Waterman et al., 2013, 2014] assuming an isotropic form of the abyssal hill topographic spectrum from Goff and Jordan [1988]. As noted above, the lack of anisotropy information in the small-scale topography could significantly impact the energy estimates. In this study, our estimates of lee-wave energy radiation employ the abyssal hill statistical parameters from Goff [2020] determined from global gravimetric measurements, including the anisotropy information in the topographic spectra. Moreover, we employ high-resolution multibeam (MB) bathymetric data for the Drake

Passage region to estimate the abyssal hill statistical parameters. The MB data allow us to capture the small-scale abyssal hills (1-10 km), i.e., the length scales predicted by linear lee-wave theory that are not captured by coarser resolution gravimetric data. The different topographic datasets and their statistical parameters allow us to assess the sensitivity of energy radiation estimates to the choice of statistical parameters that represent the 2D topographic spectra. In addition, we will calculate the energy loss to lee waves using the 1D isotropic topography of Nikurashin and Ferrari [2011], and compare to that calculated using the Goff [2020] and MB anisotropic topographies.

This paper is structured as follows. Section 2 presents the data sets. An overview of the methodology to estimate dissipation rates, internal wave parameters and lee-wave energy radiation is presented in section 3. Section 4 presents the dissipation rates and wave parameters estimated across Drake Passage and their relationship with background stratification, shear, and the ACC frontal positions. Lee-wave energy radiation estimates are presented and compared with previous studies in section 5. The spatial variability across Drake Passage of the lee-wave energy radiation and its time variability are also explored in this section. The effect of including the anisotropy in the topographic spectrum of the energy estimates is presented in section 6. Section 7 compares the local turbulent dissipation rates and the local lee-wave energy radiation using different topographic datasets. We finalize with the summary and conclusions in section 8.

3.3 Data sets

3.3.1 cDrake finestructure profiles

As part of the cDrake project [Chereskin et al., 2012], full-depth CTD/LADCP casts were taken at 43 sites in Drake Passage during five annual cruises aboard the RVIB Nathaniel B. Palmer in late austral spring (November) of 2007 through 2011 (Fig. 3.1). Casts were performed to within 20 m of the bottom when possible. A total of 177 casts were collected over the 4 years at the CPIES sites.

For the CTD casts, a SeaBird SBE 11-Plus was deployed; the instrument has an initial accuracy of 0.001°C and 0.003 psu for temperature and salinity respectively resulting in density estimates accurate to 0.003 kg m^{-3}. Bottle samples were taken during each cast at scheduled depths to validate salinity, and CTD calibrations were performed pre- and post-cruise for each year. The CTD downcast data used here were quality-controlled, despiked, and averaged to 1-dbar vertical resolution. Before implementing the finescale parameterization, we followed Whalen et al. [2012] and removed the upper-ocean mixed layer and the poorly-stratified layer below the mixed layer (e.g. mode-water layers and pycnostads) from the CTD profiles using the density-based criteria of de Boyer Montégut et al. [2004]. These weakly stratified regions exhibit high strain not due to internal waves, leading to spuriously high dissipation rates.

The LADCP current velocity profile at the location of the CTDs was obtained using a single downward-looking 150 kHz RDI Phase 3 broadband ADCP with 30° beam angles mounted on the CTD rosette. The LADCP sampled with a 16-m vertical bin and a staggered ping cycle alternating 1 s and 1.6 s between pings. The staggered ping cycle results in a region of reduced sampling between 500-1000 m above the bottom, but it avoids a complete data void arising from when the previous ping reflects off the bottom and so interferes with the current ping. Data were collected in beam coordinates. During each cast, two hull-mounted RD Instruments shipboard ADCPs recorded velocity data: a 150 kHz narrowband ADCP (NB150) on all five cDrake cruises (2007-2011) and an Ocean Surveyor 38 kHz phased array (OS38) on the last three cruises (2009-2011). The NB150 maximum profiling range is 300 m with 8-m vertical resolution; the OS38 maximum profiling range is 1000 m with a 24-m vertical resolution [more details about the data acquisition and processing is available in Firing et al., 2016; Gutierrez-Villanueva et al., 2020]. Horizontal velocities (u, v) and vertical shears were obtained from the simultaneous CTD/LADCP profiles using the velocity inversion method of Visbeck [2002]. In brief, for each LADCP cast, the method defines a system of linear equations constrained with bottom tracking, along with the ship-drift data and the hull-mounted shipboard ADCP profiles. The system of equations is solved

using a standard least-squares technique to yield absolute velocity profiles with a 15-m vertical resolution. Absolute velocity errors are relatively small (≤ 0.05 m s^{-1} on average). Data were excluded in depth bins where the error was equal to or larger than the absolute velocity. Finally, the barotropic tide predicted from the TPXO7.2 model [Egbert et al., 1994] was averaged over the LADCP cast duration and subtracted from the velocity profile for the lee-wave energy radiation calculation (section 3.4).

3.3.2 cDrake CPIES and mapped geostrophic fields

An array of bottom-moored CPIES spanning Drake Passage was deployed from November 2007 to December 2011 (Fig. 3.1). The cDrake array consisted of a line of 20 CPIES spanning 800 km across Drake Passage (C-Line) and a local dynamics array of 3×7 (21 total) CPIES spanning 120 km cross-stream and 240 km downstream [Chereskin et al., 2012] (Fig. 3.1). An additional five CPIES (referred to as the H array) were placed along the Shackleton Fracture Zone during the observational program's final year in 2011. The CPIES were moored in water depths ranging from 500 m on the northern edge of the passage to 4300 m in the middle. The shallowest 2 sites (C01 and C17), on the continental slope, are not used in this study. Each CPIES unit recorded bottom-to-surface round-trip acoustic travel time, pressure and temperature at 0.5 m above the bottom, and velocity from an Aanderaa current meter tethered 50 m above the bottom. All instruments were sampled at hourly or shorter time intervals. To remove the barotropic tide and extract the slowly-variant geostrophic flow, the near-bottom currents were three-day low-pass filtered using a fourth-order Butterworth filter and subsampled to 12-h intervals [Tracey et al., 2013].

Tracey et al. [2013] describe in detail the processing of the pressure and acoustic travel time measurements. Here we summarize the travel time corrections and how they are used to determine temperature, salinity, buoyancy b and stratification N^2 full-depth time series. First, acoustic travel time was adjusted for the inverse barometer effect, the latitudinal effect of gravity,

and the seasonal cycle. The acoustic travel time is then converted to travel time τ_{index} between the surface and 2000 dbar using a second order polynomial, with depth-dependent coefficients determined from the historical hydrography (526 CTD and Argo float data) within Drake Passage. A constant offset for each CPIES site was determine from calibration CTDs made at the site [Chidichimo et al., 2014; Firing et al., 2014]. The hourly time series of τ_{index} were filtered using a three-day low-pass Butterworth filter; 24 hr at the beginning and the end of the records are removed to avoid transients. Subsequently, the filtered time series were subsampled to twice daily intervals.

The gravest empirical mode (GEM) analysis relates τ_{index} to temperature, salinity, and calculated quantities such as b and N^2 by using the available hydrography mentioned above [Tracey et al., 2013]. The GEM for each quantity was computed by fitting smoothing splines to the relationship between τ_{index} and temperature, salinity, b and N^2 at a range of different pressure levels p from 4000 dbar to the surface. The buoyancy GEM [Foppert et al., 2016] was constructed by first calculating neutral density following Jackett and McDougall [1997] with the temperature and salinity GEMs. Buoyancy was then estimated as $b = -g\frac{\gamma-\gamma_0}{\rho_0}$, where $g = 9.81$ m s^2 is gravity, $\rho_0 = 1035$ kg m^{-3} is the seawater density, and $\gamma_0 = 28.5$ kg m^{-3} is a deep neutral density. Subsequently, the N^2 GEM was calculated as $\frac{\partial b}{\partial z}$. The GEM for each variable was then vertically interpolated to 10-dbar intervals using cubic splines. Consequently, low-pass four-year, twice-daily time series of $b(p,t)$ and $N^2(p,t)$ were obtained at each CPIES site by using $\tau_{index}(t)$ to look up $b(p,\tau)$ and $N^2(p,\tau)$ in their GEM by linear interpolation.

For the local dynamics array, near-bottom pressures and currents referenced to 4000 dbar were objectively mapped satisfying the geostrophic relationship $\nabla \cdot f\mathbf{U} = 0$ (where ∇, f and $\mathbf{U}$ are the horizontal gradient operator, Coriolis frequency and horizontal velocity vector, respectively) to obtain geostrophic streamfunction and horizontal velocity [Firing et al., 2014]. These 4000-dbar absolute geostrophic fields are referred to as the depth-independent, barotropic component. Geopotential anomaly at each depth was objectively mapped to obtain the depth-

dependent, baroclinic geostrophic streamfunction and velocity and their gradients. This study uses the mapped geostrophic velocity where the mapping error is < 0.08 m s^{-1}. Further information on the objective mapping methodology and validation of the mapped fields with numerical simulations and independent data sets is provided in Firing et al. [2014].

3.3.3 Multibeam bathymetry

MB bathymetry data were obtained for the Drake Passage area from the Global Multi-Resolution Topography (GMRT) Synthesis [Ryan et al., 2009]. This synthesis is maintained as a multi-resolution gridded global Digital Elevation Model (DEM) that includes quality-processed ship-based MB sonar data at their full spatial resolution. The gridded bathymetry for the Drake Passage area includes the sonar data collected since 1992, which includes the five cDrake cruises around the CPIES and the CTD/LADCP casts [Fig. 3.1; Firing et al., 2016].

3.3.4 Mean Dynamic Topography

The ACC frontal locations are determined using the Mean Dynamic Topography from Maximenko et al. [2009] derived from a combination of 20 years of satellite altimetry, gravity measurements, and in situ data. We use each front's streamfunction values as defined by Gutierrez-Villanueva et al. [2020] to determine the CPIES and finestructure profile positions relative to the fronts in Drake Passage. There are 3, 26, 5 and 5 CPIES locations within the Subantarctic Front, Polar Front Zone, Polar Front and Southern Drake Passage regions, respectively (Fig. 3.1).

3.4 Methods

3.4.1 Finescale parameterizations

We infer finescale turbulent dissipation rates, ε, due to breaking internal waves by applying a finescale parameterization to the CTD/LADCP casts. The two key assumptions of the parameterization are 1) that both shear V_z and strain ξ_z at scales $O(10-100)$ m are caused mainly by internal waves and 2) that nonlinear wave-wave interactions stimulate a downscale energy cascade resulting in internal wave breaking, leading to turbulent dissipation [Polzin et al., 2014, and references therein]. Several studies have applied this parameterization to CTDs, LADCPs, and profiling float profiles in the Southern Ocean, revealing an energetic internal wave field in the ACC [e.g. Frants et al., 2013; Garabato et al., 2004; Kunze, 2017; Kunze et al., 2006; Meyer et al., 2015; Sheen et al., 2013; Thompson et al., 2007; Waterhouse et al., 2014; Waterman et al., 2013; Wu et al., 2011]. Here we apply the finescale parameterization [Polzin et al., 2014]:

$$\varepsilon = \varepsilon_0 \frac{< V_z^2/\overline{N}^2 >^2}{< V_z^2{}_{GM}/N_0^2 >^2} h(R_\omega) L(f,\overline{N}), \tag{3.1}$$

$$h(R_\omega) = \frac{3(R_\omega+1)}{2\sqrt{2}R_\omega\sqrt{R_\omega-1}}, \tag{3.2}$$

$$L(f,\overline{N}) = \frac{f\cosh^{-1}[\overline{N}/f]}{f_{30}\cosh^{-1}[N_0/f_{30}]}, \tag{3.3}$$

where $\varepsilon_0 = 6.37\times10^{-10}$ W kg^{-1}, $N_0 = 5.2\times10^{-3}$ rad s^{-1}, $V_z^2{}_{GM}/N_0^2$ are the canonical Garrett-Munk dissipation rate [Polzin et al., 2014], stratification, and buoyancy-normalized shear variance, respectively; $f_{30} = 7.3\times10^{-5}$ rad s^{-1} is the inertial frequency at 30° latitude, f is the local Coriolis frequency in rad s^{-1}, and $\overline{N}$ is the mean stratification $\overline{N}$ estimated by doing quadratic

fits for each 320-m window of the buoyancy frequency (stratification) profile computed from individual CTD profiles N. In the absence of observations of the simultaneous frequency and wavenumber energy content, the only source of information for the frequency content of the internal wave field is the shear-to-strain ratio R_ω

$$R_\omega = \frac{< V_z^2/\overline{N}^2 >}{< \xi_z^2 >}. \tag{3.4}$$

For a single wave frequency ω, $R_\omega \cong (\omega^2 + f^2)/(\omega^2 - f^2)$, is a proxy for the ratio of horizontal kinetic energy to potential energy. For a Garrett-Munk internal-wave field, $R_\omega = 3$; larger values than Garrett-Munk indicate more near-inertial frequency content.

3.4.2 Estimating finescale dissipation rates of turbulent kinetic energy ε

Shear and density profiles were broken into 320-m windows with a 50% overlap from the surface to the bottom. For each 320-m segment of buoyancy-normalized shear variance $V_z^2/\overline{N}^2$, a linear fit was removed and a Hanning window was applied before Fourier transformation. Shear spectra were corrected due to smoothing associated with finite differencing, interpolation, and instrument tilting by using the Polzin et al. [2002] LADCP noise model. Next, shear variance was calculated by integrating the buoyancy-normalized shear spectra over specific limits of integration $V_z^2/\overline{N}^2 = \int_{m_{min}}^{m_{max}} S_i[V_z/\overline{N}]dm$, where m_{min}, m_{max} are the minimum and maximum (cutoff) vertical wavenumbers, respectively; $S_i[]$ indicates the vertical wavenumber spectra. The cutoff m_{max} wavenumber corresponds to the wavenumber limit at which $S_i[V_z/\overline{N}]$ rolls off, indicating the transition from weakly nonlinear to strongly nonlinear wave-wave interactions [Gargett, 1990]. We found that $\sim 90\%$ of individual $S_i[V_z/\overline{N}]$ had a roll-off in the buoyancy-normalized spectra that started at $2\pi/106$ rad m^{-1} (not shown). Consequently, we decided to integrate $S_i[V_z/\overline{N}]$ using $2\pi/320$ rad m^{-1} and $2\pi/106$ rad m^{-1} as the m_{min} and m_{max}, respectively. The Garrett-Munk shear

variance [Cairns and Williams, 1976] was also integrated using the same limits of integration to obtain GM buoyancy-normalized shear variance.

Internal-wave strain ξ_z is computed from the stratification profiles as $\xi_z = (N^2 - \overline{N}^2)/\overline{N}^2$ for each 320-m window. Strain variances were obtained by integrating the spectra over the specific wavenumber limits $\xi_z^2 = \int_{m_{min}}^{m_{max}} S_i[\xi_z]dm$; the same limits of integration used for $V_z^2/\overline{N}^2$ are also employed for ξ_z^2. Using fixed limits for both shear and strain avoids the need to normalize by their respective Garrett-Munk spectra.

We tested the sensitivity of the finescale dissipation estimates ε and shear-strain ratio R_ω to different finescale parameterizations and limits of integration (Fig. 7.1, 7.2). First, we employed alternative limits of integration as in Sheen et al. [2013] ($2\pi/160$ rad m^{-1} and $2\pi/64$ rad m^{-1}; see Fig. 7.1a,d and 7.2a,d). Using different limits did not significantly affect the amplitudes of either ε or R_ω; the spread of the cloud for ε is within one order of magnitude difference for 320-m estimates located near the surface (height above bottom $>$ 1500 m). The medians (filled squares and gray error bars in Fig. 7.1a,d and 7.2a,d) show that half of the estimates align with the 1:1 relationship. The R_ω comparisons show that using larger wavenumber limits of integration brings the ratio down by a factor of three in general (filled squares in Fig. 7.1d and 7.2d), meaning that relatively short waves have less near-inertial energy content. On the other hand, comparing ε calculated with the strain-only parameterization with that estimated using the shear and strain estimates (for each 320-m window) shows the ε estimates do not vary significantly (Fig. 7.1b and 7.2b); a large number of points fall along the 1:1 line, although some strain-only estimates are larger than the shear-strain estimates. Using larger wavenumber limits of integration for the strain-only parameterization gives dissipation estimates comparable to that of the shear-strain case (Fig. 7.1c and 7.2c). Consequently, in the following we use the shear-strain parameterization and chose $2\pi/320$ rad m^{-1} and $2\pi/106$ rad m^{-1} as the m_{min} and m_{max}, respectively.

To avoid singularities when calculating ε (see eqs. 3.1, 3.2), R_ω was set to 1.01 if the calculated $R_\omega < 1.01$. Alternatively, Kunze et al. [2006] inferred that global shear estimates

are dominated by noise rather than internal-wave energy in regions of weak stratification, as indicated by a sharp increase in R_ω where stratification decreases. We explored this shear noise contamination in our data sets by binning R_ω as a function of $\overline{N}$ for each individual cDrake cruise as well as combining all cruises (not shown). We concluded that shear measurements (and therefore ε and R_ω) appear to be unbiased due to low stratification. We also inspected the data for the possibility of shear contamination due to low ADCP range in regions of weak acoustic backscatter, but found no increase in R_ω as the ADCP range decreased.

3.4.3 Internal wave properties

The polarization ratio ϕ quantifies the dominant energy propagation of single frequency internal waves. It is an approximation of the ratio of upward to downward energy propagation; however, it may not indicate the energy flux vertical propagation in a multichromatic wave field [Waterman et al., 2014]. The ratio $\phi_{ccw/cw}$ is calculated as

$$\begin{aligned} \phi_{ccw/cw} &= \frac{\phi_{ccw}}{\phi_{cw}}, \\ \phi_{ccw} &= \frac{S_i[V_z(u/N)]+S_i[V_z(v/N)]+2QS}{2}, \\ \phi_{cw} &= \frac{S_i[V_z(u/N)]+S_i[V_z(v/N)]-2QS}{2}, \end{aligned} \tag{3.5}$$

where $\phi_{ccw}, \phi_{cw}, QS$ are the counterclockwise (ccw) and clockwise (cw) shear variance and the quadrature spectra, respectively; u, v are the zonal and meridional velocity components. In the Southern Hemisphere, a dominance of counterclockwise polarization ($\phi_{ccw}/\phi_{cw} > 1$) indicates a dominance of downward directed internal wave energy propagation. Conversely, a dominance of clockwise polarization ($\phi_{ccw}/\phi_{cw} < 1$) indicates a dominance of upward internal wave energy flux. We calculated ϕ by integrating the ccw, cw and quadrature spectra, estimated from the 320-m

buoyancy normalized shear variance windows, over the wavenumber limits used to calculate ε and R_ω.

3.4.4 Estimating lee-wave energy radiation

Lee-wave theory

Assuming a stable density stratification N^2, and both quasi-steady (slowly variant) $\mathbf{U}$ and tidal currents $\mathbf{U}_t$ flowing over subcritical topography, the Bell Jr [1975] linear theory gives expressions for the wave stress and associated energy radiation to lee waves. The wave stress integrated over the expected (linear) lee-wave scales $2\pi\frac{|f|}{|\mathbf{U}|} < (k,l) < 2\pi\frac{N}{|\mathbf{U}|}$ is

$$\tau = \frac{\rho_0}{4\pi^2}\int\int \frac{\mathbf{k}}{|\mathbf{k}|}P(k,l)\sqrt{[N^2-(\mathbf{k}\cdot\mathbf{U})^2][(\mathbf{k}\cdot\mathbf{U})^2-f^2]}\times \mathrm{sgn}(\mathbf{k}\cdot\mathbf{U})J_0^2\left(\frac{|\mathbf{k}\cdot\mathbf{U_t}|}{\omega_t}\right)dkdl, \quad (3.6)$$

where $\mathbf{k}=(k,l)$ is the horizontal wavenumber, f is the Coriolis frequency, $\mathbf{k}\cdot\mathbf{U}$ is the Doppler-shifted frequency, ω_t is the tidal frequency, $P(k,l)$ is the 2D power spectrum of the abyssal hill topography, and ρ_0 is the seawater density. The parameter J_0^2 is the Bessel function of order 0, and it is dependent on the tidal excursion parameter $|\mathbf{k}\cdot\mathbf{U_t}|/\omega_t$. Previous studies assumed that the barotropic tide is negligible in the ACC and did not remove it from their LADCP profiles [e.g. Sheen et al., 2013; Trossman et al., 2015; Waterman et al., 2013, 2014]. In this study, the barotropic tide was removed from the LADCP profiles and near-bottom current meters, therefore $J_0(|\mathbf{k}\cdot\mathbf{U_t}|/\omega_t)=1$. Consequently, the wave stress (3.6) reduces to

$$\tau = \frac{\rho_0}{4\pi^2}\int\int \frac{\mathbf{k}}{|\mathbf{k}|}P(k,l)\sqrt{[N^2-(\mathbf{k}\cdot\mathbf{U})^2][(\mathbf{k}\cdot\mathbf{U})^2-f^2]}\times \mathrm{sgn}(\mathbf{k}\cdot\mathbf{U})dkdl, \quad (3.7)$$

The Bell Jr [1975] linear lee-wave theory assumes subcritical topography so that criti-

cal/supercritical topography effects are not included in the lee-wave energy radiation. Critical and supercritical topography is defined by the steepness parameter $s = \sqrt{2}NH_{rms}/|\mathbf{U}|$, where H_{rms} is the root-mean-square (rms) height of the multichromatic topography [Nikurashin et al., 2014]. The steepness parameter is a measure of the ratio between topographic height and the expected vertical wavelength of the lee wave. The steepness parameter also indicates when the near-bottom quasi-steady flow does not have enough kinetic energy to override the topographic features; therefore, the topography blocks the flow and does not generate internal waves. The $\sqrt{2}$ is a correction factor that stems from using a multichromatic topography. When a monochromatic topography is used, the steepness parameter reduces to the standard definition $NH/|\mathbf{U}|$, where H is the height of the sinusoidal bump [Nikurashin and Ferrari, 2010b]. In a 3D topography the flow can be blocked and also split and go around topography [Nikurashin et al., 2014]. To account for the critical to supercritical topography with respect to the flow, our stress estimates τ are corrected to

$$\tau = \begin{cases} \tau * (s_c/s)^2, & \text{for } s > s_c \\ \tau, & \text{elsewhere.} \end{cases} \tag{3.8}$$

We use a critical steepness parameter $s_c = 0.4$ to account for the nonlinear blocking and splitting of the flow around topography [Nikurashin et al., 2014].

To estimate the contribution from the eddy flow to the radiation of lee waves, we followed Yang et al. [2018] and decomposed the horizontal velocity $\mathbf{U} = \overline{\mathbf{U}} + \mathbf{U}'$, where $\overline{\mathbf{U}}$ and $\mathbf{U}'$ are the time-mean and eddy components. Similarly, we decomposed the wave stress into a mean and transient component $\tau = \overline{\tau} + \tau'$. The energy radiation (loss) of the quasi-steady total flow into lee-wave generation is then calculated as the work done by the lee-wave drag:

$$E_{lee} = \overline{-\tau \cdot \mathbf{U}}, \tag{3.9}$$

and the energy radiation from the near-bottom eddy flow to lee waves is

$$E'_{lee} = \overline{-\tau' \cdot \mathbf{U}'}. \tag{3.10}$$

Note that the wave stress is a nonlinear function of the total velocity; thus the eddy velocity contributes to the time-mean energy loss through this nonlinear dependence [Yang et al., 2018]. We estimated four-year lee-wave energy radiation time series using the low-pass time series of near-bottom currents $\mathbf{U}$ and stratification N^2 [inferred using the GEMS technique; Chidichimo et al., 2014; Tracey et al., 2013] estimated from the CPIES. We employed only the nearest-to-bottom N^2 time series at each CPIES for the lee-wave energy radiation estimates. To estimate lee-wave energy radiation from the CTD/LADCP data, we followed previous studies [Sheen et al., 2013; Waterman et al., 2013] and reduced high frequency, short vertical wavelength variability in the CTD/LADCP casts by vertically averaging the velocity and stratification over the 1000 m closest to the bottom.

Abyssal hills topography spectrum

The horizontal scales of internal lee waves as predicted from linear theory are determined by the near-bottom flow and stratification: $|f|/|\mathbf{U}| < (k,l) < N/|\mathbf{U}|$. Typical length scales for Drake Passage are $O(10^2 - 10^4)$ m. Goff and Jordan [1988] proposed a stationary, zero-mean, Gaussian-distributed, anisotropic covariance function to model the abyssal hill topography. The covariance function has five parameters describing the amplitude, orientation, characteristic wavenumbers, and Hausdorff dimension of seafloor topography. The model is flat at low wavenumbers and follows a power law at high wavenumbers. The 2D abyssal hill spectral model is defined by

$$P(k,l) = 4\pi\nu H_{rms}^2 |\mathbf{Q}|^{-\frac{1}{2}} [\Gamma(k,l)^2 + 1]^{-(\nu+1)}, \tag{3.11}$$

where ν is the Hurst number, which characterizes the spectral slope at high wavenumbers, H_{rms} is the topography rms, and Γ is the dimensionless norm of $\mathbf{k}$ defined by

$$\Gamma(k,l) = \sqrt{\left(\frac{|\mathbf{k}|}{k_s}\right)^2 \cos^2(\theta - \theta_s) + \left(\frac{|\mathbf{k}|}{k_n}\right)^2 \sin^2(\theta - \theta_s)}, \tag{3.12}$$

where k_s and k_n are the wavenumbers in the strike and normal-to-strike direction of the topography respectively, $\theta = \arctan\left(\frac{k}{l}\right)$ is the angle clockwise from true north to the wavenumber vector, and θ_s is the strike angle measured clockwise from the north. In equation (3.11), $\mathbf{Q}$ is a positive, symmetric matrix expressed in terms of its eigenvalues $k_n^2 \geq k_s^2$ and its normalized eigenvectors $\hat{\mathbf{e}}_n$ and $\hat{\mathbf{e}}_s$

$$\mathbf{Q} = k_n^2 \hat{\mathbf{e}}_n \hat{\mathbf{e}}_n^T + k_s^2 \hat{\mathbf{e}}_s \hat{\mathbf{e}}_s^T. \tag{3.13}$$

Since the eigenvectors are orthogonal (i.e., $\hat{\mathbf{e}}_n^T \hat{\mathbf{e}}_s = 0$), they depend on one orientation parameter, which is chosen to be the azimuth θ_s of $\hat{\mathbf{e}}_s$, the eigenvector in the strike direction [Goff and Jordan, 1988]. Therefore, the 2D anisotropic model becomes

$$P(k,l) = 4\pi\nu \frac{H_{rms}^2}{k_s k_n} [\Gamma(k,l)^2 + 1]^{-(\nu+1)}. \tag{3.14}$$

Nikurashin and Ferrari [2011] used ship-based single-beam echosound data, which provide global along-track 1D topography, and simplified the 2D anisotropic topography spectrum (eq. 3.14) to 1D by assuming isotropy:

$$P(k) \simeq P_0 k^{-\mu+1}, \tag{3.15}$$

where P_0 is the spectral level and $\mu = 2(\nu + 1)$ is the topographic spectral slope at scales between 2 km and 20 km. Nikurashin and Ferrari [2011] suggest that the isotropy assumption in the topographic spectra in eq. 3.15 has minimal implications in the rate of energy transfer from

near-bottom flows to internal lee waves. They assumed that near-bottom flows over abyssal topography, dominated by transient eddies, can span the whole 360° direction during a few eddy turn-over times. Therefore, they concluded that the time-mean radiation is an average over geostrophic flows impinging on rough topography at all possible angles.

Abyssal hills statistical parameters

The statistical parameters (k_n, k_s, θ_s, H_{rms}, and ν) in equation (3.14) needed to estimate the energy radiation to lee waves are obtained from three topographic data sets representing the abyssal hill morphology.

The first data set of statistical parameters is provided by Goff [2020] (G2020, hereinafter), an update from Goff [2010]. The G2020 statistical parameters are based on the most recent global maps of the remotely sensed altimetric gravity field. The updated data set is significantly improved in the lateral and vertical resolution of the global gravity map. Also, regions that previously had a low rms (i.e., where the small-scale gravity variance did not exceed the noise level) are improved. A key aspect of the data set is that it masks distinct features such as seamounts, mid-ocean ridges (e.g. Shackelton Fracture Zone; Fig. 3.1), and continental margins as they do not represent abyssal hills [Goff, 2010]. The statistical parameters are available on a $1^\circ \times 1^\circ$ longitude-latitude grid. Further details about the methodology employed to estimate these parameters can be found in G2020 and Goff [2010]. For estimating E_{lee} (eq. 3.9) and E'_{lee} (eq. 3.10), we assigned the statistical parameters from the grid box that contains each CPIES and CTD/LADCP casts. We exclude those CPIES and casts that are close to the South American or Antarctic shelf breaks, as these topographic features are not abyssal hills. Table 7.1 shows the G2020 statistical parameters used for each CPIES location.

The topographic scales resolved by altimetric gravimetry ($2.5 - 7.0$ km alongtrack spatial resolution) are insufficient for determining the smallest expected lee-wave wavelengths. Hence, a second data set of statistical parameters is determined using the Drake Passage MB data to resolve

these smaller length scales. The statistical parameters of the topographic spectra are estimated using a least-squares fit of the 2D MB autocovariance [Goff and Jordan, 1988]. However, this is only possible at 10 out of the 41 CPIES locations, as either the noise-to-signal ratio from the MB-derived data set is high, or locations are adjacent to mid-ocean ridges, continental margins or sea mounts. The statistical parameters obtained from the MB data are listed in Table 7.1. The H_{rms} estimated from the MB data at these 10 CPIES locations is smaller than that estimated from the G2020 data, except at CPIES C11. The G2020 gravimetric data overestimates the H_{rms} in Drake Passage since it cannot resolve the smaller topographic length scales that contribute to the lee-wave radiation.

Finally, to compare our lee wave energy radiation estimates with that calculated assuming an isotropic abyssal hill topography, we use the eq. (3.15) statistical parameters from Nikurashin and Ferrari [2011] (NF2011, hereinafter). NF2011 analyzed global shipboard single beam echo soundings with an along-track resolution of 2 km in a $3^\circ \times 3^\circ$ grid. A least-squares fit was used to estimate P_0 and μ. Interpolation was used for grid cells where topographic data is absent. Akin to the G2020 data sets, the grid box containing each CPIES location was used to characterize the topographic spectra as in NF2011.

In summary then, the MB and G2020 topographic data sets are used to derive the abyssal hills statistical parameters and represent a 2D anisotropic abyssal hill topographic spectrum (eq. 3.14). The NF2011 topography is used to derive the 1D isotropic form of the Goff and Jordan [1988] topographic model (eq. 3.15).

3.5 Finescale turbulent dissipation and internal wave properties

3.5.1 Spatial variability

Finescale turbulent dissipation rates ε across Drake Passage show a consistent spatial pattern for the different cruises: higher values of ε in the northern half of Drake Passage ($< 58^\circ$ S) indicate more vigorous internal wave activity and mixing due to breaking waves than in the southern part (Fig. 3.2). The southern region shows background dissipation rates $\varepsilon \leq 1 \times 10^{-10}$ W kg^{-1}, whereas in northern Drake Passage $\varepsilon \geq 1 \times 10^{-8}$ W kg^{-1}. The northern Drake Passage elevated dissipation rates are concentrated between 500 and 1500 m depth and in the Polar Front and Polar Front Zone. The Polar Front Zone also exhibits the largest frontal meandering and mesoscale eddy activity in Drake Passage [e.g. Lenn et al., 2011]. Mesoscale eddies in the ACC can modify the propagation of internal waves [Kunze, 1985], which potentially affects the dissipation patterns [Meyer et al., 2015; Sheen et al., 2015]. Near the bottom, the dissipation patterns in each of the different cruises suggest that breaking internal waves are less vigorous, likely because the region exhibits relatively smooth topography except for the stations near the Shackleton Fracture Zone (e.g. C10 in Fig. 3.1). Using alternative limits of integration or the strain-only parameterization yield very similar ε estimates and spatial distribution for all cruises. As an example, Fig. 7.3 shows the comparisons between different parameterizations and limits of integration for cDrake 2010. Our near-bottom turbulent dissipation values are on average an order of magnitude smaller than those from Garabato et al. [2004], who used finescale parameterizations to estimate dissipation from measurements made upstream of our study area. Sheen et al. [2013] also employed finescale parameterizations to estimate dissipation rates upstream of our study area (their T3 transect) and found more homogeneous and higher ε values ($\geq 1 \times 10^{-9}$ W kg^{-1}) in between the Polar Front and the Subantarctic Front compared to our estimates. Although the

sample sizes in these studies are relatively small when studying a highly intermittent process like turbulent mixing, our results together with previous studies [Garabato et al., 2004; Sheen et al., 2013, 2014] point to elevated mixing in Drake Passage relative to background global ocean dissipation.

Global ocean estimates of turbulent dissipation rates made from finescale observations often assume a constant shear-to-strain ratio $R_\omega = 7$ [Kunze, 2017; Kunze et al., 2006], which corresponds to more near-inertial wave frequencies than the Garrett-Munk spectrum for which $R_\omega = 3$. However, our results suggest the frequency content of the internal wave field in Drake Passage, as indicated by R_ω estimates, is less near-inertial and more like Garrett-Munk throughout the water column (Fig. 3.1). There is some variability between years. For instance, the shear-to-strain ratios during 2008 and 2009 (Figs. 3.3b,c) are closer to the Garrett-Munk value in the northern Drake Passage region than in other years. Our results do not show a latitude-dependent frequency content, i.e., that internal waves are more near-inertial moving poleward as found by Sheen et al. [2014], since our R_ω values do not change moving poleward. Shear contamination due to low-stratification [as discussed in section 3.2 and Kunze et al., 2006], could explain the increase in R_ω with latitude observed in Sheen et al. [2014], as the stratification is weaker south of the Polar Front. Our results indicate that for high-latitude regions such as Drake Passage, median values of R_ω are closer to 3-4, in agreement with other estimates in the Southern Ocean [e.g. Meyer et al., 2015; Sheen et al., 2013; Waterman et al., 2013].

3.5.2 Sources of high mixing

We explore possible sources of finescale mixing in Drake Passage by calculating the polarization ratio $\phi_{ccw/cw}$ (eq. 3.5) (Fig. 3.4). The polarization ratio across Drake Passage is rather noisy and shows no latitude or depth dependence, similar to the spatial distribution of R_ω for the different years (Fig. 3.3). However, some patches of high dissipation rates ($\varepsilon > 1 \times 10^{-9}$ W kg^{-1}) in the northern Drake Passage in the upper 1500 m (Figs. 3.2b,c) are associated with

polarization ratios $\phi_{ccw/cw} > 1$ suggesting downward energy propagation. Meyer et al. [2015] showed that larger than average diffusivities were associated with larger than average polarization ratios ($\phi > 1$), related to near-inertial energy in the upper 1000 m at the Kerguelen Plateau in the Indian Ocean sector of the Southern Ocean. The authors associated this larger than average polarization ratio with wind-generated near-inertial waves propagating downwards below the mixed layer. To determine possible sources of high mixing, we constructed average profiles of $\phi_{ccw/cw}$ and R_ω using all estimates of ε and separately for those of high mixing where $\varepsilon > 1 \times 10^{-9}$ W kg^{-1} (Fig. 3.5). We calculated the average profiles as a function of height above the bottom and also with depth in order to distinguish bottom-generated waves from below-mixed-layer-generated waves, respectively. In constructing the median profiles, we used all 177 available CTD/LADCP casts.

Over 50% of the profiles indicate downward energy propagation in the upper 1000 m (blue line in Fig. 3.5a), with median values of the polarization ratio greater than unity. The median shear-to-strain ratio in the upper 1000-m lies between 3 and 4, consistent with Garrett-Munk (blue line Fig. 3.5b). When the shear-to-strain ratio is restricted to high dissipation values, the median exhibits a strong depth dependence, decreasing from a maximum of 5 at 750 m depth to a minimum of 1 at 2000 m depth (red line Fig. 3.5b). The median profiles in the upper 1000 m indicate downward energy propagation with more near-inertial frequency and are consistent with Meyer et al. [2015]. High-amplitude near-inertial wave packets propagating down from the mixed layer, with vertical wavelengths of 200 m, have been observed west of Drake Passage in the upper 1500 m [Kilbourne and Girton, 2015]. The decay of the near-inertial frequency content and the counterclockwise rotation energy (Figs. 3.5a,b) below 1000 m suggests that near-inertial waves dissipate below the base of the ACC baroclinic jet, where the geostrophic shear is the largest. Under these conditions, waves could propagate downwards until they are vertically trapped inside critical layers and dissipate. The near-bottom waves for the all-data (blue lines) and the high-mixing profiles (red lines) are not statistically different and indicate more

clockwise energy polarization ($\phi_{ccw/cw} < 1$) in the 1000 m closest to the bottom (Fig. 3.5c). The R_ω profiles indicate that fewer near-inertial waves are associated with high mixing levels (red line in Fig. 3.5d), whereas over half of the profiles indicate that the waves are less near-inertial and more Garrett-Munk-like (blue line in Fig. 3.5d). These results agree with those of Sheen et al. [2013] and Waterman et al. [2013] who attributed the high mixing patterns to less inertial, upward propagating internal lee waves.

3.5.3 Effect of background shear and stratification

To explore the broad relationship between finescale turbulent dissipation rates and internal-wave frequency content with the background stratification and shear in Drake Passage, dissipation rates and shear-to-strain ratios are bin averaged as a function of shear squared and stratification (Fig. 3.6). Each bin average is calculated using all available 320-m ε and R_ω estimates from the 177 CTD/LADCP profiles with their respective mean shear squared $\overline{V^2}$ and reference stratification $\overline{N}^2$. Bins with less than five estimates (dissipation or shear-to-strain ratio) are omitted. The 1:1 relationship line indicated in Fig. 3.6 marks where the large-scale Richardson number $\text{Ri} = \overline{N^2}/\overline{(\frac{\partial u}{\partial z})^2 + (\frac{\partial v}{\partial z})^2} = 1$.

In general, low-shear, poorly stratified locations are associated with less internal wave activity as shown by the low dissipation values $\varepsilon < 1 \times 10^{-9}$ W kg^{-1} (Fig. 3.6a) and with less near-inertial waves $R_\omega < 5$ (Fig. 3.6b). Mixing due to breaking internal waves increases as the background stratification and shear increases; more near-inertial frequency content is associated with higher mixing (therefore, with higher stratification and shear). The highest stratification and shear levels are found in the upper 1500 m in the northern Drake Passage, within and between the Subantarctic Front and Polar Front (Figs. 3.2,3.3). The higher mixing and more near-inertial energy associated with higher stratification and shear is consistent with wind-generated near-inertial waves propagating down from the mixed layer and dissipating in the upper 1500 m (Figs. 3.5a,b), below the base of the baroclinic fronts.

There is also high dissipation ($\varepsilon > 5 \times 10^{-9}$ W kg^{-1}) associated with Ri$\leq$ 1 (Fig. 3.6). These low, large-scale Ri values are found in and north of the Polar Front in the bottom kilometer (not shown). The estimated Ri values that lie close to the stability threshold of the large-scale flow suggest that turbulent dissipation could occur near the bottom by physical mechanisms other than nonlinear wave-wave interactions, such as shear or convective instabilities; these latter processes are not captured by the finescale parameterization [Polzin et al., 2014]. Therefore, our finescale dissipation estimates, although high in these low Ri regions, may not reflect the full turbulent dissipation near the bottom.

3.6 Lee-wave energy radiation

3.6.1 Topographic roughness

Topographic roughness in Drake Passage relative to the ACC front positions is shown in Figure 3.7. We computed topographic roughness $\hat{H}_{rms}$ by employing eq. (3.14) for the 2D anisotropic topographic datasets of G2020 and MB, and the integral of eq. (3.15) for the 1D isotropic NF2011 dataset, and integrating them over the expect linear lee-wave wavenumber $2\pi\frac{|f|}{|\mathbf{U}|} < (k,l) < 2\pi\frac{N}{|\mathbf{U}|}$. Statistical parameters used for each CPIES location are shown in Table 7.1. Topographic roughness averaged for each frontal region mostly ranges from 60 m to 180 m, although some locations show $\hat{H}_{rms} > 200$ m. Mean and individual topographic roughness estimates are within the typical values found by Sheen et al. [2013] in Drake Passage but an order of magnitude larger than values found by Waterman et al. [2013] in the Kerguelen Plateau region. Mean $\hat{H}_{rms}$ calculated for the 1D isotropic NF2011 and the 2D anisotropic G2020 abyssal hill topographies are not statistically different. The higher spatial resolution of the G2020 topographic roughness shows more variability within the Polar Front Zone than that from the NF2011 topography.

3.6.2 Energy extraction from the total flow into lee waves

We estimate the energy radiation from the total geostrophic flow into lee waves in Drake Passage using the three different topographic datasets and equation (3.9). The steepness parameter is calculated as $s = \sqrt{2}N\hat{H}_{rms}/|\mathbf{U}|$ where $\hat{H}_{rms}$ is shown in Fig. 3.7. We analyze the spatial distribution of the energy radiation across Drake Passage and compare it to the four-year mean low-pass near-bottom circulation (blue arrows in Fig. 3.8a). The three northernmost CPIES (C03, C04 and C20; Fig. 3.1) show strong northward flow associated with the mean position of the Subantarctic Front; the near-bottom flow is steered by the South American continental slope [Gutierrez-Villanueva et al., 2020]. As in Chereskin et al. [2009] and Firing et al. [2016], the strong mean near-bottom currents located in the local dynamics array, i.e. in the Polar Front Zone, are associated with strong meandering of the Subantarctic Front and Polar Front, and transient eddies [Watts et al., 2016]. The one-year averaged currents at the five CPIES adjacent to the Shackleton Fracture Zone show deviation from the surface flow (gray contours in Fig. 3.8a) due to topographic steering.

Here, we only show E_{lee} for the G2020 topography as similar results were obtained when the MB and NF2011 topographies were employed. As expected, the four-year average of lee-wave energy radiation from the total flow is collocated with where the strongest near-bottom currents impinge on rough topography (Fig. 3.8a). E_{lee} is largest where the Polar Front flows over the Shackleton Fracture Zone (243.0 mW m^{-2}, based on one year of data) and in the Polar Front Zone (322.2 mW m^{-2}, based on four years of data). The lowest mean energy estimates (0.91 mW m^{-2}) are found in the Southern Drake Passage, where stratification and currents are the weakest (blue arrows in Fig. 3.8a).

The high-spatial resolution of the local dynamics array in the Polar Front Zone (Fig. 3.1) offers the opportunity to explore the spatial distribution of the energy radiation into lee waves from the total flow. We used the objectively-mapped geostrophic currents at 4000 m depth (black thin arrows in Fig. 3.8a) and an averaged constant stratification $N^2 = 6.38 \times 10^{-7}$ s^{-2}. The

objectively-mapped currents show good agreement with the near-bottom CPIES currents (blue arrows). Our energy-radiation estimates are not significantly different if the mean stratification (calculated at each CPIES location) nearest each mapped grid position is used instead. The energy estimates calculated from the objectively-mapped currents are a factor of 5 smaller than those estimated directly from the near-bottom current meters (filled colored circles Fig. 3.8). The differences are potentially due to the low-pass smoothing and adjusted depth employed for the mapped currents. The Polar Front Zone E_{lee} varies by one order of magnitude. Surprisingly the downstream region of the Polar Front Zone, characterized by a relatively smooth topographic depression (Yaghan Basin in Fig. 3.1), displays relatively large energy radiation ($E_{lee} = 290.25$ mW m^{-2}; Fig. 3.8a), associated with a deep, strong cyclonic circulation (blue and black arrows in Fig. 3.8a).

Table 3.1 shows the mean statistics of the energy radiation from the total flow into lee waves per frontal region using the CPIES near-bottom current and stratification time series. We formed a four-year time series for each frontal region by averaging together the energy radiation estimates from the CPIES located in that region. For the Polar Front, there is only one four-year site (C10, Fig. 3.1) as recall that the H-array CPIES only sampled for 1 year from October 2010 to November 2011. The standard error is calculated as $\sigma/\sqrt{\hat{n}}$, where σ and $\hat{n}$ are the standard deviation and the degrees of freedom respectively. Here $\hat{n}$ is the ratio between the time series length (days) and the decorrelation time scale (days), determined to be the first zero crossing of the autocorrelation function for the time series in each front.

Our frontwise annual lee-wave energy radiation estimates are statistically stable as they show no significant year-to-year variability irrespective of the topography used (Table 3.1). The Polar Front Zone displays the largest lee-wave energy radiation for both the 1D NF2011 and 2D G2020 topographies. In this region, using both topographies we found that over the last sampling period from Oct 2010 - Nov 2011 the average energy radiation drops by 30% with respect to the preceding sampling period. The Polar Front Zone is where the strongest bottom currents occur

(Fig. 3.8a) due to the meandering of the ACC fronts and deep eddy formation [Chereskin et al., 2009]. Hence the drop in the lee-wave energy radiation from Oct 2010 - Nov 2011 is likely a result of less meandering causing a reduction in the mesoscale eddy formation during that period. Nonetheless, when the year-long records from the five H-array CPIES in the Shackleton Fracture Zone (Fig. 3.1) are included over that period (Oct 2010 - Nov 2011) in the Polar Front, the energy radiation increases by a factor of 2-3 over the other sampling periods (Table 3.1).

The four-year energy estimates in this study compare well with those of Brearley et al. [2013], who used a single year-long mooring record from the DIMES program in Drake Passage, located downstream of our region and just south of the Subantarctic Front (Polar Front Zone in our study). That study used a 2D isotropic topography and $s_c = 0.7$, which accounts for flow blocking but not for splitting, therefore, suggesting that their lee-wave energy estimates are potentially biased high. Their annual-mean energy radiation from a single location is an order of magnitude lower than our four-year-mean and individual year-mean radiation estimates in the Polar Front Zone (Table 3.1).

Previous modelling studies that have estimated the lee-wave energy radiation from a global ocean model velocity time series averaged in the 500-1000 m closest to the bottom potentially underestimate the lee-wave radiation from deep flows [Nikurashin and Ferrari, 2011; Scott et al., 2011; Yang et al., 2018]. Nikurashin and Ferrari [2011] estimated lee-wave radiation energy of $14-42$ mW m^{-2} from a global ocean model. Their estimates, however, are more homogeneous across the Drake Passage, whereas ours vary by one order of magnitude across the different frontal regions [see Fig. 2 in Nikurashin and Ferrari, 2013]). The Yang et al. [2018] Drake Passage averaged lee-wave radiation energy estimates determined from the year-long five-day averaged model velocity field are a factor of three smaller than our 1D (NF2011) and 2D (G2020) energy estimates. The Scott et al. [2011] lee-wave energy model estimates are smaller by five-fold than our estimates for the 2D isotropic topography [Goff, 2010].

3.6.3 Energy extraction from the eddy flow into lee waves

We estimate the lee-wave energy radiation from the near-bottom eddy flow E'_{lee} (eq. 3.10) and explore its relationship with the near-bottom EKE in Drake Passage. The lee-wave energy radiation from the eddy flow and the EKE are calculated using the near-bottom current meters and mapped geostrophic velocities (Fig. 3.8b). The easternmost-sampled region of the Polar Front Zone shows the smallest contribution of the energy radiation from the eddy flow to the total flow ($\% E'_{lee}/E_{lee}$; small inset in Fig. 3.8b); the energy radiation due to the mean cyclonic circulation in the Yaghan Basin contributes almost half of the total E_{lee}. Conversely, the largest energy radiation due to eddies is localized close to the Shackleton Fracture Zone (H-array) and collocated with the maximum near-bottom EKE (Fig. 3.8b, non-filled contours). In the western half of the sampled region of the Polar Front Zone, eddies are the major contributor to the generation of lee waves; lee-wave energy due to eddies is of the same magnitude as the total-flow energy radiation. This maximum lee-wave energy radiation due to the eddy flow coincides with the maximum poleward (divergent), horizontal eddy heat flux estimated by Watts et al. [2016]. This horizontal flux caused by strong depth-independent currents crossing the upper baroclinic jet at an angle (and so favoring the growth of meanders of the ACC fronts) indicates baroclinic instability processes [Watts et al., 2016].

The deep EKE in the Polar Front Zone shows a similar distribution to that of the surface EKE [Foppert et al., 2017], with a second maximum located downstream (Fig. 8b). The lee-wave energy radiation due to the eddy flow also shows patchy, but large values in the downstream region. While baroclinic instabilities dominate the eddy formation and growth in the upstream region, their growth is truncated downstream [Foppert, 2019]. Foppert [2019] suggested that barotropic instabilities (downgradient horizontal eddy momentum fluxes) provide a non-negligible path for eddies to grow by extracting kinetic energy from the mean flow and converting it to EKE. Mesoscale eddies generated by instability of the ACC are thought to lose energy through several mechanisms. Yang et al. [2018] showed that lee-wave radiation significantly weakens

the eddy flow where the near-bottom eddy flow interacts with rough topography. The loss of energy from the eddy flow to lee waves may limit or taper the amount of energy available for eddy growth through baroclinic instabilities (conversion from potential energy to EKE) and barotropic (conversion from mean KE to EKE). The potential influence of lee-wave radiation on the energy pathways of the ACC and its implications for the MOC deserves further investigation.

3.6.4 Time variability

The four-year time series of near-bottom currents and stratification offer an opportunity to investigate the time variability of the lee-wave radiation across Drake Passage. As for Fig. 3.8, here we only show results for the G2020 topography as similar patterns were obtained when using the NF2011 topography. The time series of E_{lee} (total flow) and s/s_c are shown in Figure 3.9. Selected stations representative of each frontal region are displayed along with time series of EKE and KE (solid gray line and dashed red line, respectively, Fig. 3.9a-d). In the Subantarctic Front and Polar Front Zone, EKE $\geq$ KE for most of the four-year records; this relationship does not hold for the Polar Front and Southern Drake Passage regions. As expected, there is a strong correspondence between E_{lee} and the near-bottom EKE and KE. In the Subantarctic Front and Polar Front Zone, E_{lee} has larger time variability as the mesoscale activity is more vigorous than in the Southern Drake Passage. More energy estimates that fall in the subcritical topography $s < s_c$ are found in the Polar Front Zone and Polar Front as the near-bottom flow is strong enough to override the rough topography, therefore, radiate more lee waves.

Interannual variability of the expected E_{lee} is evidently correlated to that of EKE and KE. The greatest changes in EKE (therefore, in the expected E_{lee}) are found in the Subantarctic Front and Southern Drake Passage (Fig. 3.9a,d). For instance, lower than average EKE corresponds with a decrease in predicted internal lee-wave radiation during the first half of 2010 in the Subantarctic Front and western Polar Front Zone (Fig. 9a,b). The weaker flow during this period results in more topographic blocking and splitting of the near-bottom currents, resulting in weaker lee-wave

energy radiation. It is unlikely that the decrease of predicted lee-wave radiation during 2010 could be due to a migration of the fronts; no southern migration of the fronts has been found in Drake Passage [e.g. Kim and Orsi, 2014]. Investigating the physical mechanisms driving interannual variability of near-bottom KE and EKE (thus in expected lee-wave radiation) is beyond the scope of this study; nevertheless, it warrants future work.

3.7 Effects of isotropic and anisotropic topography

3.7.1 Energy radiation estimates

To study the effect of different topographies, we compare the lee-wave energy radiation using the 1D isotropic abyssal hills topography of NF2011 and that calculated using the G2020 and MB 2D anisotropic topographies (Fig. 3.10). We include the CTD/LADCP energy estimates (non-filled symbols in Fig. 3.10) and plot them with the 4-year near-bottom CPIES estimates (colored dots in Fig. 3.10). Only C07 is shown; other CPIES show similar results (Fig. 7.4). We also compared our energy estimates calculated using the NF2011 statistical parameters and those calculated using the G2020 statistical parameters averaged on a coarse $3^\circ \times 3^\circ$ box centered at each CPIES location. However, our results (not shown) are insensitive to the averaging of the G2020 parameters using a similar coarse resolution grid to that of the NF2011 topography. For energy estimates $E_{lee} > 10^{-3}$ mW m^{-2}, the lee-wave energy radiation is not sensitive to the choice of topography. The relationship between the lee-wave energy radiation estimates calculated using G2020 versus NF2011 topography (blue dots in Fig. 3.10) and MB versus NF2011 case (red dots in Fig. 3.10) shows that most of the dots fall within the one order of magnitude discrepancy (dashed lines in Fig. 3.10), except for a small percentage ($< 10\%$) of dots for the NF2011 vs G2020 and MB cases (blue and red dots respectively); these small clusters show NF2011 energy estimates being larger than the G2020 and MB estimates by more than three-fold. Although the cases are fewer, the CTD/LADCP estimates (black triangles and squares in Fig. 3.10) exhibit the

same behavior as the CPIES energy estimates and occasionally are larger than those obtained by the CPIES.

This study shows that the energy estimates are not sensitive to the choice of abyssal hill topography. Yang et al. [2018] showed that artificially changing the 2D anisotropic bathymetry to an isotropic form can lead to an increase in the energy radiation estimates up to an order of magnitude in Drake Passage. Our comparison between the NF2011 1D topography and G2020/MB topography are within the Yang et al. [2018]'s range of discrepancy. We only find a small cluster with 2-3 orders of magnitude discrepancy between the 1D isotropic NF2011 and the 2D anisotropic G2020, in agreement with that determined by Trossman et al. [2015] using the CTD/LADCP casts from both the Southern Ocean finestructure experiment (SOFine) near the Kerguelen Plateau [Waterman et al., 2013, 2014] and from the DIMES experiment near Drake Passage [Sheen et al., 2013]. Since Sheen et al. [2013] employed a 1D isotropic topography and only corrected their estimates for nonlinear blocking (but not for splitting), their energy radiation could potentially be overestimated.

We compare the energy radiation estimates calculated using the CTD/LADCP casts with those estimated from the CPIES near-bottom current meter and stratification at each CPIES location, employing the three topographic data sets (Fig. 3.11). Here, each pointwise CTD/LADCP estimate is compared to the nearest CPIES estimate in space, averaged over a five-point window in time centered at the time of the CTD/LADCP cast. We expect differences in our results since the CTD/LADCP estimates represent a snapshot averaged over 1000 m, whilst the CPIES estimates are obtained from near-bottom $\mathbf{U}$ and inferred N^2 at about 50 m above the bottom. The energy radiation estimates determined using the CPIES and the CTD/LADCP casts agree within two orders of magnitude using the three different bathymetries when both the CTD/LADCP and CPIES estimates are larger than 10^1 mW m^{-2}. The slope of the best fit in $\log_{10}$ scale using only those estimates that agree within one order of magnitude is less than one for both NF2011 and G2020 topographies (blue and red solid lines in Fig. 3.11, respectively), which indicates that the

CPIES estimates are generally larger than the CTD/LADCP estimates. As both energy estimates decrease (i.e., moving down along the 1:1 line in Fig. 3.11), the differences can be up to 6 orders of magnitude.

We also calculated the mean and standard error of the lee-wave energy radiation from CTD/LADCP and CPIES estimates (shown in Fig. 3.11) over the five cDrake cruises for each of the five frontal regions (Table 3.2). The standard error is calculated as $\sigma/\sqrt{n}$, where σ is the standard deviation and $n = 5$ is the number of cDrake cruises (i.e., degrees of freedom), using both the G2020 and NF2011 topographies. Not surprisingly, the CPIES energy estimates are higher than the CTD/LADCP estimates regardless of the topography used. The vertical averaging of the horizontal currents from the LADCP cast used to calculate the slowly variant near-bottom flow likely underestimates the energy radiation; the low-pass-filtered CPIES current better captures the geostrophic flow thought to be the main driver for lee-wave generation.

The Polar Front Zone and Subantarctic Front exhibit the largest lee-wave energy radiation estimates in Drake Passage for both G2020 and NF2011 topographies (Table 3.2). Sheen et al. [2013] estimated O(1-10) mW m^{-2} energy radiation estimates from CTD/LADCP casts in the Scotia Sea (downstream of Drake Passage) using a 1D isotropic topography spectrum (their estimates are corrected only for blocking, but not for splitting of the flow). Our estimates in the Polar Front Zone fall are one order of magnitude larger than those obtained by Sheen et al. [2013] in the same frontal region, for the Scotia Sea (Table 3.2). The lower Sheen et al. [2013] estimates are potentially a consequence of quiescent mesoscale activity during their sampling period. Our study includes samples both along and across the Polar Front Zone in Drake Passage, and the stations are repeated five times, allowing better characterization of the deep flows and therefore also of the lee-wave energy radiation with more statistical robustness. Similar energy radiation estimates to ours are found by Waterman et al. [2013] for both instantaneous and transect-averaged cases over relatively smooth (1D isotropic) topography ($\hat{H}_{rms} < 40$ m) in the Kerguelen Plateau area.

3.7.2 Subcritical-to-supercritical topography

Figure 3.12 shows the bivariate probability distribution function of the steepness parameter s with respect to the flow and the geostrophic streamfunction Ψ in Drake Passage using the near-bottom current meters and stratification from the CPIES time series. In general, the steepness parameter distribution is similar for both the 2D anisotropic GF2020 (Fig. 3.12a) and the 1D isotropic NF2011 (Fig. 3.12b); the 5-95 percentiles interval spans $0.20 \leq s \leq 5$, however, s has been known to be as large as $O(10)$ [Yang et al., 2018]. Both the 1D isotropic and 2D anisotropic cases show that for the Subantarctic Front and within the Polar Front, more data falls within the critical/supercritical topography ($s \geq s_c$), where topographic blocking and/or flow splitting effects limit the energy radiation to lee waves. In contrast, subcritical topography ($s \leq s_c$) dominates within the Polar Front Zone for either topography. If a $s_c = 0.70$ is used (instead of $s_c = 0.4$), more estimates in the Polar Front Zone fall within the subcritical topography for the NF2011 topography (Fig. 3.12b) than for the G2020 (Fig. 3.12a). This is partly because the larger $s_c = 0.7$ only accounts for the topographic blocking but not for splitting. The Polar Front Zone coincides with where the highest mesoscale activity is found in Drake Passage [Foppert et al., 2017]. Strong bottom flows ($0.20 - 0.40$ m s^{-1}), due to the meandering of the ACC fronts and deep eddy formation in the Polar Front Zone [Chereskin et al., 2009], impinge on the relatively smooth topography potentially contributing to the subcritical topography in this region.

The s estimated using the near-bottom CTD/LADCP current speed and stratification for the G2020 and NF2011 topographies (open black squares in Fig. 3.12) mostly fall within the critical and supercritical topography everywhere in the Drake Passage. For G2020, only three casts located in the Polar Front Zone are in the subcritical topography (Fig. 3.12a). Around 20% (37) of all casts are in the subcritical topography for the NF2011 topography, with the biggest cluster found in the Polar Front Zone (Fig. 3.12b). All stations for the MB s (open magenta circles in Fig. 3.12) are in the supercritical topography. Having a time series of near-bottom current and stratification allows us to characterize the time-variable steepness parameter s in Drake Passage

at more statistical robaustness than was attainable in previous studies.

3.8 A simple energy budget

We calculate the fraction of lee-wave energy that is locally dissipated through nonlinear wave-wave breaking (Fig. 3.13). We integrated the finescale dissipation estimates from near the bottom to the base of the second mixed layer (see section 2.1). In interpreting our results, caution is advised as turbulent mixing is not only caused by breaking lee waves; for example, downward-propagating near-inertial internal waves breaking near the pycnocline can also enhance turbulent dissipation [Meyer et al., 2015]. Also, waves generated upstream can travel horizontally [Baker and Mashayek, 2021] or can be advected by the geostrophic flow [Waterman et al., 2021, 2014], and dissipate downstream of topography [Zheng and Nikurashin, 2019], therefore breaking the assumption that lee wave energy dissipates locally. Advection by the flow and remote dissipation are more likely to occur in and north of the Polar Front where the strongest flows are found.

The ratio between turbulent dissipation and lee-wave energy radiation indicates that on average only a small percentage ($< 10\%$) of the lee-wave energy dissipates locally, regardless of the topography employed for CPIES and CTD/LADCP estimates (gray symbols in Fig. 3.13a,b,c). Although a small fraction of the expected lee-wave energy estimates are sensitive to the choice of topography, the percentage of lee-wave energy locally dissipated remains invariant to topography. Furthermore, these expected energy estimates are too small to significantly impact the energy budget. Using the strain-only finescale estimates of turbulent dissipation only brings the percentage up to 30% (Fig. 7.5a), and is $< 10\%$ when the shear-strain parameterization with alternative limits is employed (Fig. 7.5b). The small percentage agrees with Sheen et al. [2013] who found an order of magnitude discrepancy between their direct estimates of turbulent dissipation from VMPs integrated in the bottom kilometer and lee-wave energy radiation estimates at a site upstream of our study. However, perfect agreement between lee-wave energy radiation

and local dissipation is not expected. Nikurashin and Ferrari [2010b] showed from numerical simulations using parameters tuned for Drake Passage [Garabato et al., 2004] that the ratio of turbulent dissipation vertically integrated over the bottom kilometer and the energy extracted by the lee waves from the geostrophic flow is 50% for critical to supercritical topography, reducing even further to $\sim 10\%$ for subcritical topography. Despite doing a full-water-column integration of the turbulent dissipation estimates, our results show that the percentage is smaller than that obtained by Nikurashin and Ferrari [2010b] for critical-supercritical topography. When subcritical topography ($\log_{10}(s/s_c) \leq 0$ in Fig. 3.13a-c) dominates (therefore, linear lee-wave theory applies), the percentage of lee-wave energy that dissipates locally ($< 10\%$) is consistent with Nikurashin and Ferrari [2010b]. Waterman et al. [2014] found that finescale parameterizations overpredict their estimates of turbulent dissipation at a subset of locations where large lee-wave energy radiation coincides with upward propagating, high-frequency internal waves and shear profiles with maximum values near the bottom and decreasing with height (above the bottom). It is unlikely that the omission of inertial oscillations in the linear lee-wave theory brings the lee-wave energy radiation closer to the local dissipation, since the modified theory that takes account of energy lost to inertial oscillations is thought to reduce the energy available for lee waves by only 15% [Nikurashin and Ferrari, 2010a]. Therefore, the excess lee-wave energy must either propagate or be advected by the geostrophic flow and dissipate elsewhere [Zheng and Nikurashin, 2019] and/or be reabsorbed back into the mean flow [Kunze and Lien, 2019]. On the other hand, including the interaction of the barotropic tide harmonics with the near-bottom flow [Shakespeare, 2020] may reduce the expected lee-wave energy radiation, thus bringing the energy radiation closer to the energy dissipated locally.

An inverse relationship is observed between the fraction of energy radiation and subcritical/critical topography: the more subcritical the topography is, the larger the lee-wave energy radiated (Figs. 3.13a,b,c, blue shading). Conversely, critical-to-supercritical topography dominates for small energy radiation to lee waves for both NF2011 (1D isotropic) and G2020 (2D

anisotropic) (Fig. 3.13a,b), and also for the MB (2D anisotropic) topography (Fig. 3.13c) although fewer stations are available. While turbulent dissipation varies by two orders of magnitude, the lee-wave energy radiation varies by almost six orders of magnitude. The fraction of energy locally dissipated, therefore, is limited predominantly by the saturation of the energy flux due to topographic blocking and splitting. As discussed by Nikurashin and Ferrari [2010b], when the bottom flow does not have enough kinetic energy to surmount large topography ($s \geq s_c$), the stagnant fluid downstream and below the height of the topographic feature thickens and so reduces the vertical displacement of the water flowing on top of it. Consequently, the lee-wave energy radiation saturates. It is possible that this critical-to-supercritical topography with respect to the flow drives highly nonlinear breaking downstream of the topography (due to nonradiating internal waves and acceleration of the flow in these regions), which could be higher than that for the subcritical topography [Klymak, 2018; Klymak et al., 2021]. Whether this breaking downstream of topography could be suitable for weakly nonlinear wave-wave cascade of energy and breaking requires further investigation.

Trossman et al. [2015] noted that pointwise discrepancies between lee-wave energy estimates and direct estimates of dissipation in the SOFine and DIMES regions can be large. However, the authors found that statistical agreement between the energy estimates and dissipation rates is achieved when averaging all locations and when the 2D anisotropy is accounted for in the abyssal hill topographic spectrum. Here we take a similar approach and averaged our energy E_{lee} and depth-integrated ε estimates by frontal region. The front-wise averaging potentially reduces the nonlocal effects, such as wave advection and mean flow-wave interactions of the energy and dissipation estimates; these effects are not encapsulated in the Bell Jr [1975] theory and finescale parameterizations [Waterman et al., 2014]. Our results are shown in Figure 3.13d for the CPIES (circles) and CTD/LADCP (triangles). For the CPIES estimates, both NF2011 and G2020 topographies (blue and red circles, Fig. 3.13) show one-to-two orders of magnitude higher energy conversion over the dissipation within all frontal regions. Notably, the CTD/LADCP energy

estimates for the NF2011 topography (blue triangles circles, Fig. 3.13) show better agreement with the depth-integrated inferred dissipation than the CPIES estimates. In the Southern Drake Passage, dissipation exceeds the expected lee-wave energy radiation by a factor of 2, which is likely owing to the fact inferred dissipation is not only due to lee waves breaking at their site of generation.

3.9 Conclusions and summary

Radiation and breaking of internal lee waves are thought to play a significant role in the energy budget of the Southern Ocean. However, uncertainties remain regarding the amount of energy converted from ACC deep flows into lee waves and how much of this energy dissipates locally. In this study we analyzed the spatial distribution of finescale turbulent mixing and internal lee-wave energy radiation in Drake Passage using three different abyssal hill topographies. Moreover, we quantified the percentage of radiated lee-wave energy that dissipates locally from near-the-bottom to the based of the pycnocline. Turbulent dissipation was estimated using a shear-to-strain finescale parameterization calculated from a series of CTD/LADCP casts at repeated locations across Drake Passage. Drake Passage is a known hot spot of internal wave activity and breaking. Our results consistently showed higher turbulent dissipation due to breaking internal waves north of the Polar Front. In the upper 1500 m, higher dissipation was associated with downward propagating near-inertial waves dissipating in the thermocline of the Subantarctic Front and Polar Frontal Zone. However, we found that turbulent dissipation was less vigorous near the bottom across much of Drake Passage, mainly due to the relatively smooth topography in our study region. The internal wave frequency content in Drake Passage is less near-inertial than what was assumed for the global ocean by Kunze [2017] who used $R_\omega = 7$ (i.e., $\omega \sim 1.15f$).

The energy extraction from the geostrophic flow to internal lee waves across Drake Passage was estimated using a unique four-year time series of near-bottom currents and stratification from

an array of CPIES. The Bell Jr [1975] linear lee-wave theory, corrected for critical to supercritical topography with respect to the flow, was used to determine the lee-wave energy radiation using both near-bottom current meter and CTD/LADCP casts. Lee-wave energy was calculated from three abyssal hill topographies: two were 2D anisotropic (G2020 and MB), and one was 1D isotropic (NF2011). The Polar Front Zone comprises multiple strong deep flows associated with the frequent meandering of the Subantarctic Front and Polar Front. These strong flows impinging over small abyssal hills characterized subcritical topography for generating lee waves (and therefore more linear energy radiation). In the Southern Drake Passage region, the energy radiation was small due to weaker flow and stratification.

Lee-wave radiation was collocated with strong near-bottom EKE. The maximum radiation of lee-wave energy was localized in the Polar Front and the Polar Front Zone. In the Polar Front Zone, the maximum expected radiation was collocated with a maximum in downgradient eddy heat flux observed by Watts et al. [2016]. A second maximum in the expected lee-wave radiation was localized downstream (in the Polar Front Zone), and coincided with a second EKE maximum. Yang et al. [2018] showed that radiation of lee waves due to the interaction of the deep ACC flow with topography represents an important sink of EKE in a year-long global climate model output. Our estimates from observations also indicated significant loss of energy from the eddy flow to lee waves. Further work with idealized simulations with lee-wave-resolving resolution could further clarify and quantify the effect of lee-waves on the Southern Ocean EKE pathways.

This study was motivated by previous studies [Trossman et al., 2015; Yang et al., 2018] that suggested that estimates of lee-wave energy radiation and near-bottom turbulent dissipation in the ACC potentially come to a close agreement (less than one order of magnitude in discrepancy) by employing a two-dimensional anisotropic abyssal hill topography. Previous studies estimated lee-wave energy radiation by assuming an isotropic topography in Drake Passage [Sheen et al., 2013] and the Kerguelen Plateau [Waterman et al., 2013]; these studies found an order of magnitude discrepancy between their lee-wave energy estimates and turbulent dissipation. In contrast, the

statistical parameters from the G2020 gravimetric and MB data used in our study showed that the abyssal hills in Drake Passage are highly anisotropic, as $k_n > k_s$ by a factor of 4-5. Trossman et al. [2015] suggested that, while pointwise discrepancies between the expected lee-wave energy and dissipation estimates were large (without statistical agreement), averaged energy estimates and direct estimates of dissipation from VMPs were in statistical agreement when the 2D anisotropy was accounted for in the abyssal hill topographic spectrum. Our study showed that on average less than 10% of the lee-wave energy radiation dissipated locally regardless of the abyssal hill topography employed. Nikurashin and Ferrari [2010b] found that for critical to supercritical topography ($s \geq s_c$), numerical simulations showed that half of the radiated energy dissipates locally in Drake Passage, and it reduced to $\sim 10\%$ for subcritical topography. Our study showed that lee-wave energy estimates were one to two orders of magnitude larger than the local turbulent dissipation for both 1D isotropic and 2D anisotropic bathymetries, in agreement with the expected percentage found by Nikurashin and Ferrari [2010b] for subcritical-to-supercritical topography. This excess of wave radiation was associated with critical to subcritical topography, i.e. more linear lee-wave energy radiation. The percentage of expected lee-wave energy that locally dissipates by wave-wave cascade does not increase even if turbulent dissipation is integrated from the bottom to the base of the pycnocline. In the absence of critical layers, upward-propagating lee waves can reflect back from the base of the pycnocline, and energy transfer from the sheared flow to the waves is enhanced, therefore, enhancing wave breaking and mixing [Baker and Mashayek, 2021].

Several caveats come with this study. Some of the near-bottom current meters may have been located within the bottom boundary layer. The lack of direct estimates of turbulent dissipation prevented us from estimating true dissipation rates due to breaking internal waves. Mean dissipation rates could be substantially biased due to sampling in a hot spot of turbulent mixing [Klymak, 2018]. Some of our dissipation estimates from finescale parameterizations were inherently overpredicted due to physics that are not encapsulated by the parameterization

[Waterman et al., 2014]. Also, the statistical representation of the abyssal hill topography might be inaccurate for some regions in Drake Passage; the MB data revealed topography that is smoother compared to the single-beam (NF2011) and satellite gravimetry (G2020). For example, the Polar Front Zone is characterized by abyssal plains rather than by abyssal hills. In this region, the energy sink due to the bottom boundary layer might have been more important than lee-wave generation. Higher precision mapping of the global ocean topography is required for more accurate statistical representations of the abyssal topography, thus enabling more realistic representations of the energy deposition from geostrophic flows to lee waves.

Despite the above-mentioned limitations, the main take-away of this study suggests that only a small percentage of the expected lee-wave energy dissipated locally in the full-water column through nonlinear wave-wave interaction, as also found in various recent studies [Brearley et al., 2013; Nikurashin and Ferrari, 2010a; Sheen et al., 2013; Waterman et al., 2013]. Specifically, the finding that the scatter between the amount of energy radiated and local dissipation remained invariant even if the full 2D anisotropic topography was employed showed that the lack of isotropy was not a definitive aspect for explaining the small fraction of theoretical lee-wave energy radiation that dissipates locally. Therefore, our study suggests that alternative fates must be considered for the paths of the excess lee-wave energy. The theoretical lee-wave energy could be either advected by the geostrophic flow and dissipate elsewhere [Zheng and Nikurashin, 2019] and/or be reabsorbed back into the mean flow [Kunze and Lien, 2019]. In addition, the interaction of the slowly-variant flow with the barotropic tide over small-scale abyssal hill topography could suppress the energy radiated into lee waves [Shakespeare, 2020]. Future work using idealized numerical simulations tuned for the range of parameters (such as steepness) found in this study could shed light on the fates of the excess of lee-wave energy radiation.

3.10 Acknowledgments

The authors thank Maxim Nikurashin for providing the Nikurashin and Ferrari [2011] abyssal hills statistical parameters. We thank two reviewers and the editor whose insightful comments greatly improved the manuscript. The Global Multi-Resolution Topography (GMRT) Synthesis gridded bathymetry is hosted at Lamont-Doherty Earth Observatory of Columbia University, and is available at https://www.gmrt.org/GMRTMapTool/. The 1992-2012 Maximenko et al. [2009] Mean Dynamic Topography is available at https://apdrc.soest.hawaii.edu/projects/DOT. cDrake data are available from the National Centers for Environmental Information (NCEI): CTD/LADCP (https://www.ncei.noaa.gov/archive/accession/SIO-cDrake-LADCP) and CPIES (https://www.ncei.noaa.gov/archive/accession/0121256/). cDrake was a collaboration between investigators at the University of Rhode Island and Scripps Institution of Oceanography. The measurements presented here were made with support provided by the National Science Foundation (NSF) Office of Polar Programs grants ANT-0636493 and ANT-0635437. We wish to thank Kathy Donohue, Randy Watts, Karen Tracey, Erran Sousa, Gerard Chaplin, and Dan Holloway for their ancillary roles and support for the cDrake project. We particularly thank Yvonne Firing for providing the objectively mapped CPIES data in the local dynamics array and Annie Foppert and Karen Tracey for providing the GEMs. The code for the LADCP velocity inversion method is maintained by Andreas Thurnherr and is available online at https://www.ldeo.columbia.edu/~ant/LADCP.html. We are grateful to the captains and crew of the RVIB Nathaniel B. Palmer. MOGV is grateful for financial support from the UC Mexus-Conacyt during his Ph.D. degree. The NSF Awards OCE-1755529 and OPP-2001646 support MOGV, JS, TKC, and this research.

Chapter 3, in full, is a reprint of the material as it appears in Gutierrez-Villanueva, M. O., Chereskin, T. K., Sprintall, J., and Goff, J. A. (2022). Turbulent mixing and lee-wave radiation in Drake Passage: Sensitivity to topography. Journal of Geophysical Research: Oceans, 127,

e2021JC018103, https://doi.org/10.1029/2021JC018103. The dissertation/thesis author was the primary investigator and author of this paper.

Table 3.1: Mean ± standard error lee-wave energy radiation estimates [mW m^{-2}] per frontal region calculated from the CPIES near-bottom currents and stratification time series for five sampling periods demarcated by the beginning of each cDrake cruise. Decorrelation time scales [days] are included. Estimates for the Polar Front that also include the one-year-long H-array are given in the footnotes. Bold numbers indicate that E_{lee} for that specific sampling period is statistically different from other sampling periods for the same abyssal hill topography. Four-year-long mean E_{lee} (Nov 2007 - Nov 2011) in the Polar Front Zone and Southern Drake Passage marked with asterisks indicate that E_{lee} calculated using the NF2011 topography is statistically different than that calculated with the G2020 topography.

			E_{lee} [mW m^{-2}]				
Frontal region	Topography	Decorrelation time scale [days]	Nov 2007 - Nov 2011	Nov 2007 - Nov 2008	Nov 2008 - Nov 2009	Nov 2009 - Oct 2010	Oct 2010 - Nov 2011
Subantarctic Front (SAF)	NF2011	68	23.72 ± 7.21	22.73 ± 7.24	32.86 ± 10.51	26.28 ± 6.26	12.52 ± 3.18
	G2020	50	35.21 ± 6.89	29.64 ± 6.06	51.22 ± 9.74	35.86 ± 5.22	20.30 ± 3.43
Polar Front Zone (PFZ)	NF2011	27	$42.20 \pm 7.84^{*}$	55.25 ± 9.38	50.79 ± 9.17	35.98 ± 5.85	28.74 ± 5.11
	G2020	29	$58.25 \pm 6.49^{*}$	66.74 ± 6.96	67.43 ± 7.19	$\mathbf{52.70 \pm 5.02}$	$\mathbf{37.27 \pm 3.40}$
Polar Front (PF)	NF2011	49	7.66 ± 4.20	7.33 ± 2.65	3.02 ± 1.51	11.01 ± 6.51	9.33 ± 4.41[a]
	G2020	54	13.60 ± 3.62	14.87 ± 2.74	$\mathbf{6.00 \pm 1.72}$	16.47 ± 4.83	17.06 ± 4.27[b]
Southern Drake Passage (SDP)	NF2011	76	$2.87 \pm 0.90^{*}$	1.43 ± 0.37	1.80 ± 0.53	3.53 ± 0.81	4.43 ± 1.37
	G2020	63	$4.20 \pm 0.88^{*}$	2.73 ± 0.36	3.32 ± 0.61	5.14 ± 0.72	5.92 ± 1.15

[a-b] $\mathbf{26.15 \pm 5.78}$ and $\mathbf{35.70 \pm 4.33}$ when the H-array is included.

Table 3.2: Mean ± standard error lee-wave energy radiation estimates [mW m^{-2}] per frontal region calculated from currents and stratification from the contemporaneous CPIES and CTD/LADCP estimates shown in Figure 3.11. Estimates for the Polar Front that also include the one-year-long H-array are given in the footnotes. Bold numbers indicate that CPIES energy estimates are statistically different from the CTD/LADCP estimates when using the same abyssal hills topography.

	G2020		NF2011	
	CPIES	CTD/LADCP	CPIES	CTD/LADCP
Frontal region	[mW m^{-2}]	[mW m^{-2}]	[mW m^{-2}]	[mW m^{-2}]
Subantarctic Front (SAF)	56.15 ± 22.24	29.51 ± 22.98	$\mathbf{36.47 \pm 12.24}$	$\mathbf{14.39 \pm 6.90}$
Polar Front Zone (PFZ)	59.48 ± 24.49	39.44 ± 5.66	21.25 ± 10.06	15.38 ± 2.98
Polar Front (PF)	9.26 ± 5.25[a]	8.82 ± 4.40[b]	$\mathbf{15.82 \pm 1.69}$[c]	$\mathbf{5.10 \pm 3.77}$[d]
Southern Drake Passage (SDP)	4.97 ± 0.72	5.90 ± 3.52	$\mathbf{3.36 \pm 1.53}$	$\mathbf{1.42 \pm 0.70}$

[a-d] $\mathbf{52.42 \pm 38.98}$, $\mathbf{11.63 \pm 4.65}$, $\mathbf{36.23 \pm 20.56}$, and $\mathbf{5.73 \pm 1.93}$ when the H-array is included.

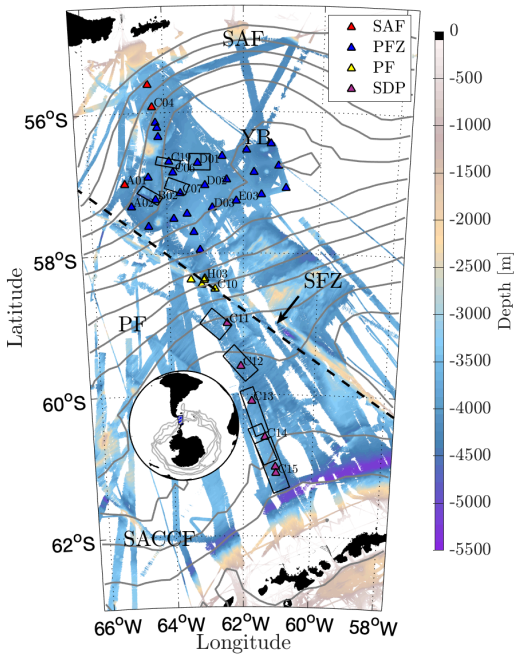

Figure 3.1: Area of study shown in Lambert projection. Filled triangles show the position of the CPIES and CTD/LADCP casts. Locations are color-coded by their position relative to the ACC fronts: red, blue, yellow and magenta triangles show the CPIES locations within the Subantarctic Front (SAF), Polar Front Zone (PFZ), Polar Front (PF) and Southern Drake Passage (SDP) area. Gray thick lines show the mean dynamic topography by Maximenko et al. [2009]. The colored background shows the multibeam bathymetry from the GMRT synthesis [Ryan et al., 2009]. The 3×7 CPIES local dynamics array is located in the Polar Front Zone between the mean position of the SAF and PF. The Shackleton Fracture Zone (SFZ; thick dashed line) is indicated. The central position of the Yaghan Basin (YB), a topographic depression, is indicated. Black boxes delineate where statistical parameters were calculated using the multibeam data (see Table 7.1).

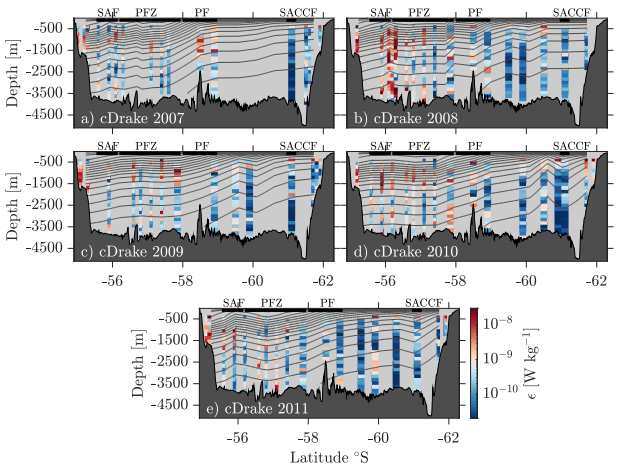

Figure 3.2: Across Drake Passage sections along the cDrake C-Line of finescale dissipation rates of turbulent kinetic energy ε [W kg^{-1}] for a) November 13-December 7 2007, b) November 19-December 13 2008, c) November 19-December 19 2009, d) October 23-November 15 2010, and e) November 18-December 11 2011. Dark gray patches show the MB bathymetry. Each profile corresponds to one CTD/LADCP cast. Thick black bars along the top axis show the mean position of the ACC fronts (Fig. 3.1). The buoyancy contours averaged for the duration of each cDrake cruise are shown in gray contours. Buoyancy contours are plotted in the range of 1×10^{-3} m s$^{-2} \leq 0.6 \times 10^{-3} \leq 1.4 \times 10^{-3}$ m s^{-2}.

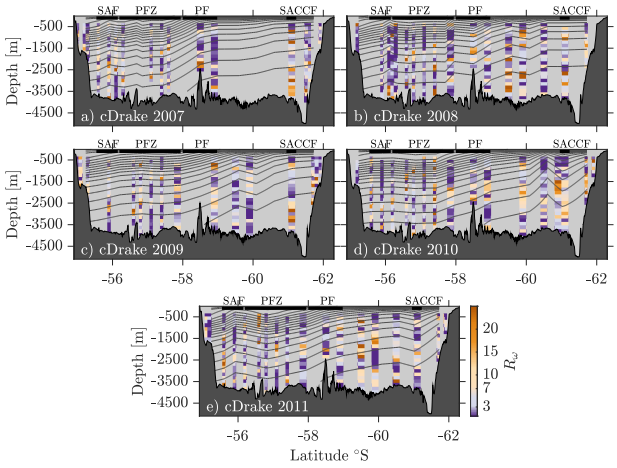

Figure 3.3: Across Drake Passage sections along the cDrake C-Line of shear-to-strain ratio R_ω for a) November 13-December 7 2007, b) November 19-December 13 2008, c) November 19-December 19 2009, d) October 23-November 15 2010, and e) November 18-December 11 2011. $R_\omega = 3$ is the canonical Garrett-Munk ratio (purples). Thick black bars along the top axis show the mean position of the ACC fronts (Fig. 3.1). The buoyancy contours averaged for the duration of each cDrake cruise are shown in gray contours. Buoyancy contours are plotted in the range of 1×10^{-3} m s$^{-2} \leq 0.6 \times 10^{-3} \leq 1.4 \times 10^{-3}$ m s^{-2}.

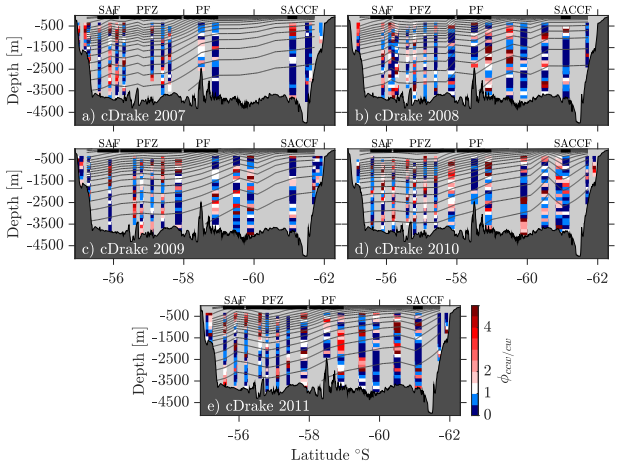

Figure 3.4: Across Drake Passage sections along the cDrake C-Line of polarization ratio $\phi_{ccw/cw}$ for a) November 13-December 7 2007, b) November 19-December 13 2008, c) November 19-December 19 2009, d) October 23-November 15 2010, and e) November 18-December 11 2011. $\phi_{ccw/cw} > 1$ (white to reds) indicates downward internal wave energy propagation in the Southern Hemisphere. Thick black bars along the top axis show the mean position of the ACC fronts (Fig. 3.1). The buoyancy contours averaged for the duration of each cDrake cruise are shown in gray contours. Buoyancy contours are plotted in the range of 1×10^{-3} m s^{-2} $\leq 0.6 \times 10^{-3} \leq 1.4 \times 10^{-3}$ m s^{-2}.

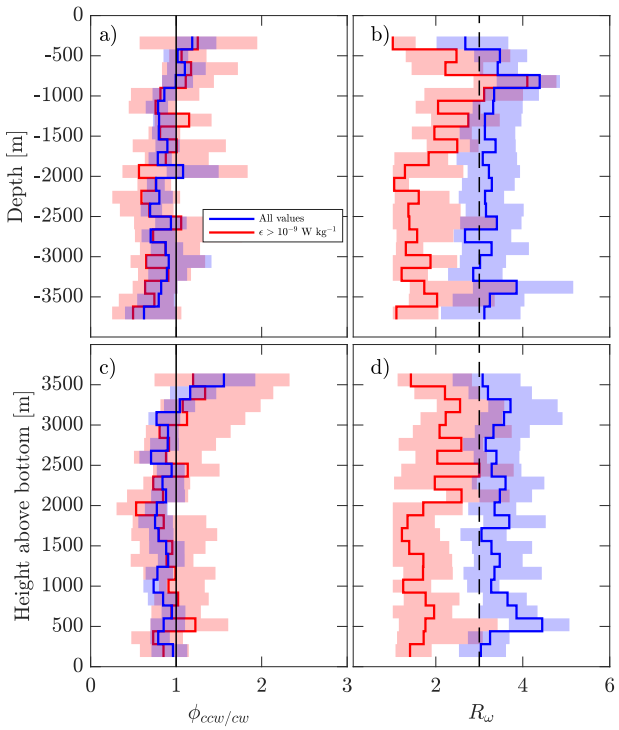

Figure 3.5: Median profiles of (a),(c) polarization ratio $\phi_{ccw/cw}$ and (b),(d) shear-to-strain ratio R_ω as a function of (a)-(b) depth and (c)-(d) height above the bottom. Blue and red thick solid lines are calculated using all data available and those where finescale dissipation rates $\varepsilon > 1 \times 10^{-9}$ W kg^{-1}, respectively. Blue and red shaded areas show the bootstrapped 95% confidence limits. $\phi_{ccw/cw} > 1$ (solid black line in (a),(c)) suggests downward internal wave energy propagation. Dashed line in (b),(d) indicates the canonical Garrett-Munk shear-to-strain ratio $R_\omega = 3$.

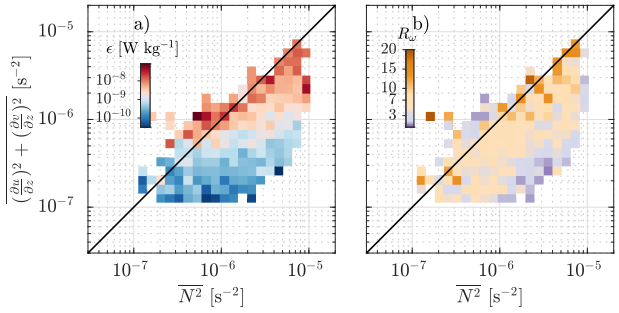

Figure 3.6: Bin averaged patterns of a) finescale dissipation rates ε [W kg^{-1}] and b) shear-to-strain ratio R_ω as a function of referenced mean stratification $\overline{N^2}$ [s^{-2}] and mean shear squared $\overline{(\frac{\partial u}{\partial z})^2 + (\frac{\partial v}{\partial z})^2}$ [s^{-2}]. The solid diagonal line shows the 1:1 relationship, i.e. the Richardson number Ri= 1. Empty bins (white) where the number of 320-m estimates of ε or R_ω is less than 5 are not averaged.

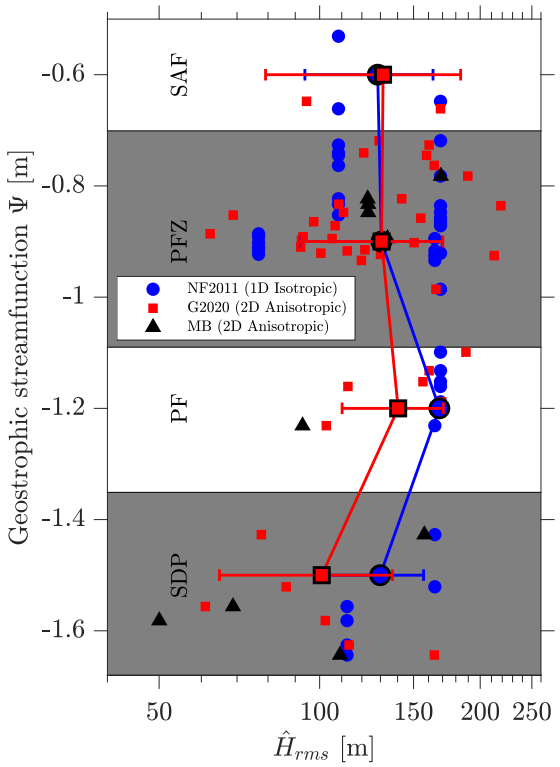

Figure 3.7: $\hat{H}_{rms}$ for Drake Passage area as a function of geostrophic streamfunction Ψ [m]. Filled circles, squares and triangles indicate the $\hat{H}_{rms}$ using the NF2011, G2020, and MB statistical parameters, respectively. Black-lined blue circles and red squares show the mean $\hat{H}_{rms}$ calculated from the NF2011 and G2020 parameters, respectively, for each frontal region. Horizontal bars are the standard deviation. SAF, PFZ, PF, and SDP are the Subantarctic Front, Polar Front Zone, Polar Front and Southern Drake Passage, respectively. Southern Drake Passage includes the Southern ACC Front.

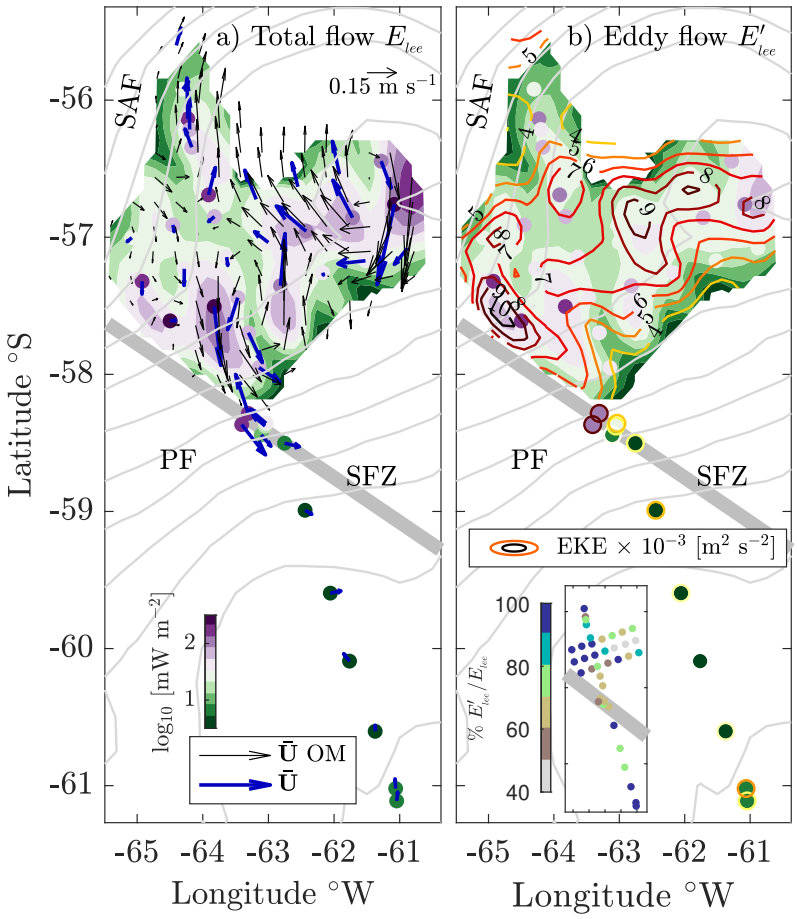

Figure 3.8: (a) Log_{10} of lee-wave energy radiation due to the total flow E_{lee} [mW m^{-2}], calculated using eq. (3.9). Filled circles correspond to mean estimates using the near-bottom CPIES time series of current velocity and stratification at 50 m above the bottom. Vectors show the objectively mapped low-pass currents at 4000 m (thin black; vectors are plotted every other grid point) and from the current meter (thick blue). (b) Log_{10} lee-wave energy radiation due to the eddy flow E'_{lee} [mW m^{-2}], calculated using eq. (3.10). Color-coded contours and open circles show the near-bottom eddy kinetic energy (EKE $\times$ 10^{-3} m^2 s^{-2}). Only the G2020 statistical parameters are used to estimate the lee-wave energy estimates shown in the figure. The same colorbar scale is used for both E_{lee} and E'_{lee}. The location of the Shackleton Fracture Zone is included (gray thick line). Light gray contours show the mean dynamic topography by Maximenko et al. [2009]. Small inset shows the % contribution from the energy radiation from the eddy flow to that of the total flow, both calculated from the CPIES data.

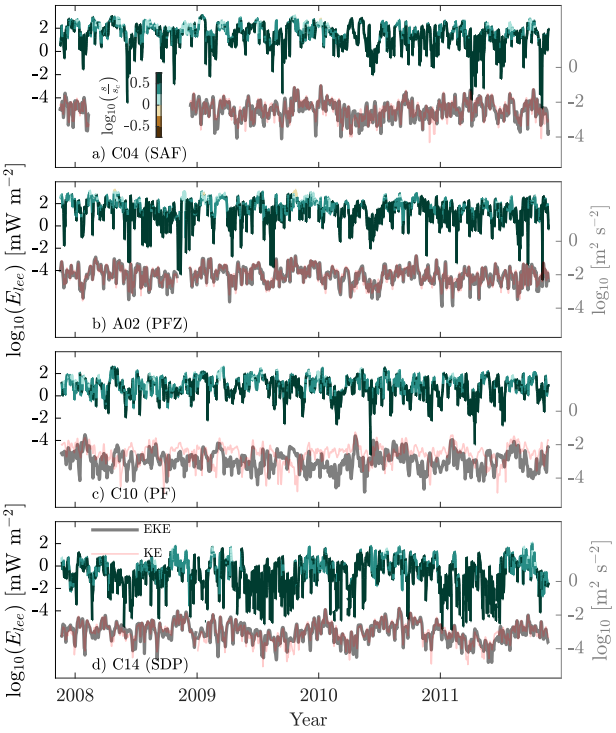

Figure 3.9: (a)-(d) Time series of $\log_{10}$ lee-wave energy radiation E_{lee} [mW m^{-2}] color-coded by the $\log_{10}$ (s/s_c), and $\log_{10}$ of near-bottom EKE (gray thick line) and KE (red line) [m^2 s^{-2}] estimated from near-bottom current meters and stratification at different CPIES locations (the location of each CPIES with respect to the frontal regions is included). Time series of E_{lee}, KE and EKE were smoothed using a three-day running mean. $\mathrm{Log}_{10}(s/s_c) < 0$ indicates subcritical topography. Only the G2020 statistical parameters are used to estimate s and E_{lee}.

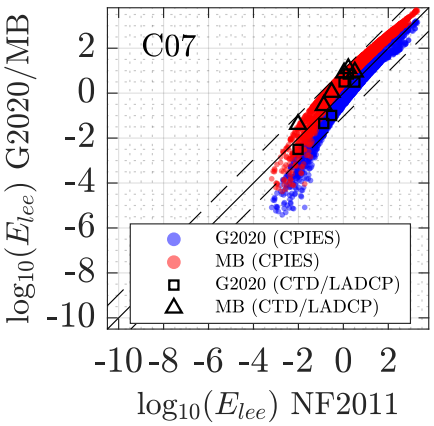

Figure 3.10: Log_{10} lee wave energy radiation (E_{lee}) [mW m^{-2}] calculated using the NF2011 1D isotropic abyssal topography vs $\log_{10}$ lee wave energy radiation calculated using a 2D anisotropic abyssal topography at CPIES C07 (Fig. 3.1). Filled circles are energy estimates using the CPIES bottom current meters and stratification time series. Blue and red circles indicate that E_{lee} (y axis) was calculated using the G2020 and MB statistical parameters, respectively. Open black squares and triangles are E_{lee} (y axis) calculated using the G2020 and MB statistical parameters, respectively, using the CTD/LADCP stratification and velocity averaged in the 1000 m closest to the bottom. Solid diagonal shows the 1:1 relationship. Dashed diagonals show the one order of magnitude limits.

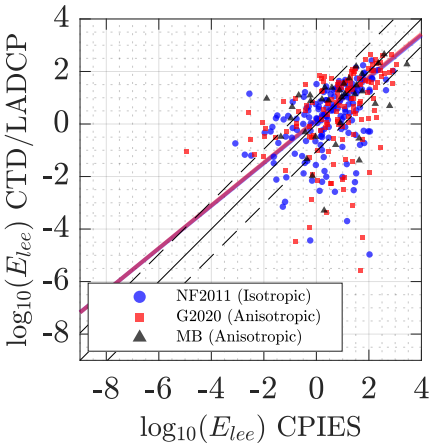

Figure 3.11: Log_{10} lee-wave energy radiation using the CTD/LADCP casts (E_{lee} CTD/LADCP) [mW m^{-2}] vs $\log_{10}$ lee-wave energy radiation using the CPIES near-bottom current meter and stratification (E_{lee} CPIES) [mW m^{-2}]. Lee-wave radiation is estimated using the NF2011 (filled blue circles), G2020 (filled red squares), and MB-inferred (filled black triangles) statistical parameters. Red and blue solid lines are the linear fit in $\log_{10}$ scale for the NF2011 and G2020 topographies, respectively. Only estimates falling within one order of magnitude are used for the linear fit, which amounts to 60% and 52% of total number of all estimates (177) for the NF2011 and G2020 topographies respectively. Solid diagonal shows the 1:1 relationship. Dashed diagonals show the one order of magnitude limits.

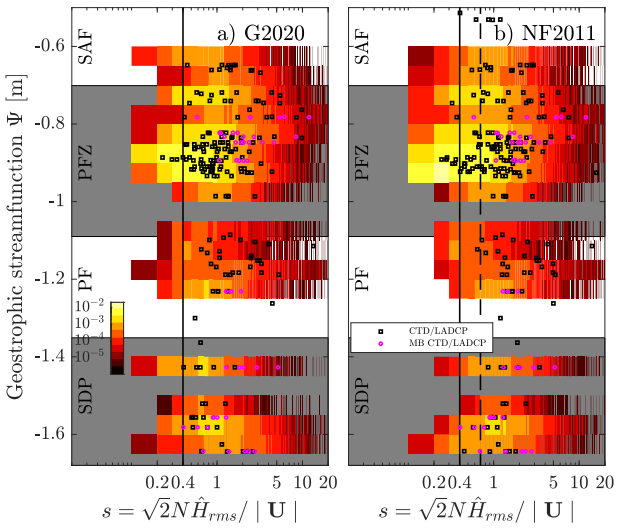

Figure 3.12: Two-dimensional probability distribution of steepness parameter s and geostrophic streamfunction Ψ [m] for the Drake Passage area. Colorbar shows the probability for s calculated using the CPIES near-bottom current meters and stratification and the (a) G2020 and (b) NF2011 $\hat{H}_{rms}$ values (see Fig. 3.7). Black open squares are the steepness values calculated for the CTD/LADCP using the (a) G2020 and (b) NF2011 topographies; magenta open circles (a),(b) use the MB bathymetry. Vertical solid line indicates the critical steepness parameter $s_c = 0.4$. Vertical dashed line in (b) shows $s_c = 0.7$ employed by Nikurashin and Ferrari [2011]. Bin size is 0.05 m and 0.10 for Ψ and s, respectively.

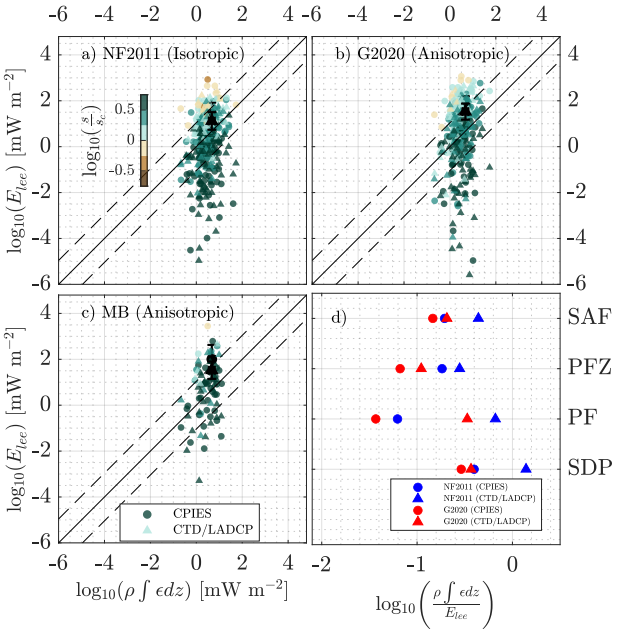

Figure 3.13: Lee-wave energy radiation (E_{lee}) [mW m^{-2}] vs finescale turbulent kinetic energy dissipation ε integrated from the bottom to the base of the mixed layer in Drake Passage [mW m^{-2}]. Lee-wave energy radiation is calculated using the (a) NF2011, (b) G2020, and (c) MB abyssal hill topography. Filled circles show the energy radiation estimated using the CPIES near-bottom current meter and stratification closest in time to the CTD/LADCP cast. Colorbar shows the $\log_{10}(\frac{s}{s_c})$. CTD/LADCP-based energy estimates are shown in colored filled triangles. Mean and bootstrapped 95% confidence limits for both CPIES and CTD/LADCP-based estimates are shown in black symbols (filled circles and triangles, respectively), and vertical and horizontal bars. Solid diagonal shows the 1:1 relationship. Dashed diagonals show the one order of magnitude limits. (d) Log_{10} of the averaged ratio between the vertically integrated dissipation and lee-wave energy radiation by frontal region. Blue and red symbols indicate that the NF2011 and G2020 abyssal hill topography was used. CTD/LADCP and CPIES estimates are shown in open circles and filled triangles. Only data found in (a)-(b) was used for estimating the ratio.

Chapter 4

Long-term temporal variability of Drake Passage properties and transport

4.1 Introduction

The eastward flowing Antarctic Circumpolar Current (ACC) is one of the critical components of the Southern Ocean (SO) and the global ocean climate system, as it connects the major ocean basins. The ACC promotes exchange between the three major ocean basins, allowing the establishment of a global-scale overturning circulation which transports heat, moisture, carbon dioxide, and other tracers around the globe and strongly influences the Earth's climate. Therefore, accurately quantifying the transport of the ACC and its three-dimensional structure is pivotal to assessing how the SO is responding to climate change.

Drake Passage has historically provided an ideal location for monitoring the ACC transport, as it represents the narrowest constriction (800 km) that the ACC navigates on its circumpolar path. As such, Drake Passage transport serves as a valuable metric for validating ocean and climate models and for constraining inverse models. Recent estimates of Drake Passage transport suggest that the canonical transport estimate of 134 Sv from the International Southern Ocean

Studies (ISOS) program [Cunningham et al., 2003; Whitworth and Peterson, 1985] might be low [Colin de Verdière and Ollitrault, 2016; Donohue et al., 2016; Firing et al., 2011; Griesel et al., 2012; Koenig et al., 2014; Mazloff et al., 2010]. Koenig et al. [2014] estimated a full-depth Drake Passage transport of 141 Sv from a combination of moored current meters (DRAKE, 2006-2009) and satellite altimetry. cDrake (2007-2011), which used an extensive array of Current and Pressure recording Inverted Echo Sounders (CPIES), estimated a full-depth baroclinic and barotropic transport of 127 Sv [Chidichimo et al., 2014] and 45.6 Sv [Donohue et al., 2016], respectively, yielding a total of 173 Sv. Colin de Verdière and Ollitrault [2016] estimated Drake Passage transport (175 Sv) by enforcing mass conservation applied to Argo float displacements and World Ocean Atlas hydrography and found agreement with the cDrake transport estimate. Nevertheless, as pointed by Xu et al. [2020], it is possible that the cDrake and DRAKE transports might be biased high and low, respectively: the cDrake total transport [Donohue et al., 2016] might be overestimated due to undersampling the tight near-bottom recirculation south of the Shackleton Fracture Zone [Xu et al., 2020] while the surface geostrophic currents used in the DRAKE estimate [Koenig et al., 2014] yielded a weaker near-surface transport than that estimated from shipboard Acoustic Doppler Current Profiler (sADCP) measurements [Firing et al., 2011]. By comparing high-resolution global model output to the cDrake, DRAKE, ISOS, and sADCP data, Xu et al. [2020] concluded that the model's 157.3 Sv mean transport is representative of the time-mean ACC transport through Drake Passage; the model's transport is approximately the average of the cDrake [Donohue et al., 2016] and DRAKE [Koenig et al., 2014] estimates. Although uncertainty still persists for the time-mean Drake Passage transport, these new observational studies have led to a better description of the mean vertical and horizontal structure of the ACC.

How the ACC transport responds to atmospheric forcing remains an open question. An increase in the SO westerly winds has been documented over the past several decades, reflecting

an intensification of the Southern Annular Mode [SAM; Fogt and Marshall, 2020; Marshall, 2003]. Coarse-resolution global climate models (GCMs) have predicted that the increase in the strength of the westerlies over the ACC leads to an increase in the model transport [Farneti et al., 2010; Hall and Visbeck, 2002; Meredith and Hogg, 2006]. In contrast, eddy-permitting GCMs have shown that the ACC transport remains invariant to the increase in the wind forcing whilst the mesoscale eddy activity increases, reaching a saturation eddy state [Hallberg and Gnanadesikan, 2001; Meredith and Hogg, 2006; Patara et al., 2016]. None of the ISOS, DRAKE, and cDrake [Chidichimo et al., 2014] estimates show a clear trend in the Drake Passage transport. Böning et al. [2008] showed that the southward shift and strengthening of the westerly winds (attributable to anthropogenic warming) in recent decades apparently do not accelerate the ACC flow. Using a $1/12^{\circ}$ high-resolution model, Xu et al. [2020] showed that the modeled transport through Drake Passage exhibits no long-term trend as the modeled baroclinic and barotropic transports tend to compensate each other. Also, the authors suggested that monitoring the barotropic or baroclinic components alone is insufficient to assess the temporal variability of the total transport. Long-term high spatial resolution measurement programs that monitor both the barotropic and baroclinic flow components in addition to the total flow are required to resolve the highly variable currents across Drake Passage and to observe possible long-term trends of the ACC baroclinic and barotropic transports with statistical significance. The lack of long-term in-situ observations hampers the exploration of other long timescales of variability and long-term trends in the ACC total, baroclinic and barotropic transports.

The SO has been experiencing rapid changes in its water mass properties for the last five decades due to an increase of heat uptake driven by the greenhouse effect [Auger et al., 2021; Gille, 2002, 2008; Swart et al., 2018]. Early eddy-resolving numerical simulations indicated that an increase in the surface buoyancy forcing can change the upper-ocean stratification and alter the latitudinal density gradients [Hogg, 2010]. Using an array of Argo floats and hydrographic surveys, Böning et al. [2008] found a significant ocean warming in the upper 1500 m in the north

flank of the ACC over the last 20 years. More recently, Shi et al. [2021] found from observations that the significant warming of the upper ocean concentrated north of the Subantarctic Front drives a small but significant acceleration ($O(0.1-1)$ cm s^{-1} per decade) of the zonally-averaged eastward flow in this region. However, Shi et al. [2021] did not find an acceleration of the flow in Drake Passage. The authors attribute the acceleration to heat uptake in the surface on the north flank of the ACC due to an increase in human-induced greenhouse gas over the last several decades [Swart et al., 2018]. Whether this warming pattern extends to the Drake Passage latitudes and consequently accelerates the zonal flow in Drake Passage, remains unclear and warrants exploration from an observational standpoint.

In contrast to the ocean warming that the subtropical regions of the SO have experienced over the last three decades, the high-latitude subpolar regions (the SO at Drake Passage latitudes 54°S-70°S) have cooled at the surface [Auger et al., 2021]. The surface cooling is evident in the Pacific sector of the SO, but it is maximum in the Drake Passage area [Auger et al., 2021; Sprintall, 2008]. How this surface cooling can influence the density gradients across Drake Passage and, therefore, the ACC transport through Drake Passage, remains unclear. Here we hypothesize that the increase in the westerly wind stress over the ACC increases the upwelling of cold water along the isopycnals south of the Polar Front. This cold water is advected equatorward by the Ekman transport which can increase the temperature and density gradients across the fronts in the upper ocean, thereby driving an acceleration of the eastward ACC flow and transport through Drake Passage. While this hypothesis only accounts for temperature-driven changes, cooling can induce salinity changes in the upper ocean. These salinity changes can modify the density gradients with time, especially south of the Polar Front where salinity's role in setting the stratification in this region is important. Long-term monitoring of the temperature and salinity across the Drake Passage could help to determine temporal trends in both the temperature and salinity in the baroclinic structure of the ACC.

This chapter uses a unique observational time series of year-round repeated temperature,

salinity, and underway velocity across the ACC to explore whether the Drake Passage flow shows significant warming and acceleration in the last two decades. The multi-decadal Drake Passage time series is one of the most frequently repeated and longest continuous time series of temperature, salinity, and underway velocity across the ACC in the SO. The unprecedented high along-track spatial resolution of the transects allows us to observe patterns on the order of the first baroclinic Rossby radius, which spans from 20 km in the northern Drake Passage to 10 km near the Antarctic Peninsula [Chelton et al., 1998]. Moreover, the 25-year temperature time series allows for exploring and documenting both interannual and long-term variability of the upper ocean in Drake Passage.

4.2 Data sets

4.2.1 Underway velocity

Underway upper-ocean velocity, temperature, and salinity were collected aboard the Antarctic Research and Supply Vessel (ARSV) Laurence M. Gould (LMG) that transits between South America and the Antarctic Peninsula (Fig. 4.1). Since September 1999, a narrowband 150 kHz Acoustic Doppler Current Profiler (ADCP; NB150) has sampled velocity in the upper 300 meters at 8-m vertical resolution with the first depth bin at 26 m. In addition, since November 2004, a 38 kHz phased array ADCP (OS38) has sampled velocity in the upper 1000 m at 24-m vertical resolution with the first depth bin at 46 m. Here we use only the upper 210 m and 970 m for the NB150 and OS38 ADCPs, respectively, since the velocity profiles are gappier below these threshold depths. Transects were discarded if they did not cross the 1000-m isobath at either the South American and Antarctic continental shelves or if the ship significantly deviated from its main course. From September 1999 - December 2019, 354 NB150 and 248 OS38 (of 400 and 300 total crossings respectively) ADCP transects meet these criteria. 172 and 147 transects fall into the most commonly repeated line (blue thick line, Fig. 4.1a) for the NB150 and OS38

respectively.

Velocity data were processed using the Common Ocean Data Access System (CODAS) software [Firing et al., 2012]. Following Lenn et al. [2007] and Firing et al. [2011], returned ping data are averaged over 5-min ensembles and screened using amplitude, error velocity, and percent good criteria. Velocities were transformed from ship-relative to absolute ocean currents using GPS position and attitude measurements. The absolute current velocities are in 5-min resolution, i.e. ~ 1.60 km along-track resolution (assuming a ship's speed of 5.5 m s^{-1}). Barotropic tidal currents were removed from the absolute velocity by subtracting the tidal prediction of the TPXO7.2 tide model [Egbert et al., 1994]. Baroclinic tides and ageostrophic Ekman currents $O(0.01)$ m s^{-1} were not removed from the velocity data as it is impractical to remove these flows within uncertainty for each transect. In the upper 24 m and 42 m where the NB150 and OS38 ADCPs did not sample, a slab layer was assumed.

Here errors in the ADCP are examined to assess the significance of the velocity trends. Following Rocha et al. [2016], the OS38 ADCP accuracy is 1.75×10^{-2} m s^{-1} for 5 min averages (i.e., 100 pings), and an error in ship's speed due to GPS position error of 2.4×10^{-2} m s^{-1}, resulting in a absolute velocity error of 2.97×10^{-2} m s^{-1} or 2.97 cm s^{-1}. Velocity profiles are block-averaged into 25-km along-track bins (~ 83 min for a mean ship velocity of 5 m s^{-1}) per transect. The block averaging reduces the error by a factor of 0.25 to yield an absolute velocity error of 0.74×10^{-2} m s^{1} or 0.74 cm s^{-1}. The absolute velocity error rises to 1.05×10^{-2} m s^{-1} if data is averaged instead to 12 km along-track resolution. The 25-km averaged absolute error translates to a standard error of 0.04 cm s^{-1} in the mean for 248 transects. Therefore, the absolute error resolves trends of 2.6×10^{-3} cm s^{-1} year^{-1} in 15 years of data, or 2.5×10^{-3} Sv year^{-1} for an area of 100 km $\times$ 970 m, where 100 km is the typical width of the ACC fronts in Drake Passage. Additional error could arise from errors in determining the transducer alignment as found by Firing et al. [2011] and discussed in the next section yields a bias of 7.2×10^{-3} m s^{-1} or 7.2×10^{-1} cm s^{-1}. Clearly, this error is smaller than the absolute velocity error, therefore,

resulting in a smaller error in the trend. For the NB150, the absolute velocity error is 0.61 cm s^{-1} for 25-km averages, yielding an error in the velocity trends as large as 1.6×10^{-3} cm s^{-1} $year^{-1}$ for 20 years of data.

4.2.2 XBT temperature and XCTD salinity

Since September 1996, on 6-7 LMG transects per year, 70 eXpendable Bathythermograph (XBT) probes are deployed that measure temperature in the upper 900 m. The temperature profiles were averaged to 10-m depth bins. The spatial resolution is 6-10 km across the Subantarctic Front and Polar Front, and 10-15 km elsewhere [Sprintall, 2003]. All data were quality-controlled and corrected as in Sprintall [2003]. A lookup temperature-salinity-depth-position relation was constructed from historical hydrography. The lookup relation was employed to estimate salinity for each XBT temperature profile. The majority of crossings also deployed twelve expendable conductivity-temperature-depth (XCTD) probes with a spacing of 25 to 50 km to directly measure temperature and salinity in the upper 1000 m. These XCTD data were used to correct the historical data. The salinity anomaly was determined from the XCTD measurements with respect to the historical data, and then the salinity anomaly was objectively mapped along the transect and added to the XBT-derived salinities. Overall, there are 114 XBT/XCTD transects from September 1996 - December 2019 that were used to calculate the time-mean temperature and salinity fields; 53 of these transects fall along the most commonly sampled line (Fig. 4.1a). 63 of 114 surveys coincide with the OS38 ADCP transects from November 2004 to December 2019, and 98 with the NB150 from September 1999 to December 2019.

Akin to the errors in the velocity trends, we investigated the errors in the XBT temperature and XCTD salinity probes to assess the significance of their trends. The error associated with the systematic fall rate error is $\sim 1\%$ of the depth due to random probe differences. The thermistor calibration error is 0.05°C, which translates into a standard error of 0.005° for 114 transects. For a sampling period of 23 years, the standard error resolves trends of 2.5×10^{-4} °C $year^{-1}$; the

error reduces to 3.1×10^{-4} °C year^{-1} for a 15-year sampling period. The XCTD probes accuracy of ~ 0.05 psu accounts for the errors in conductivity, temperature and pressure [Gille et al., 2009]. This accuracy translates into a standard error of 4.7×10^{-3} psu from the mean, and it allows to estimate trends of 1.8×10^{-4} psu year^{-1} in 23 years of data.

Each temperature and salinity transect was objectively mapped to a latitude-depth grid with a horizontal and vertical resolution of 1/10° (i.e. $\sim$11 km along-track resolution) and 10 m starting from the surface to 760 m, respectively. The 760 m depth range is employed as the XCTD data samples to this depth only. For the horizontal grid, two Gaussian functions were used: one with a large-scale decorrelation scale of 100 km and another with a mesoscale decorrelation that is the first baroclinic Rossby radius that varies with latitude [Chelton et al., 1998].

4.2.3 Sea surface altimetry

SSALTO/DUACS daily maps of sea level anomalies are employed for estimating the mesoscale geostrophic velocities. The daily maps were obtained from multiple satellite altimeters and objectively mapped to a $0.25° \times 0.25°$ Cartesian grid [Ducet et al., 2000]. The sea level anomalies are relative to a twenty-year mean of the sea surface height field. We use the daily maps from September 1999 to December 2019, which covers our period of interest.

The ACC frontal locations are determined using daily maps of sea level anomalies plus the Mean Dynamic Topography from Maximenko et al. [2009] derived from a combination of 20 years of satellite altimetry, gravity measurements, and in situ data. We use each front's streamfunction values as defined by Gutierrez-Villanueva et al. [2020] to determine the velocity, temperature, and salinity profile positions relative to the fronts in Drake Passage.

4.2.4 ECMWF reanalysis version 5

To estimate trends in the wind stress curl over the SO and Drake Passage area, zonal and meridional wind components at 10 m above the sea level from the fifth-generation reanalysis product [ERA5, Hersbach et al., 2020] of the European Center for Medium-Range Weather Forecast (ECMWF) are employed. ERA5 is produced using 4D-Var data assimilation (from historical observations) and model forecasts with 137 hybrid-sigma/pressure levels in the vertical and the top level at 0.01 hPa (1 m). The horizontal spatial resolution is $0.25^\circ \times 0.25^\circ$. We use the period from 1996-2019, which corresponds to the sampling period of the Drake Passage observations. This study uses monthly means created from the hourly data.

4.3 Methods

4.3.1 Constructing time series of total velocity

The velocity vector was rotated to an along/across-transect coordinate system. For this study, only the across-transect component u_{tot} was kept such that positive flow means eastward flow, and then bin-averaged u_{tot} onto a 25-km along-track grid [Firing et al., 2011]. For transects with continuous gaps $\leq$ 150 km, gaps were filled using an objective mapping as follows. The 25-km across-transect velocity anomalies were estimated by subtracting the mean geostrophic across-transect velocity component obtained by calculating objectively mapped mean geostrophic velocity vectors as in Gutierrez-Villanueva et al. [2020] and references therein. In calculating the mean geostrophic velocity, all available transects from the OS38 and NB150 ADCPs were employed. For each transect, the nearest mean geostrophic velocity (in a 25 km $\times$ 25 km grid-box) to the u_{tot} velocity position was employed and rotated to the along/across-transect coordinates to estimate the mean geostrophic across-transect velocity component. Next, the velocity anomalies were objectively mapped into an along-track/depth grid using a Gaussian covariance function

with horizontal and vertical decorrelation scales of 50 km and 300/100 m, respectively, for the OS38/NB150.

4.3.2 Correcting OS38 misalignment angle

As in Firing et al. [2011], the time series of the total transport calculated from the OS38 velocity shows a systematic offset between northbound and southbound OS38 estimates of the total transport integrated across Drake Passage, $U_{tot} = \int_0^L \int_{-970}^0 u_{tot} dz dx$ (L is the length of the transect). The mean southbound transport was 23 Sv less than that estimated from the northbound cruises. This bias arises from a bias in the cross-track velocity and is consistent with a rotation calibration error, termed transducer misalignment error, that results in a component of the ship's speed erroneously projected in the cross-track direction. Since the ship speed changes sign when the direction of steaming is reversed, so does the sign of the velocity error. Normally, transducer misalignment (fine-tuning of the orientation of the transducer in the ship's hull) is determined through bottom tracking calibration in shallow water, where the ship speed over the ground from the ADCP is calibrated against ship speed from GPS. Both ADCPs are routinely calibrated with bottom track data when available. The NB150 time series do not exhibit any systematic error upon estimating mean transports for the northbound and southbound transects. For the OS38, the cross-transect velocities were corrected to account for the residual ADCP transducer misalignment angle error following Firing et al. [2011], by minimizing transport bias. In summary, the method assumes that both the mean northbound and southbound transport should be equal. First, a least-squares model was fitted to the northbound and southbound transport time series:

$$\hat{y} = a_0 + a_1 t + a_2 \cos(\omega_{ann} t) + a_3 \sin(\omega_{ann} t) + a_4 \cos(\omega_{semi} t) + a_5 \sin(\omega_{semi} t), \qquad (4.1)$$

where $\hat{y}$ is the predicted variable (transport), $a_0, ..., a_5$ are the model coefficients corresponding to the mean, trend, annual and semiannual transports, and ω_{an} and ω_{semi} are the annual and semiannual frequencies. U_{tot} estimates are discarded from the least-squares fit if the transport exceeds 3σ, where σ is the standard deviation of the northbound and southbound transects, separately. For the southbound (127) and northbound (117) transects, a_0 was estimated as 75.73 ± 7.06 Sv and 102.56 ± 5.94 Sv, respectively, hence resulting in a bias of 13.41 Sv. The bias then was added to or subtracted from the individual southbound and northbound estimates. Using the least-squares model (eq. 4.1), the corrected U_{tot} time series yields a mean transport $\overline{U}_{tot} = 89.41 \pm 4.69$ Sv. This value is in close agreement with Firing et al. [2011]'s mean of 90 ± 2.1 Sv based on the first 5 years of data.

To correct u_{tot} transects due to the misalignment angle, the velocity offset u_{offs} was estimated as:

$$u_{offs} = \frac{U_{tot} - \overline{U}_{tot}}{A}, \tag{4.2}$$

where A is the area that corresponds to the along-track distance (that varies for each transect) multiplied by the depth of the deepest ADCP bin (970 m). The average u_{offs} for the southbound and northbound transects is 1.4 cm s^{-1} and -1.2 cm s^{-1}, respectively. These values are in agreement with those estimated by Firing et al. [2011]. The mean transport using u_{tot} corrected with the velocity offset u_{offs} was calculated, and the transport is almost equal (or at least statistically not different) to that using the transport correction method. The size of the misalignment angle α_{miss} correction to the cross-transect velocity component is approximately:

$$\alpha_{miss} = \arcsin\left(\frac{u_{offs}}{|u_{ship}|}\right), \tag{4.3}$$

where $u_{ship} = 5.5$ m s^{-1} is the typical ship's velocity. Excluding a few outliers (5 of 204 transects), the mean of the α_{miss} time series is 0.14° with a standard error of 0.03°.

4.3.3 Filling gaps in the NB150 cross-transect velocity

Starting in November 2004 (i.e., the start of the OS38 sampling period), a large percentage of NB150 transects are gappier than those before November 2004. Many gaps were too large to be filled using objective mapping. Gaps in the NB150 are the largest in the southern Drake Passage, owing to lower backscatter resulting in reduced velocity measurements relative to the northern Drake Passage. Since OS38 velocity data is less gappy than NB150 data, the concurrent OS38 transects were used to fill the gaps in the NB150. The 25-km velocity anomalies from the OS38 ADCP were objectively mapped to the same vertical resolution of the NB150, using the same Gaussian covariance functions employed for the NB150.

4.3.4 Geostrophic and reference transport

The upper-ocean geostrophic across-stream velocity component u_{geo} and volume transport U_{geo} integrated across Drake Passage were estimated from the temperature and salinity transects. The transects were employed to estimate the geopotential anomaly Φ, which is the geostrophic streamfunction given as:

$$\Phi = \int_{p_0}^{p} \delta(x,p)dp, \tag{4.4}$$

where $p_0 = 760$ db is the reference pressure, p is pressure, and δ is the specific volume anomaly estimated from the temperature and salinity transects. Across-transect geostrophic velocity u_{geo} was then calculated as the first difference of Φ with respect to the along-track distance:

$$u_{geo} = -\frac{1}{f}\frac{\partial \Phi}{\partial x}, \tag{4.5}$$

where f is the local Coriolis frequency, and x is the along-track distance. Geostrophic transport across Drake Passage U_{geo} was then calculated as the integral of u_{geo}, i.e. $U_{geo} = \int_0^L \int_{z_0}^0 u_{geo} dz dx$, where L is the length of the transect, and $z_0 = -760$ m is the deepest bin.

The total across-transect velocity u_{tot}, defined in Section 3.2 as that of the ADCP velocities, is given by the geostrophic u_{geo} and reference u_{ref} components (i.e. $u_{tot} = u_{geo} + u_{ref}$). The reference component is defined as the averaged residual velocity over the sampled water column

$$u_{ref} = \frac{1}{|z_1 - z_2|} \int_{z_2}^{z_1} (u_{tot} - u_{geo}) dz, \tag{4.6}$$

where $z_2 = 210$ m (NB150) and 760 m (OS38) are the deepest bin for each ADCP and $z_1 = 90$ m is the base of the Ekman layer. The Ekman layer was defined where the total shear $\frac{\partial u}{\partial z}_{tot}$ showed an exponentially decaying profile, after first averaging per transect and then averaging for the entire time series (Fig. 4.2) [Lenn and Chereskin, 2009]. Below 90 m, the mean shear velocity reduces to a constant value and is in good agreement with the geostrophic shear $\frac{\partial u}{\partial z}_{geo}$ (Fig. 4.2). Reference transport integrated across Drake Passage was calculated as $U_{ref} = \int_0^L \int_{760}^0 u_{ref} dz dx$.

The U_{ref} time series for the common period of October 2005-April 2019 are shown in Fig. 4.3. While the time series seem correlated, the NB150 U_{ref} series (dark cyan, Fig. 4.3a) shows no linear trend whereas the OS38 time series (gray, Fig. 4.3a) apparently exhibits a decaying trend starting in October 2005. The mean reference transport $\overline{U}_{ref}$ is larger for the NB150 than for the OS38 reference transport (Fig. 4.3b). We tested if using the same depth range as that of the NB150 (90-210 m) for estimating the OS38 u_{ref}, therefore, U_{ref} (Fig. 4.3a; salmon) could explain the difference in the trends. Using a similar depth range to that of the NB150 still shows a negative trend although the time series variance is larger than that for the OS38 from 90-760 m. Both OS38 time series show a distribution skewed towards relatively small transport estimates (< 50 Sv) compared to the NB150 transport distribution (Fig. 4.3c). Having these caveats in mind, we use the NB150 and OS38 (90-760 m) time series of reference velocity and transport for the rest of the analysis.

4.3.5 Isopycnal heaving and spiciness

To understand the changes in potential temperature θ and salinity S with depth and position across Drake Passage, temperature and salinity trends were decomposed into two main contributions [Bindoff and McDougall, 1994]: modification of temperature and salinity along isopycnals (neutral density layers γ) called "spiciness", and vertical displacement "heave" of neutral density layers [Jackett and McDougall, 1997]. As discussed by Durack and Wijffels [2010], the analysis when done along pressure-density surfaces allows a direct calculation of the component of temperature and salinity change due to vertical heave of neutral density surfaces, and that due to spice. The decomposition of the total potential temperature and salinity changes $\frac{\partial \theta}{\partial t}_p$ and $\frac{\partial S}{\partial t}_p$ on a pressure surface is:

$$\frac{\partial \theta}{\partial t}_p = \frac{\partial \theta}{\partial t}_\gamma + \frac{\partial \overline{\theta}}{\partial \overline{\gamma}} \frac{\partial \gamma}{\partial t}_p + \text{Res}, \tag{4.7}$$

$$\frac{\partial S}{\partial t}_p = \frac{\partial S}{\partial t}_\gamma + \frac{\partial \overline{S}}{\partial \overline{\gamma}} \frac{\partial \gamma}{\partial t}_p + \text{Res}. \tag{4.8}$$

The first terms on the right-hand side of eq. 4.7 and 4.8 represent the changes on neutral density levels, whereas $\frac{\partial \overline{\theta}}{\partial \overline{\gamma}}$ and $\frac{\partial \overline{S}}{\partial \overline{\gamma}}$ are the local gradient of mean θ and S in γ, and $\frac{\partial \gamma}{\partial t}_p$ represents the neutral density change on a pressure surface, Res represents other terms from the Taylor expansion that are considered as a residual. An important point is that the spiciness changes represent a shift in the θ/S profiles at a constant γ. Consequently, a change in salinity involves a change in temperature and conversely, temperature change along γ involves a change in salinity. Conversely, the heave component reflects adiabatic processes such as wind-driven Ekman pumping and low-frequency Rossby waves.

4.3.6 Statistical analysis: trends and significance

Trends in the transport (per 25-km distance over the grid spacing), total Drake Passage transports (U_{tot}, U_{geo}, and U_{ref}), cross-transect velocities (u_{tot}, u_{geo}, and u_{ref}) and salinity S and potential temperature θ were calculated using two different methods. For the two methods the seasonal cycle, which is the sum of the annual and semiannual harmonics estimated using eq. 4.1 from the fitted time series, was removed prior to estimating trends. For the first method, the trends were estimated by least-squares fitting $\hat{y} = a_0 + a_1 t$ to each time series; the second term on the right-hand side of the equation is the trend. Uncertainty in the calculated least-square trends is reported as the 95% confidence intervals [Fay et al., 2014] using

$$CI_{a_1} = \pm \mathrm{t}_{\alpha/2} \times RMSE \times \sqrt{\frac{1}{\sum (t_i - \bar{t})^2}}, \tag{4.9}$$

$$RMSE = \sqrt{\frac{\sum (\hat{y} - \mathrm{y}_i)^2}{N - \mu}}, \tag{4.10}$$

where $\mathrm{t}_{\alpha/2}$ is the Student's t statistic for 95% confidence (i.e., $\alpha = 0.05$), RMSE is the root mean square error, $\hat{y}$ is the predicted variable, y_i is the observed variable, $N - \mu$ is the number of observations minus the number of parameters fitted $\mu = 2$, and $\bar{t}$ is the average time in years.

For the second approach, trends were estimated using a Theil-Sen estimator [Sen, 1968; Theil, 1992], while the statistical significance used a modified Mann-Kendall test [Hamed and Rao, 1998]. The Mann-Kendall test is a commonly used non-parametric trend test. The modified test takes into account autocorrelations within the time series. The variance of a variable S for autocorrelated data can be calculated as

$$V^*(S) = \sigma_S^2 \cdot \frac{n}{n_S^*} = \frac{n(n-1)(2n+5)}{18} \cdot \frac{n}{n_S^*}, \tag{4.11}$$

$$n/n_S^* = 1 + \frac{2}{n(n-1)(n-2)} \times \sum_{i=1}^{n-1} (n-i)(n-i-1)(n-i-2)C_S(i), \tag{4.12}$$

where n is the actual number of "observations" and represents a correction related to autocorrelation in the time series and $C_S(i)$ denotes the autocorrelation between the ranks of observations. This study assumes that trends were statistically significant when the modified Mann-Kendall test resulted in a probability $p < 0.05$. In this study, all statistically significant trends in velocity and transport were above the absolute velocity error, and above the error due to the transducer misalignment for the OS38 time series (see sections 2.1 and 3.2). Similarly, significant salinity and potential temperature trends are above the XBT and XCTD probes' accuracy (see section 2.2).

Trends were also estimated by a least-squares fit using yearly means weighted by $1/\sigma$, where σ is the standard deviation of each calendar year. The standard deviation represents interannual plus mesoscale variability in the time series. The yearly means were also employed to estimate the trends and significance using the Theil-Sen estimator and the modified Mann-Kendall test, respectively. Trends estimated from the yearly averages were almost equal in spatial distribution and magnitude, and significance when compared to those trends estimated from the original time series. Therefore, we concluded that the trends presented in this study are long-term variability that stands out from relatively high-frequency (< 1 cycles per year) variability. Consequently, trends presented hereinafter were estimated by using the original time series (i.e., all transects).

4.4 Trends in Drake Passage transport

In this section, we examine the temporal variability of the total, baroclinic, and reference transports integrated across Drake Passage (U_{tot}, U_{geo}, and U_{ref} respectively; Fig. 4.4). Hereinafter, we interpret acceleration and deceleration of the eastward flow and transport as positive and negative trends, respectively. None of the time series of transport show a statistically significant trend, with the exception of U_{tot} in the upper 210 m for the NB150 time series (blue, Fig. 4.4b), which shows a statistically significant acceleration. However, the trend in the NB150 transport is sensitive to the vertical resolution: the trend becomes negative, but statistically insignificant when the total transport integrated across Drake Passage is calculated with the NB150 decimated to the OS38 vertical resolution ($dz = 24$ m; not shown). The geostrophic and reference transport time series show periods where they are 180° out of phase (black and dark cyan, Fig. 4.4c). Xu et al. [2020] suggested that compensation occurred between their modeled baroclinic and barotropic Drake Passage transports. Although the geostrophic transport in our study is referenced to the upper 760 m whereas the Xu et al. [2020] transports are referenced to the bottom, our results imply that periods of compensation between the geostrophic and reference components are likely to occur.

We tested if trends of the Drake Passage transport are sensitive to the sampling period and/or to the number of transects used. In calculating the trends for the Drake Passage total, geostrophic, and reference transports, we employed the ADCP sampling periods (November 1999 - April 2019 and October 2005 - April 2019), which correspond to the coincident NB150-XBT/XCTD and OS38-XBT/XCTD sampling periods using all transects as well as restricting the ADCP transects to those that have a coincident XBT/XCTD transect (squares and triangles, Fig. 4.5), respectively. Regardless of the period used, trends in the total transport are statistically insignificant in the upper 760 m (Fig. 4.5a) or 210 m (Fig. 4.5b), with the exception of the total transport trend in the upper 210 m (blue filled square, Fig. 4.5b). Nonetheless, the trend is

insignificant when the NB150 vertical resolution is decreased (not shown) as discussed earlier. Therefore, the Drake Passage total transport shows no significant trend in the last two decades [Shi et al., 2020, 2021; Xu et al., 2020]. Using those transects that have coincident XBT/XCTD transects does not alter the conclusion. The geostrophic transport trend is also statistically insignificant (Fig. 4.5c), which agrees with Cunningham et al. [2003] who found no trend in the Drake Passage baroclinic (geostrophic referenced to 3000 m) transport from assembling hydrographic sections at the western (from 1975 to 2000) and eastern ends of Drake Passage (SR1b section from 1993 to 200). Reference transport trend is only negative and significant when u_{ref} for the OS38 time series are employed (salmon and gray filled squares, Fig. 4.5d), although even then, when using a shorter sampling period the trends become statistically insignificant (salmon and gray triangles, Fig. 4.5d).

Although we did not find a significant trend in the Drake Passage transport, we explore the possibility that there are opposing regional trends that are located in different dynamical (frontal) regimes of the ACC. These regions could compensate each other such that when trends are integrated across the entire Drake Passage, then zero or statistically insignificant trends are found for the total Drake Passage transport. This hypothesis is explored in the next section.

4.5 Trends in cross-transect velocity and transport

4.5.1 Velocity

We examine trends in the cross-transect velocities u_{tot}, u_{geo}, and u_{ref} as functions of distance and depth. Although our previous analysis found no significant trends in Drake Passage total transport, analyzing the velocity trends across Drake Passage allows us to identify spatial patterns in the trends. To make the comparisons among different data sets, we used similar sampling periods as in the previous section for the total transports.

Opposite trends in the cross-transect velocity are found across Drake Passage for the

different periods (Fig. 4.6). Nonetheless, all trends are of the same sign with depth (Fig. 4.6). Total velocity is significantly accelerating between 200-400 km, which corresponds to the warm flank (i.e., north) of the Polar Front (gray thick line in Fig. 4.6a-d,f), and in the southernmost area of Drake Passage, where the Southern ACC Front is located (magenta thick line in Fig. 4.6a-d). Trends in these regions reach to 1.2 cm s^{-1} $year^{-1}$ and 0.60 cm s^{-1} $year^{-1}$, respectively. Deceleration (negative trend) is found north of the Subantarctic Front (gold thick line in Fig. 4.6), near the South American shelf break (Fig. 4.6a) and south of the Polar Front spanning 400 km south (Fig. 4.6a,c), ranging between $0.6 - 1.2$ cm s^{-1} $year^{-1}$. The NB150-based trends in the upper 210 m show similar spatial patterns (Fig. 4.6b,d,f), but the negative trends south of the Polar Front are statistically insignificant when all transects are employed (Fig. 4.6b,d,f). Negative trends also are found in the core of the Polar Front (300 km) when using only those transects that have a coincident XBT/XCTD transect (Fig. 4.6c), likely owing to the changing position of the front due to meandering and eddy formation [e.g. Foppert et al., 2016; Gutierrez-Villanueva et al., 2020; Watts et al., 2016]. Geostrophic velocity trends show similar patterns although they are a factor of 2-3 smaller than those for the total velocity (Fig. 4.6e). Shi et al. [2021] using the gridded Argo global data set and gridded altimetry-based geostrophic velocities found no significant trends in Drake Passage area. Their trends are insignificant potentially due to the coarse horizontal resolution ($1^\circ \times 1^\circ$) that the gridded Argo temperature and salinity fields have due to the sparsity of Argo profiles, which impacts the objective mapping procedure [see Roemmich and Gilson, 2009], hence resulting in highly smoothed gradients in density, therefore, in geostrophic velocity. The gridded data does not have sufficient high spatial resolution as in the shipboard ADCP and XBT/XCTD data to distinguish between the different frontal regions across Drake Passage.

4.5.2 Transport per along-track distance

The time series of transport per distance $\delta y \int udz$, where δy is the along-track resolution, are shown in Fig. 4.7a-c. For the total, geostrophic, and reference transports, maximum values are located near the South American shelf break (70-200 km) where the narrow Subantarctic Front sits. A wider secondary maximum is located in the Polar Front (350-500 km) and a third is close to the Antarctica shelf break (750-850 km) corresponding to the Southern ACC Front. The area between the Subantarctic Front and the Polar Front (200-350 km from the north), the area with the largest mesoscale activity in Drake Passage [Lenn et al., 2011], shows negative transport values potentially linked to a strong cyclonic circulation [Firing et al., 2016] that are the largest between 2005-2008, and become less evident and change sign (positive transport) from 2015-2019. No discernible migration of the ACC fronts is found in the total and geostrophic velocities, in agreement with Kim and Orsi [2014] and Swart et al. [2018].

We estimate trends in the transport over the along-track 25 km distance grid boxes for the total, geostrophic, and reference components using the full-sampling periods (Fig. 4.7d-f). In accordance with the trends in velocity, trends in the transport components per along-track distance show opposing trends occurring across Drake Passage. Acceleration of the upper ocean in between the Subantarctic Front and Polar Front is evident for the total component ($0.15 - 0.20$ Sv year^{-1}; Fig. 4.7d), which also can be found in the geostrophic (0.14 Sv year^{-1}; Fig. 4.7e) and reference (0.06 Sv year^{-1}) components, although the latter is not significant. Significant acceleration for the reference component is found in the core of the Polar Front (400 km). Near the South American shelf, the deceleration of the total transport reflects the strong deceleration of the reference transport ($0 - 50$ km, Fig. 4.7a,c), which overwhelms the acceleration of the geostrophic transport (Fig. 4.7b). Interestingly, the shipboard ADCP data shows an acceleration of the Southern ACC Front (Fig. 4.7a); no significance is calculated in the geostrophic velocity as not all transects have XBT drops across the front.

Clear patterns in the trends in transport emerge for the total, geostrophic, and reference

transport after using common sampling periods (Fig. 4.8). For the period of October 2005-April 2019 (dashed lines in Fig. 4.8), the largest acceleration of the transport is located at 200 km, roughly in between the Subantarctic Front and Polar Front, and deceleration extends from 300 km to north of the Southern ACC Front ($\sim 750-800$ km), where a small but significant acceleration is found. The acceleration peak in the reference transport at 200 km is split into two positive trends located around 180 km and 400 km (with the same magnitude) when the data between November 1999-April 2019 is used (solid lines in Fig. 4.8d). This result possibly stems from the strong meandering of the ACC fronts: the Subantarctic Front and Polar Front meandering south and northward for synoptic episodes would contribute to an apparent acceleration in this region. The spatial asymmetry of the opposing trends in the transport as a function of distance explains why no trend is discernible in the transport integrated across Drake Passage (Figs. 4.4,4.5). While the main area between the Subantarctic Front and Polar Front is accelerating the most, accompanied by the small acceleration of the Southern ACC Front, a compensating deceleration is found in the rest of Drake Passage. Chidichimo et al. [2014] noted that the cDrake baroclinic transport north of the Subantarctic Front tends to offset the transport in the central Drake Passage, comprising the area from the Subantarctic Front to the Southern ACC Front, for synoptic to monthly time scales. Our study suggests that different frontal regions across Drake Passage tend to compensate each other on longer-than-monthly scales, such that insignificant or no trends are found in the transport integrated across Drake Passage time series.

4.6 Changes in the baroclinic structure of Drake Passage

4.6.1 The 20-year mean salinity S and potential temperature θ

Mean sections of S and θ across Drake Passage are shown in Fig. 4.9. Relatively warm water masses ($\overline{T} > 2^{\circ}$C) are located < 400 km alongtrack. Salinity stratification is the weakest north of the Polar Front where the isotherms are more parallel to neutral density layers γ, indicating

temperature dominance for the stratification (gray contours, Fig. 4.9). The Subantarctic Front (150 km; maximum subsurface temperature gradient between $3° - 5°$C at 300 m) marks the region with the strongest temperature stratification and lateral gradients. South of 400 km, fresh ($\overline{S} < 34.25$) and relatively cold ($\overline{T} \sim 1°$C) water in the upper 100 m corresponds to the Antarctic Surface Water (AASW). In the mean, the AASW is composed of a remnant subsurface tongue of cold Antarctic Winter Water (AWW; $\overline{T} < 1°$C) with warmer surface waters occurring above during summer [Sprintall, 2003]. The northernmost extension of the subsurface AWW marks the location of the Polar Front, the boundary with the subtropical warm waters. This region is characterized by the largest variability in temperature and salinity (white contours, Fig. 4.9). Below the AWW, the dense Upper Circumpolar Deep Water (UCDW; $\overline{T} \sim 2°$C, $\overline{S} > 34.40$) is very homogeneous in temperature and has the smallest variability in both temperature and salinity. The UCDW is the result of North Atlantic Deep Water mixing with deep waters in the Indian and Atlantic sectors of the SO [Sprintall, 2008]. UCDW moving poleward where the ACC is the closest to the Antarctic continental shelf is modified due to stirring and coastal circulation, and this modified water dominates basal melt of the ice shelves.

4.6.2 Trends in isopycnal spice and heave

The Drake Passage trends in potential temperature and salinity, decomposed into trends in spice, heave, and total (eq. 4.7, 4.8), show spatial heterogeneity associated with the different dynamical regions of the ACC (Fig. 4.10). Within and north of the Subantarctic Front (< 200 km), significant warming and salinification due to spiciness (Fig. 4.10a,d) dominate the total trends (Fig. 4.10c, f). The significant warming and salinification could be partially tied to the upper 1000 m warming found in the Pacific sector of the SO, specifically, north of the Subantarctic Front [Shi et al., 2021]. Although Drake Passage restricts the eastward flow of subtropical waters north of the Subantarctic Front, it is possible that a small portion of the warmed subtropical waters [Shi et al., 2021] could make it through Drake Passage due to mesoscale advection or boundary

currents [Brearley et al., 2014]. Spice-related cooling and a small but significant freshening dominate in the south flank of the Polar Front ($500-600$ km) below 150 m depth (Fig. 4.10a). This cooling/freshening trend is likely subsurface water upwelled along isopycnals [Foppert et al., 2016] due to an increase of the westerly wind stress over the ACC [Marshall, 2003], therefore, resulting in northward Ekman heat transport. Sprintall [2008] found cooling trends at the surface south of the Polar Front although a factor of two smaller as they are averaged over the entire area south of the front for 1969-2004. Our results confirm that the cooling trend has continued since and that it might have intensified in the last decade and a half.

Heave decomposition in the Polar Front shows opposing trends in temperature south of the Polar Front (Fig. 4.10b). In the upper 150 m, cooling is associated with shoaling of the neutral density layers enclosing the AWW. Below this layer, strong warming is associated with warm-salty UCDW moving upwards, producing the largest trend in the last 20 years (Fig. 4.10e). This warming trend overwhelms the spice-related weak freshening (Fig. 4.10d), such that the total trend in depth is driven by the heave component (Fig. 4.10f). The total warming found near the core of the Southern ACC Front (Fig. 4.10c) has both spice and heave components playing an almost equal role. The warming south of the Polar Front was not statistically significant or almost negligible for the period of 1969-2004 [Sprintall, 2008]. Auger et al. [2021] found warming for the UCDW between 250-450 m south of Tasmania over the last decade with little of the trend attributable to interannual variability. Auger et al. [2021] suggested that the warming of the UCDW could be due to freshening at the base of the AWW, resulting in stronger stratification that would reduce mixing between the two layers and heat removal from the UCDW. Nonetheless, the positive salinity trend found in this study at the core of the UCDW due to spice suggests that the warming due to the freshening of the AWW might not hold for the Drake Passage area.

4.6.3 The role of wind

We examine whether the increase in the cooling in the upper 200 m and warming below 200 m south of the Polar Front is due to long-term increases in the wind stress curl over the SO and Drake Passage. To do this, we used the ERA5 monthly-time series of wind velocity components [Hersbach et al., 2020] to estimate trends of the SO vertical component of the wind stress curl $\mathbf{k} \cdot \nabla \times \tau$, where τ is the wind stress vector estimated following Fogt and Bromwich [2006] and ∇ is the gradient operator. The seasonal cycle was removed from the wind stress curl time series before computing the trends.

Upwelling (negative wind stress curl) trends are significant and peak in three distinct regions along the ACC path (Fig. 4.11a): 1) south of the Aghulas current ($10^\circ - 40^\circ$E), 2) south of Australia ($120^\circ - 160^\circ$E), and 3) in and downstream of the Drake Passage area ($70^\circ - 20^\circ$W). With the exception of the Agulhas region, the ACC is closer to the Antarctic continental shelf in these upwelling regions, where the UCDW is pushed towards the Antarctic ice shelves. Trends of the zonally averaged wind stress curl in Drake Passage range between -0.06×10^{-6} and -0.04×10^{-6} N m^{-3} year^{-1} south of 58°S, the typical mean position of the Polar Front in Drake Passage (Fig. 4.11b). Assuming that eddy-driven upwelling and other vertical motions such as diapycnal mixing are negligible, a rough estimate of the magnitude of the Ekman suction trend is obtained by

$$w_e = \frac{1}{\rho f} \mathbf{k} \cdot \nabla \times \tau, \tag{4.13}$$

where $\rho = 1030$ kg m^{-3} and $f = -1.26 \times 10^{-4}$ s^{-1} are the seawater density and Coriolis parameter for 60°S. Using the wind stress curl trends for Drake Passage, the average change of vertical velocity due to Ekman suction ranges between $5 - 3 \times 10^{-7}$ m s^{-1} year^{-1}, which over the course of 20 years yields an upward vertical velocity change of $6 - 9 \times 10^{-6}$ m s^{-1}. This amounts to an additional $290 - 190$ m of wind-driven upward vertical displacement of neutral density

layers. Similar estimates were found in the SO using a coarser horizontal resolution wind product for the 2000-2014 period [Meehl et al., 2019]. The upwelling of warm and salty UCDW below the mixed layer could minimize AWW's formation, which could eventually produce a warmer water column. Whether this warming could potentially preclude the formation of AWW due to the increase of the wind stress and wind stress curl over the SO in response to the continuing increase of greenhouse gas emissions warrants future research.

4.7 Trends in a time-varying streamline coordinate frame

To determine the trends across Drake Passage as a function of the ACC frontal regions, we estimated the transport time series and trends in a synoptic streamwise coordinate system in a similar way as used by Gutierrez-Villanueva et al. [2020] for eddy heat flux. We used a combination of the mean dynamic topography [Maximenko et al., 2009], updated with 20 years of altimetry data, and the daily maps of sea level anomalies from AVISO to track the position of the ACC streamlines. We employed "method 1" from Gutierrez-Villanueva et al. [2020] for the binning of the velocity data. This method provides an algorithm to attribute and bin data on occasions when a transect crosses the same front more than once. For example, transects often cross the Subantarctic Front twice, as it turns steeply from eastward to northward following the South American shelf break, forming meanders that can detach as eddies with closed contours. Velocity data falling within each pair of streamlines is then integrated vertically and in distance to form a transport estimate per pair of streamlines per transect. Total velocity u_{tot} is re-interpolated to a $\sim$ 11 km along-track distance (similar to that of the u_{geo} and u_{ref}) so that the criterion of one point per pair of streamlines per transect is met. The period of October 2004-April 2019 is employed as it is the common sampling period between the total OS38 and the geostrophic components.

The total, geostrophic, and reference transport time series are mostly eastward even

between the major ACC fronts (Fig. 4.12a,c,e), where recirculation and westward flow are evident in the mean 2D flow [Lenn et al., 2011]. The mean total transport per pair of streamlines is maximum within the Subantarctic Front and Polar Front; transport integrated across the fronts reaches maxima of 14 Sv and 17 Sv, respectively (Fig. 4.12b). Geostrophic transport is also maximum at the fronts with 2.5 Sv and 3.7 Sv for the Subantarctic Front and Polar Front respectively (Fig. 4.12d). Mean eastward geostrophic transport is found south of the Polar Front, as no recirculation or westward flow events are captured in the geostrophic component. The mean reference transport is 7 Sv and 8 Sv for the Subantarctic Front and Polar Front (Fig. 4.12f). The reference velocity captures more westward events south of the Polar Front. Mean transports show no significant differences when computed using all transects or the transects along the most repeated line (Fig. 4.12b,d,f).

The total transport shows opposing trends: almost equal acceleration in the Subantarctic Front and Polar Front, and deceleration between these fronts and south of the Polar Front (Fig. 4.13a). In contrast, the trends in the total transport as a function of distance show acceleration between the fronts (Fig. 4.8d). A positive, but insignificant trend is observed in the Southern ACC Front (Fig. 4.13a). The trends in the total transport suggest an acceleration of the ACC fronts and deceleration of the recirculation regions in between the fronts, although no significant trend is found within the fronts in the geostrophic transport (Fig. 4.13b).

4.8 Summary and discussion

This study used a unique time series of along-track upper-ocean temperature, salinity, and ocean velocity across Drake Passage, the narrowest constriction of the ACC, to estimate trends in the ACC total and baroclinic transport over the last 20 years. These observations from XBT/XCTD and shipboard ADCP allowed us to estimate and analyze trends across the different frontal regions of the ACC. We uniquely found that, although the total and baroclinic transport

integrated across the Drake Passage does not show statistically significant trends, the Subantarctic Front and Polar Front are accelerating between 0.1-0.2 Sv year^{-1} in the upper 970 m, whereas the area between these fronts is deaccelerating at -0.1 Sv year^{-1}. Similarly, the region South of the Polar Front shows deceleration and the Southern ACC Front shows acceleration although not significant. These trends are significantly larger than those found in the Argo global data set, north of the Subantarctic Front in the Pacific sector of the SO [Shi et al., 2021]. The opposing trends found across the different dynamical frontal regions are likely responsible for the lack of trends in the total Drake Passage transport found in this study as well as some others [e.g. Shi et al., 2020, 2021]. Long-term observations with sufficiently high resolution to resolve the different ACC frontal regions are needed to observe low-frequency trends.

This study found asymmetry in trends in temperature and salinity across the different frontal regions occurring over the last 20 years. Warming and salinification were found in the northernmost region of the ACC, between the Subantarctic Front and the South American shelf break; the trends are mostly along-isopycnal (spice) driven. The warming found in this region may be linked to the acceleration of the Subantarctic Front; warm water increasing the steric height of the front increases the lateral gradients, thus the velocity within the front. How the warm water moves into this region along isopycnals remains unclear. Drake Passage represents an important barrier for subtropical waters moving eastward north of the ACC streamlines; however, heat advection due to mesoscale eddies could act as a mechanism to move warm water into Drake Passage along the south American boundary [Brearley et al., 2014].

South of the Subantarctic Front and in the core of the Polar Front, cooling dominated the signal. The magnitude of the cooling is in accordance with the sea surface temperature trends found for the SO and Drake Passage [Auger et al., 2021]. The increase in the westerly wind stress [Fogt and Marshall, 2020] brings cool and fresh water from depth along isopycnals to near the surface, and pushes it northward. In contrast to the warming-driven acceleration of the Subantarctic Front, the Ekman-driven cooling trend near the surface is pushed into the cool (south)

flank of the Polar Front, which decreases the steric height, therefore increasing the gradients across the front. The increase in the steric height gradients across the front accelerates the flow, and therefore the transport, within the front as found in this study. Hogg [2010] and Shi et al. [2020, 2021] emphasize that buoyancy forcing rather than wind stress drives a major acceleration of the eastward flow in the SO through thermal wind shear. In particular, atmospheric heat uptake by the ocean has been identified as a major player in driving the acceleration of the upper ocean [Shi et al., 2021]. We suggest the acceleration of the fronts is driven by an increase in the eddy activity in between the fronts, consistent with the eddy saturation state. The buoyancy changes in the Subantarctic Front and Polar Front increase the tilting of the front's isopycnals, therefore, the potential energy stored in the front is subsequently released from the front through baroclinic instabilities. The eddies moving in the region between the fronts could eventually accelerate the flow when moving closer to the fronts by momentum transfer from eddies to the fronts. The potential increase in the eddy activity in the northern Drake Passage also has implications for the overturning circulation. The increase in the northward Ekman transport over the last two decades is compensated by eddies through the increase of deep poleward eddy heat flux across the fronts. Given the continuing increase in the global greenhouse emissions, we expect that the zonal westerly wind stress over the ACC to continue increasing, which would continue to bring cold water northward, therefore the eddy activity (thus eddy saturation and compensation) and zonal acceleration of the fronts would continue or even increase. Continuing the monitoring of the upper ocean temperature, salinity, and ocean currents in the upper kilometer of Drake Passage is needed to better understand how the ACC and SO are responding to global climate change.

An important result in our study is the significant warming and salinification of the southern Drake Passage region over the last 20 years. The shoaling driven by an increase of the negative wind stress curl (i.e. increase in the upwelling) dominates and overwhelms the cooling and freshening along isopycnals between 200-300 m. Similar patterns are found in the SO along 140°E [Auger et al., 2021]. The wind stress over Drake Passage brings up UCDW which warms

the cold AWW tongue that lies above. The warming and salinification due to UCDW could minimize the formation of AWW, which eventually could produce a warmer and saltier water column. In addition, UCDW has been identified as a major player in basal ice-shelf melt in the Western Antarctic Peninsula sector [Meehl et al., 2019, and references therein]. Our results suggest that the increase in wind-driven upwelling in this sector could facilitate the movement of the relative warm UCDW closer to the Antarctic shelf break where it can make its way onto the shelf due to mesoscale eddy advection and stirring [Palóczy et al., 2018], therefore, accelerating the basal melt with potential impacts in climate and sea-level rise.

4.9 Acknowledgments

We acknowledge the National Science Foundation's Office of Polar Programs (OPP) and Division of Ocean Sciences (OCE) for support of the Drake Passage time series and this research through grants OPP-2001646 and OCE-1755529. XBT temperature data were made available by the Scripps High-Resolution XBT program (http://www-hrx.ucsd.edu). The XBT probes are provided by NOAA's Global Ocean Monitoring and Observing Program through Award NA20OAR4320278. ADCP time series were acquired and processed by the Chereskin Lab at Scripps Institution of Oceanography (http://adcp.ucsd.edu/lmgould/) and can be downloaded from the Joint Archive for Shipboard ADCP (JASADCP) (http://ilikai.soest.hawaii.edu/sadcp/). The SSALTO/DUACS altimeter products were produced and distributed by the Copernicus Marine and Environment Monitoring Service (CMEMS) (http://www.marine.copernicus.eu). The ERA5 monthly wind data [Hersbach et al., 2020] was downloaded from the Copernicus Climate Change Service (C3S) Climate Data Store (https://cds.climate.copernicus.eu). The results contain modified Copernicus Climate Change Service information 2020. Neither the European Commission nor ECMWF is responsible for any use that may be made of the Copernicus information or data it contains. Finally, we are also grateful to the captain and crew of the

ARSV *Laurence M. Gould* and the Antarctic Support Contractor for their excellent technical and logistical support.

Chapter 4, in part, is currently being prepared for submission for publication of the material. Gutierrez-Villanueva M. O., T. K. Chereskin and J. Sprintall. The dissertation/thesis author was the primary investigator and author of this material.

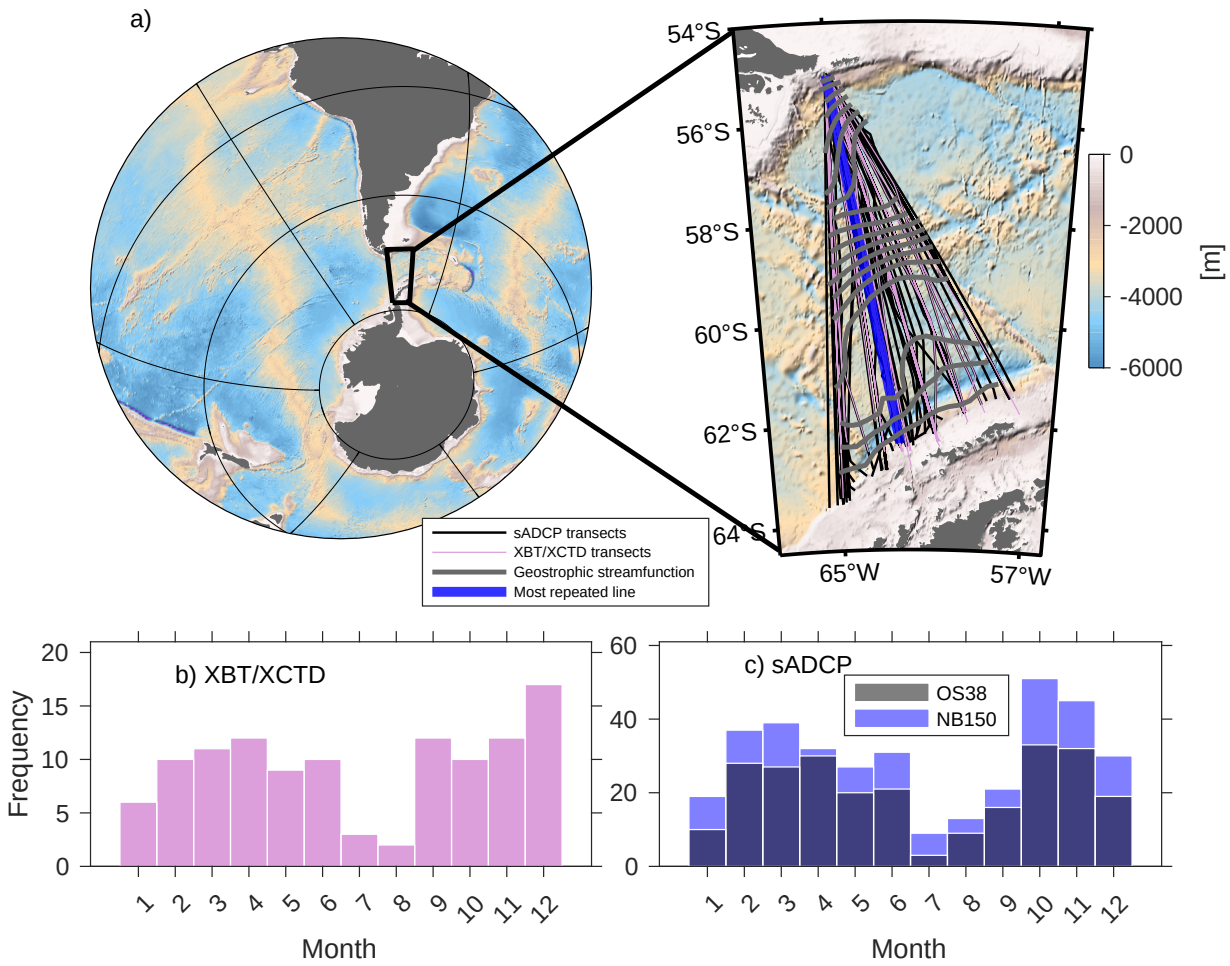

Figure 4.1: a) Area of study. XBT/XCTD (pink) and sADCP (gray) transects are shown in the zoomed Drake Passage area. Thick dark gray contours are the surface geostrophic streamfunction calculated from the NB150 transects (November 1999 - December 2019). The most repeated line is indicated in thick solid blue. (b) The number of XBT/XCTD transects found for each climatological month. (c) Light gray and blue show the histograms for the OS38 and NB150 ADCP.

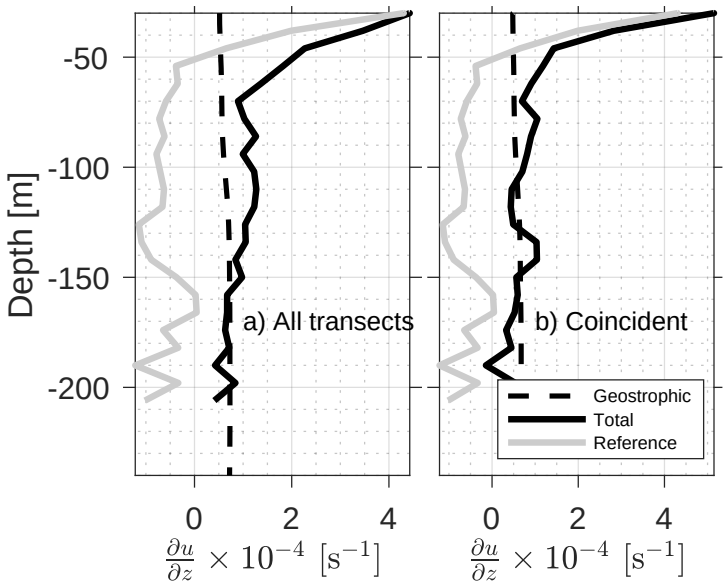

Figure 4.2: 20-year mean shear $\frac{\partial u}{\partial z}$ [s^{-1}] profiles for cross-transect total velocity $\frac{\partial u}{\partial z}_{tot}$ profile from the NB150 ADCP (thick black), geostrophic velocity $\frac{\partial u}{\partial z}_{geo}$ from the XBT/XCTD transects (thick dashed), and the residual profile $\frac{\partial}{\partial z}(u_{tot} - u_{geo})$ (thick gray). a) Geostrophic and total shear use all transects available. b) Uses the 98 coincident NB150-XBT/XCTD transects.

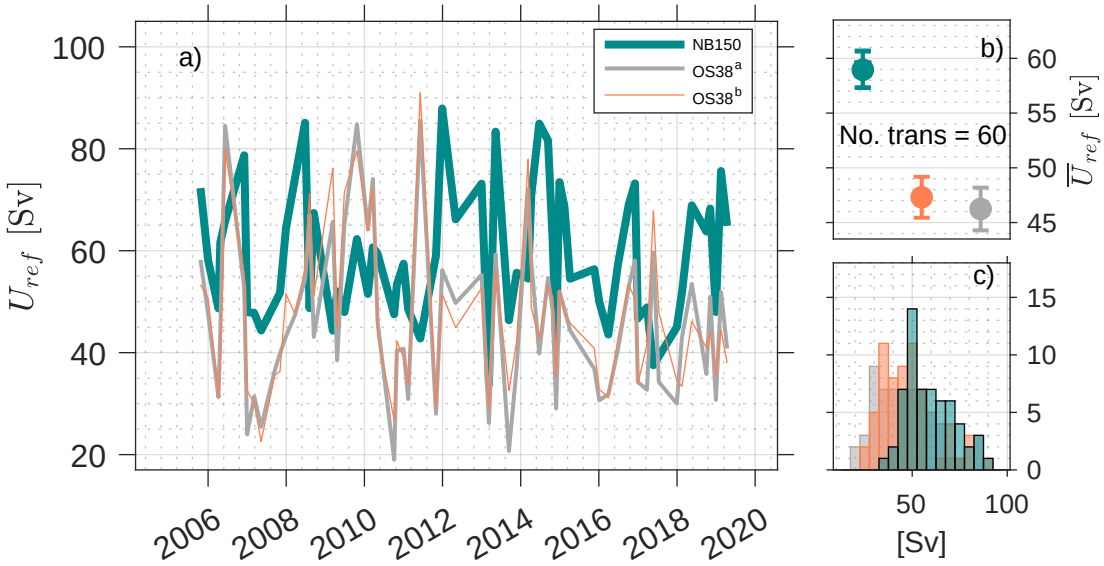

Figure 4.3: a) Times series of reference transport U_{ref} [Sv] from October 2005-April 2019 for the OS38 U_{ref} calculated using the OS38 $u_{tot} - u_{geo}$ averaged from 90-210 m (OS38^a, gray solid line), averaged from 90-760 m (OS38^b, thin salmon solid line). Thick dark cyan line shows U_{ref} using the 20-year NB150 u_{ref} estimated using $u_{tot} - u_{geo}$ from 90-210 m. b) Mean reference transport $\overline{U}_{ref}$ [Sv] calculated for the period October 2005-April 2019. The number of coincident transects used for estimating the time averages is indicated. Error bars are the standard error. c) Histograms of U_{ref}.

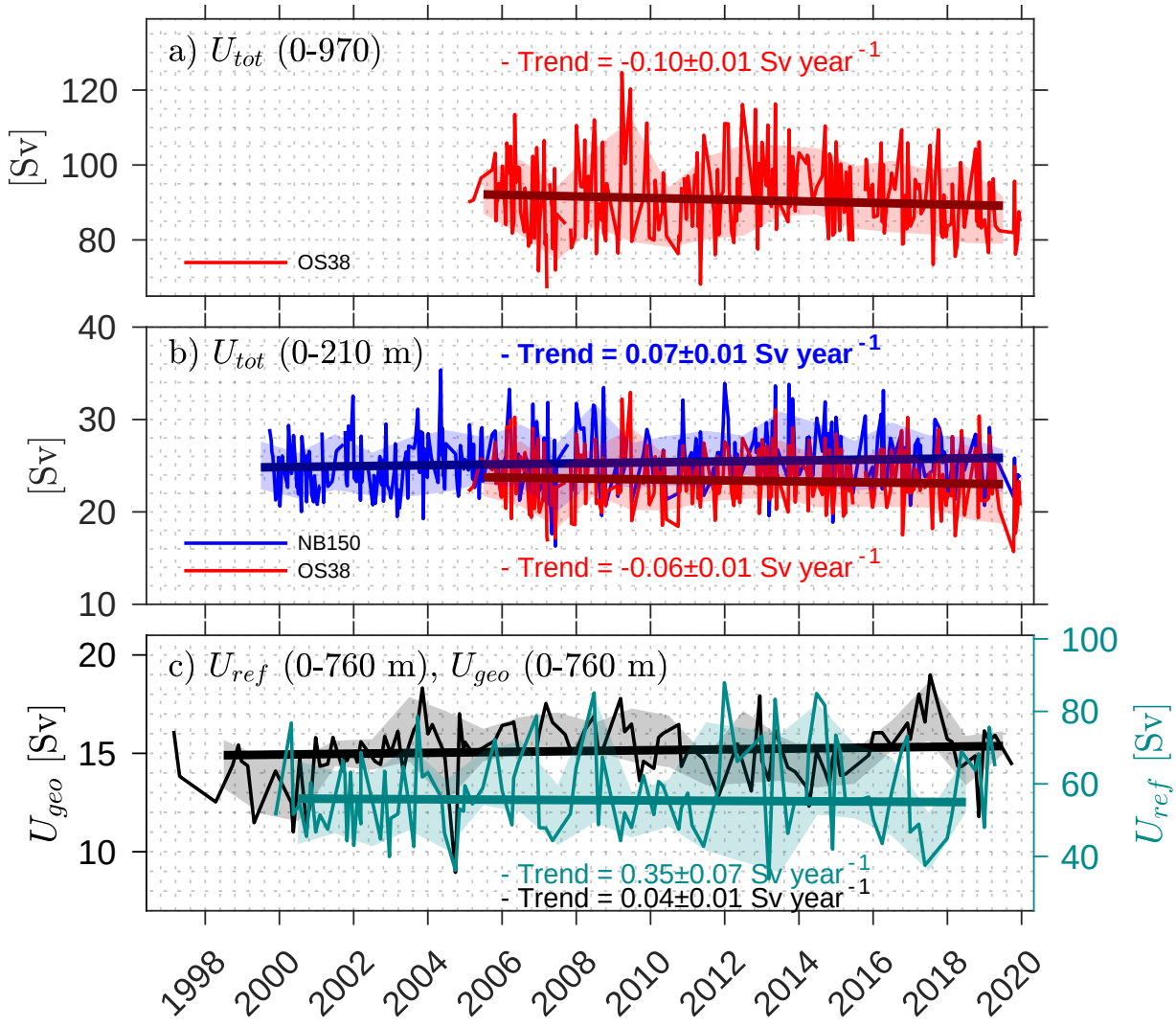

Figure 4.4: Time series of transport integrated across Drake Passage (thin solid) [Sv]: a) U_{tot} for the OS38 time series (red), b) U_{tot} for the NB150 (blue) and OS38 (red) in the upper 210 m, and c) U_{geo} (black) and U_{ref} (dark cyan) in the upper 760 m. The U_{ref} times series corresponds to the 20-year NB150 time series. Standard deviations for each calendar year are shown in shaded areas. Linear fit for the time series with the seasonal cycle removed is shown in thick solid line. Least-squares trends and 95% confidence limits are shown in text [Sv year^{-1}]. Bold text in (b) indicates that trend is significant after the modified Mann-Kendall test.

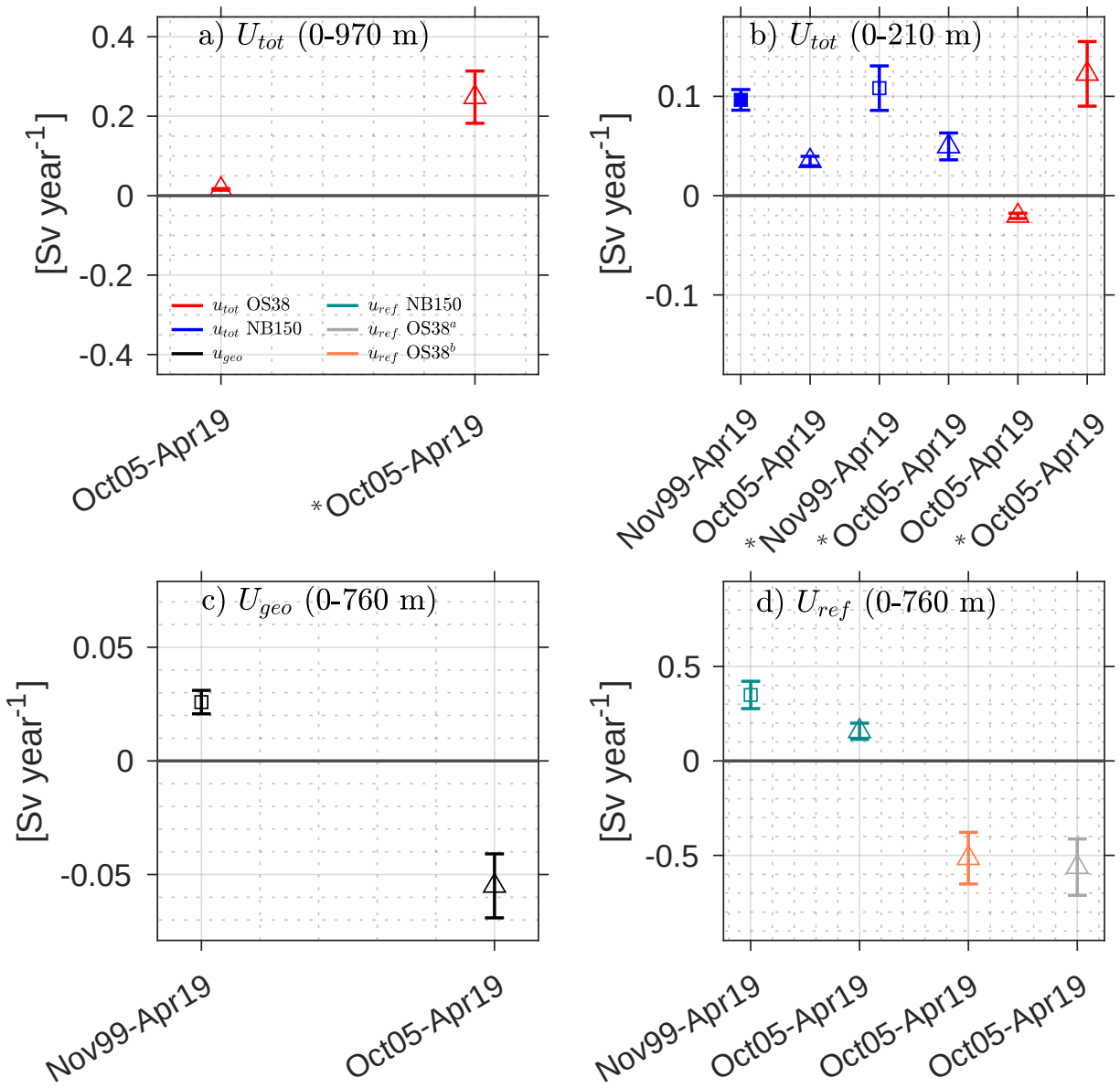

Figure 4.5: Trends [Sv year^{-1}] in transport integrated across Drake Passage: a) U_{tot} in the upper 970 m, b) U_{tot} in the upper 210 m, c) U_{geo} in the upper 760 m and d) U_{ref} in the upper 760 m. Vertical lines show the 95% least-squares confidence limits. Squares and triangles indicate that trend has been estimated using time series spanning November 1999-April 2019 and Oct 2005-April 2019, respectively. Filled symbols indicate that trend is 95% significant after the modified Mann-Kendall test. Red and blue colors indicate that the OS38 and NB150 U_{tot} time series are employed to estimate the trend in (a)-(b). Trends for U_{geo} using the XBT/XCTD time series are indicated in black. Trends in (d) U_{ref} calculated using the NB150, OS38^a and OS38^b time series are indicated in dark cyan, gray, and salmon (see Fig. 4.3a). Asterisk in the (a)-(b) x-axis indicates that only those velocity transects that have a coincident XBT/XCTD transect are employed. Different y-axis scales are shown for each plot.

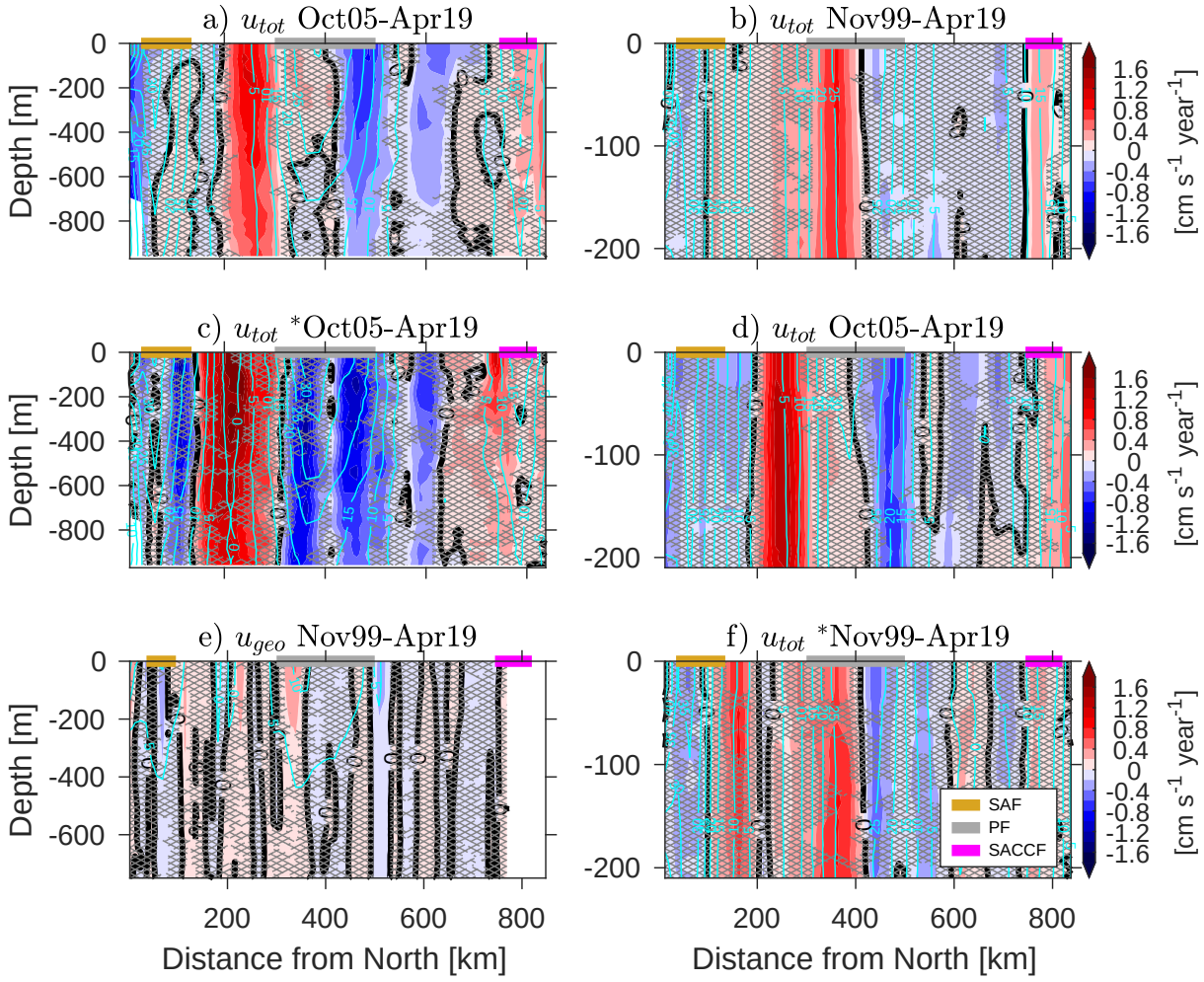

Figure 4.6: Trends in velocity [cm s^{-1} $year^{-1}$] as a function of distance from North [km] and depth [m] for a) u_{tot} in the upper 970 m (OS38), b) u_{tot} in the upper 210 m (NB150), c) u_{tot} in the upper 970 m (OS38) using only those transects that coincide with a XBT/XCTD transect, d) u_{tot} in the upper 210 m (NB150) using the OS38 sampling period, e) u_{geo} in the upper 760 m, and f) u_{tot} in the upper 210 m (NB150) using only those transects that coincide with a XBT/XCTD transect. Sampling periods used for estimating trends are indicated. Filled contours are plotted every 0.2 cm s^{-1} $year^{-1}$. Black thick contour is the zero trend. Hatched areas indicate that trend is not significant at 95% confidence after the modified Mann-Kendall test. Cyan contours show the mean velocity for the sampling period and are plotted every 5 cm s^{-1}. Vertical scales vary for each panel. Horizontal gold, gray, and magenta indicate the mean location of the Subantarctic Front (SAF), Polar Front (PF), and Southern ACC Front (SACCF).

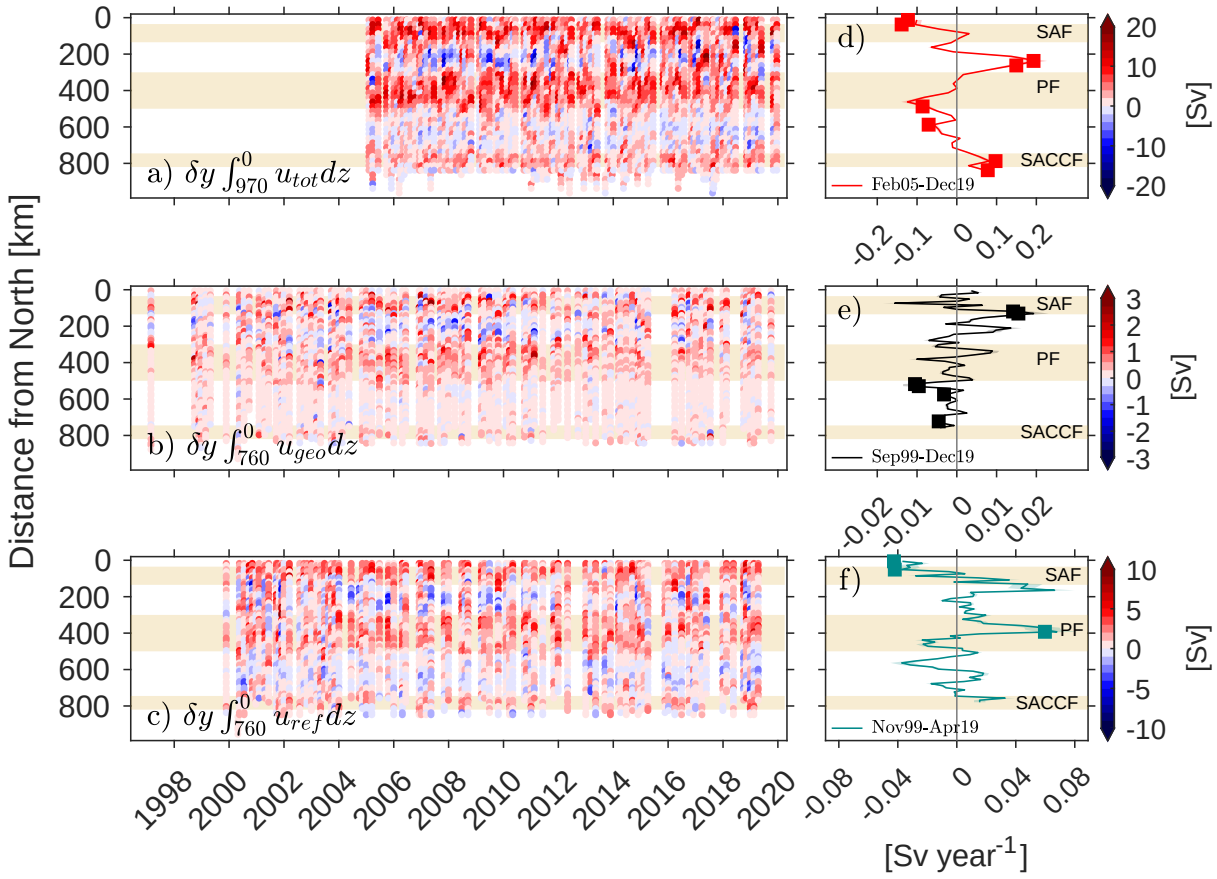

Figure 4.7: (a)-(c) Time series of transport per along-track distance box [Sv] for a) u_{tot} vertically integrated from 0-970 m, b) u_{geo} vertically integrated from 0-760 m, and c) u_{ref} vertically integrated (0-760 m). The u_{ref} times series correspond to the NB150 time series, (see Fig. 4.4c). δy is the along-track resolution: (a) 25×10^3 m and (b)-(c) 11×10^3 m. Notice the different color bar scales for (a)-(c). (d)-(f) Trends in transport per along-track distance [Sv year^{-1}] for d) u_{tot} using the OS38 from February 2005-December 2019 (red), e) u_{geo} from September 1999-December 2019 (black), and f) NB150 u_{ref} for November 1999-April 2019 (dark cyan). Shaded areas indicate the 95% confidence limits. Filled squares show statistically significant trends estimated with the Theil-Sen estimator. Similarly, different x-scales are used for the trends (d)-(f). Shaded areas show the locations for each of the ACC fronts: Subantarctic Front (SAF), Polar Front (PF), and Southern ACC Front (SACCF).

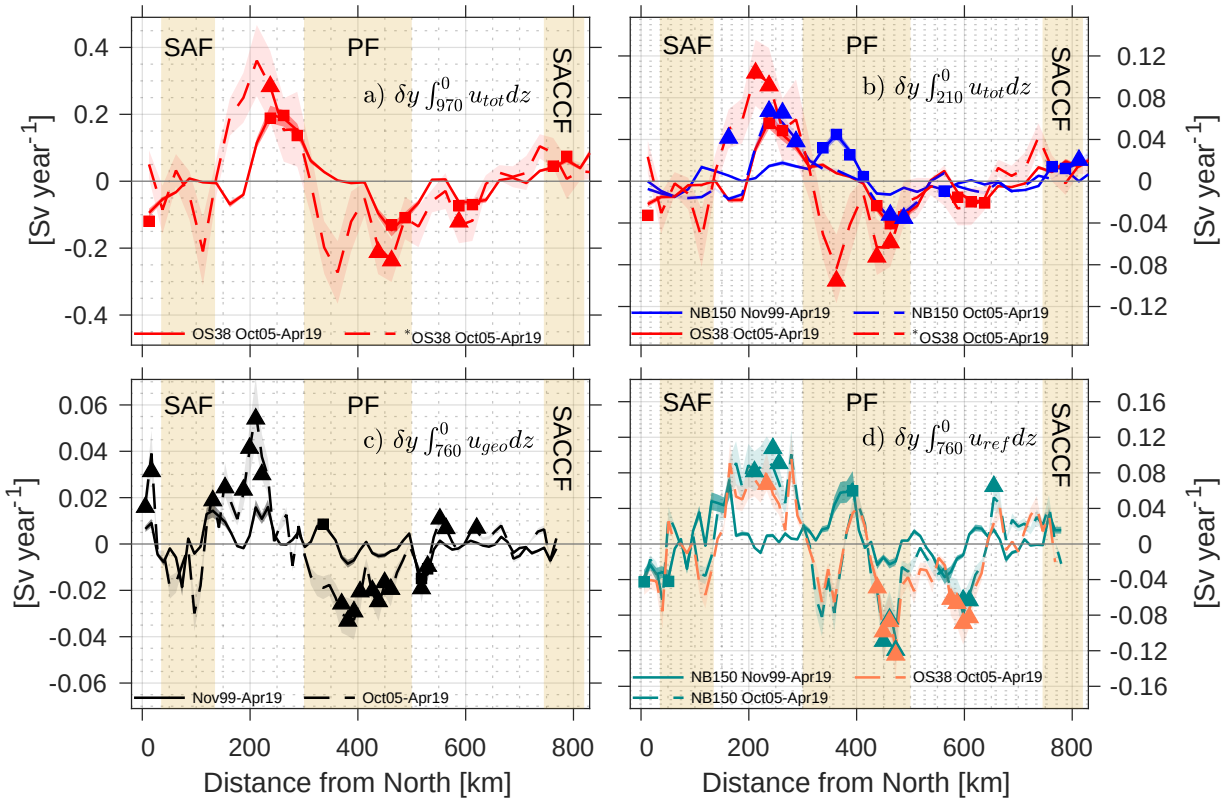

Figure 4.8: Trends in transport [Sv year^{-1}] per along-track distance for common sampling periods. a) Trends in u_{tot} vertically integrated from 0-970 m (red). b) Trends for u_{tot} vertically integrated from 0-210 m using the OS38 (red) and NB150 (blue) time series. c) Trend for u_{geo} vertically integrated from 0-760 m (black). d) Trends for u_{ref} vertically integrated (0-760 m) for the NB150 (dark cyan) and OS38^{b} (salmon) (see Fig. 4.3a). Shaded areas show the least-squares 95% confidence limits. Periods used to estimate trends are indicated in the legends. Asterisks in (a)-(b) legends indicate that trends are estimated using only those ADCP transects that have a concurrent XBT/XCTD transect. Filled symbols are statistically significant (after the modified Mann-Kendall test) trends estimated using the Theil-Sen estimator. δy is the along-track resolution: (a),(b) 25×10^3 m and (c),(d) 11×10^3 m. Vertical scales vary for each plot. Shaded areas show the locations for each of the ACC fronts: Subantarctic Front (SAF), Polar Front (PF), and Southern ACC Front (SACCF).

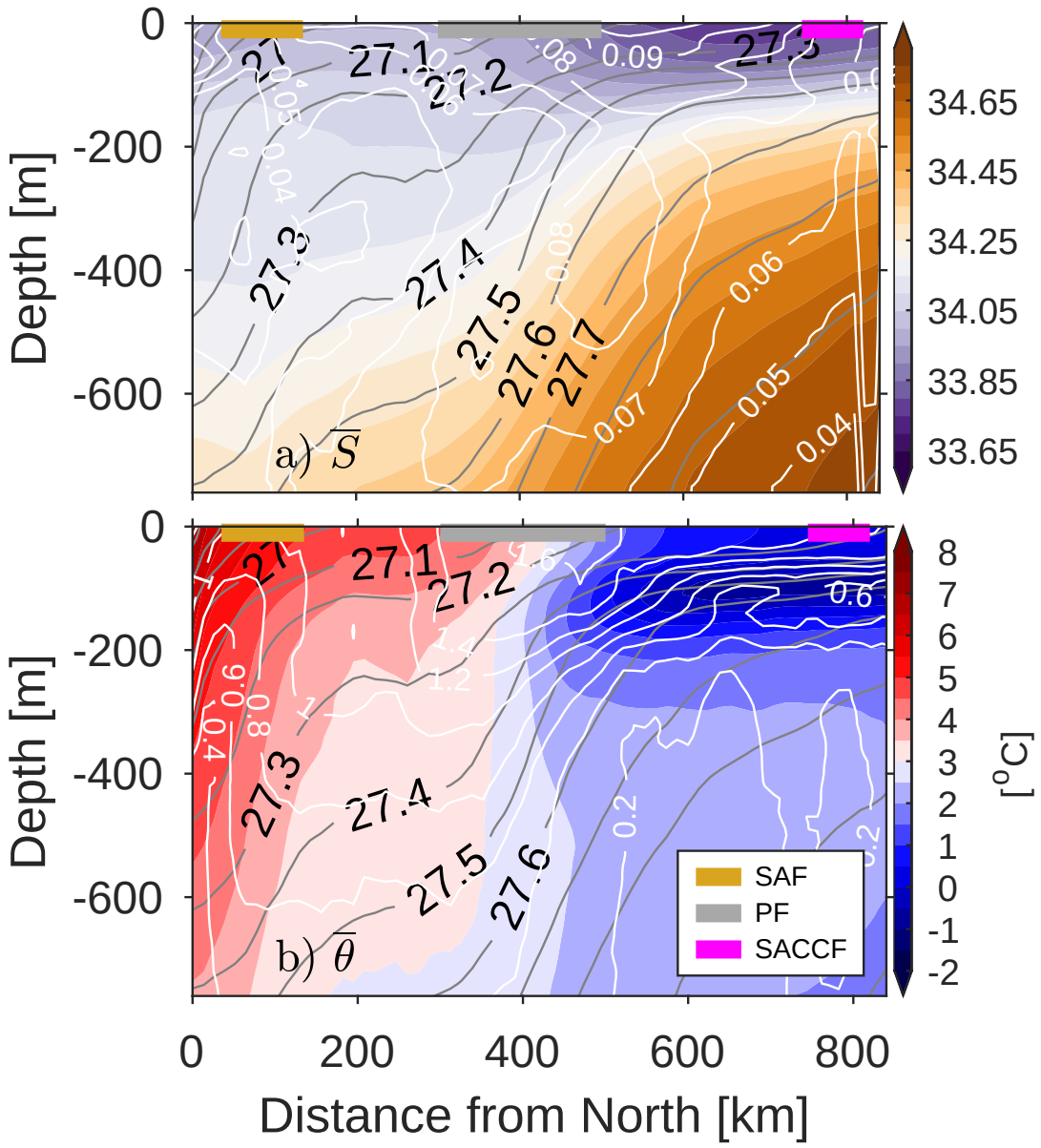

Figure 4.9: Mean a) potential temperature θ [°C] and b) salinity S across Drake Passage. All XBT/XCTD transects are used to estimate the 20-year mean. Standard deviations and mean neutral density surfaces are shown in white and gray contours respectively. Distance increases moving towards the Antarctica shelf. Horizontal gold, gray, and magenta bars indicate the mean location of the Subantarctic Front (SAF), Polar Front (PF), and Southern ACC Front (SACCF).

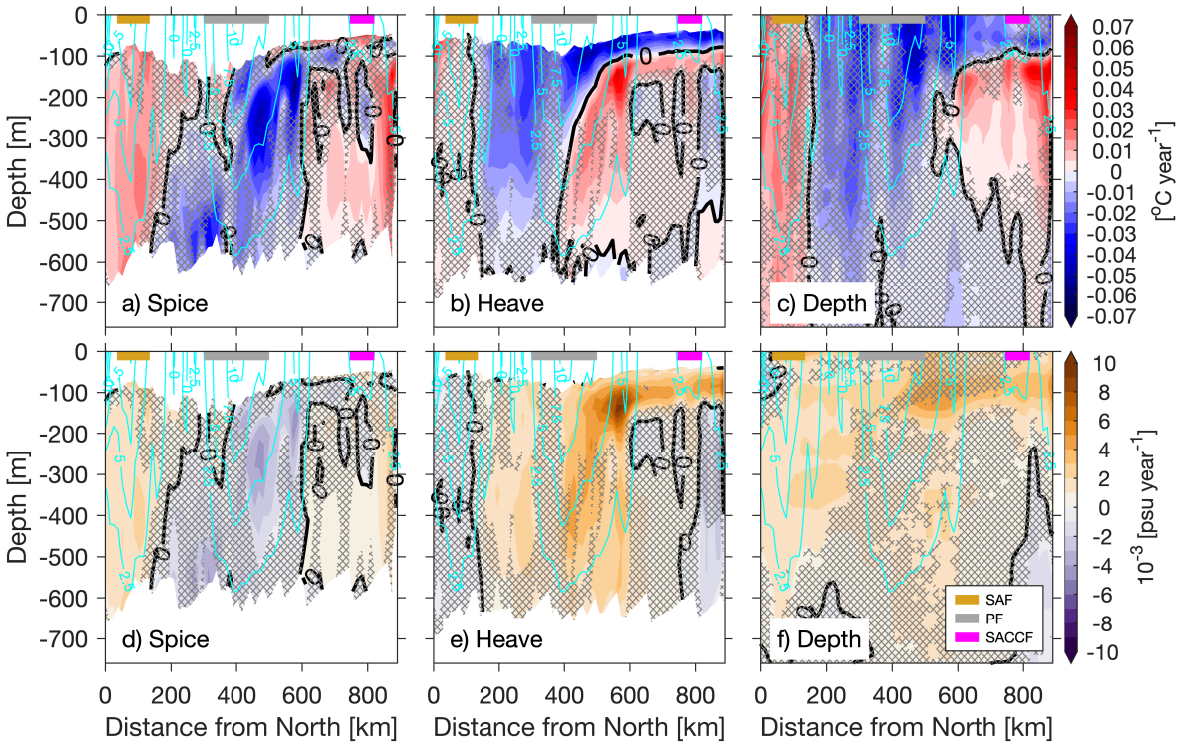

Figure 4.10: Trends in (a)-(c) potential temperature θ [°C year^{-1}] and (d)-(f) salinity [psu year^{-1}] decomposed in (a),(d) along neutral density "spice", (b),(e) isopycnal heave and (c),(f) depth or total trend. Warm color indicates warming and salinity increase for θ and S respectively. Black thick contour shows the zero trend. Hatched areas indicate that trends are not statistically significant after the modified Mann-Kendall test. Cyan contours show the 20-year mean u_{geo} plotted every 2.5 cm s^{-1}. Horizontal gold, gray, and magenta bars indicate the mean location of the Subantarctic Front (SAF), Polar Front (PF), and Southern ACC Front (SACCF).

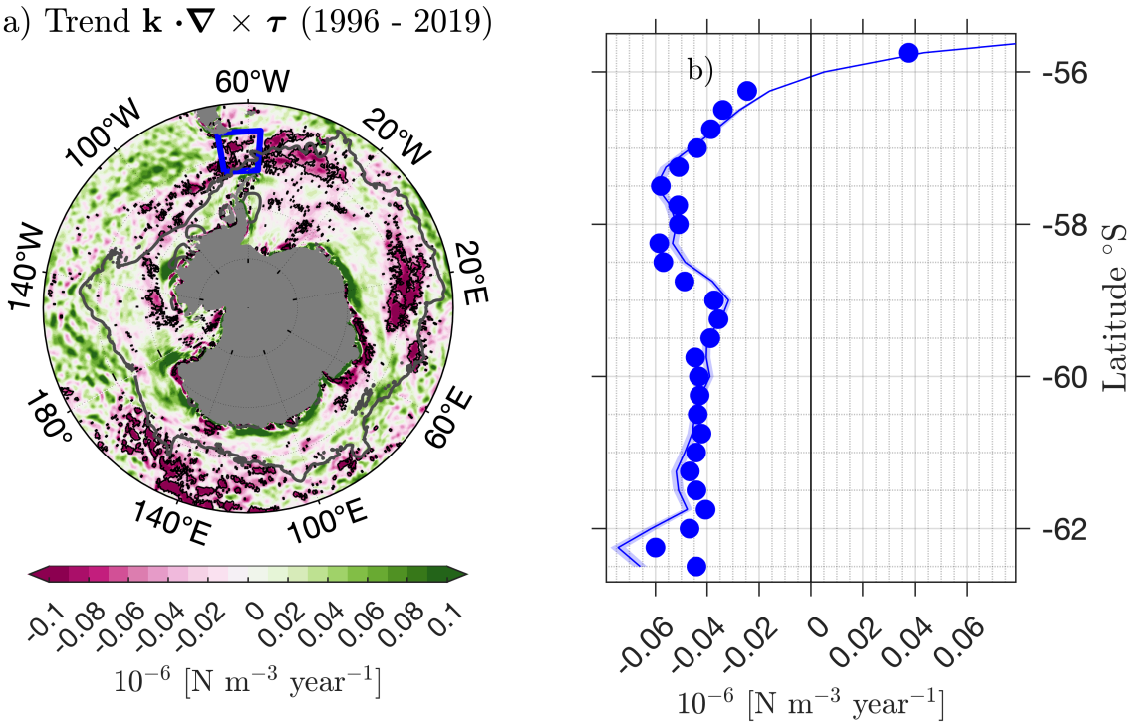

Figure 4.11: a) Trend in Southern Ocean wind stress curl $\mathbf{k} \cdot \nabla \times \tau$ [N m^{-3} year^{-1}] from 1996-2019, computed from ERA5 monthly-averaged wind stress. The seasonal cycle from the monthly wind stress curl time series is removed before computing the trends. Negative values denote areas of upwelling, i.e., Ekman suction moving water upwards. Areas enclosed by the black contour are statistically significant trends. Blue square denotes the Drake Passage area. The mean position of the Southern ACC Front is shown (gray contour). b) Trends of zonally-averaged wind stress curl in Drake Passage (blue square in (a)). Solid blue line and shaded area show the least-squares trend and the 95% confidence intervals. Filled circles show the statistically significant trend using the non-parametric tests.

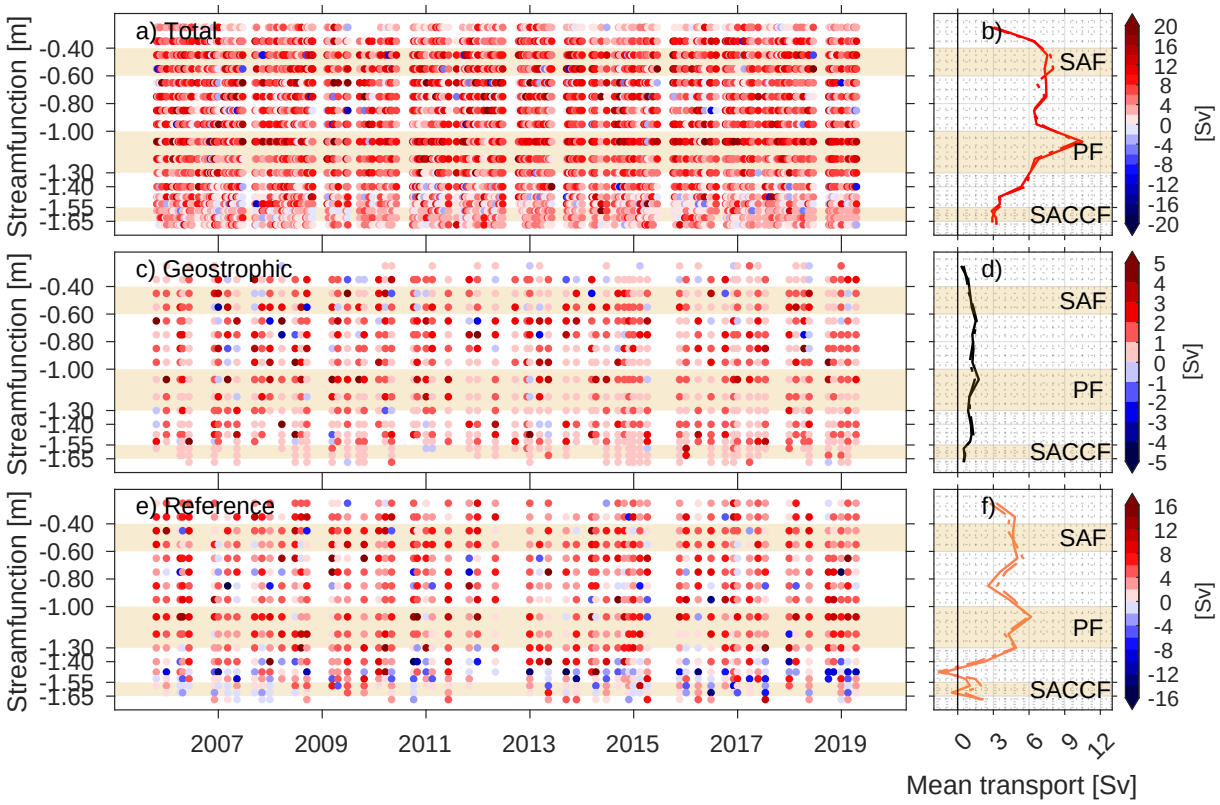

Figure 4.12: Time series of transport [Sv] per pair of streamlines for a) u_{tot} vertically integrated from 0-970 m, c) u_{geo} vertically integrated from 0-760 m, and e) u_{ref} vertically integrated (0-760 m). The u_{ref} times series correspond to the OS38^b time series, (see Fig. 4.3a). Note the different color bar scales for each time series. (b), (d), (f) Mean transport [Sv] per pair of streamlines. Solid and dashed-dot lines show the mean transport estimated for all transects available and only those along the most-repeated line (Fig. 4.1a), respectively, for October 2005-April 2019. Shaded areas show the streamwise intervals for each of the ACC fronts: Subantarctic Front (SAF), Polar Front (PF), and Southern ACC Front (SACCF).

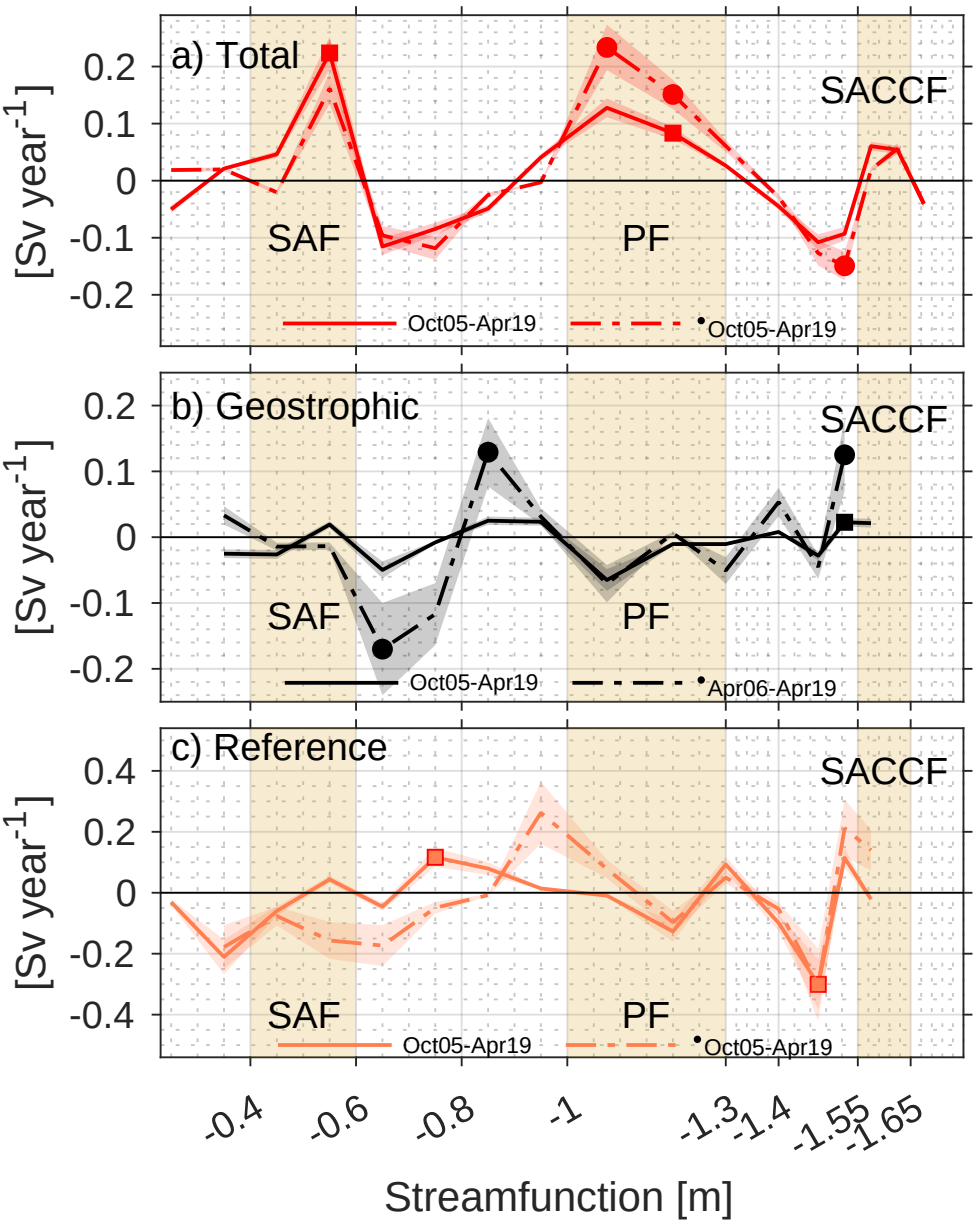

Figure 4.13: Trends in transport [Sv year^{-1}] per along-track distance for common sampling periods for a) u_{tot} vertically integrated from 0-970 m (red), b) u_{geo} vertically integrated from 0-760 m (black), and c) u_{ref} vertically integrated (0-760 m) for the OS38^{b} (salmon) (see Fig. 4.3a). Shaded envelopes show the least-squares 95% confidence limits. Periods used to estimate trends are indicated in the legends. Dashed-dot line (bullet in legend) indicates that trends are estimated using only those transects along the most-repeated line (Fig. 4.1a). Filled symbols are statistically significant (after the modified Mann-Kendall test) trends estimated using the Theil-Sen estimator. Vertical scales vary for each plot. Shaded areas show the streamwise intervals for each of the ACC fronts: Subantarctic Front (SAF), Polar Front (PF), and Southern ACC Front (SACCF).

Chapter 5

Conclusions and comments

5.1 Summary of major contributions

In this dissertation, the unique high-spatial resolution 20-year LMG temperature, salinity and underway ocean velocity time series across Drake Passage, and supplementary observations from the cDrake campaign [Chereskin et al., 2012] were utilized to study the eddy heat flux across the ACC [Gutierrez-Villanueva et al., 2020], finescale internal-wave-driven turbulence [Gutierrez-Villanueva et al., 2022] and transport of the ACC in Drake Passage. This work focused on analyzing the mean, spatial distribution and temporal variability of these quantities, and examined the possible physical processes and factors driving the spatial and temporal variability of these quantities.

In Chapter 2, the eddy heat flux as a function of ACC streamlines is quantified using the time series of upper ocean temperature and velocity transects with unprecedented horizontal resolution. In our analysis, we employed two different frameworks to calculate the along/across-transect eddy heat flux components: 1) a time-mean streamwise coordinate system, and 2) time-varying (time-mean plus daily maps of sea surface height) streamlines. One of the main results of this chapter is that the time-varying streamlines provide the best estimate of the across-

ACC eddy heat flux component as it allows to track the shifting and meandering of the ACC fronts. Using the time-varying streamlines, the depth-integrated (0-900 m) across-ACC eddy heat flux is maximum poleward in the south flank of the Subantarctic Front (-0.10 ± 0.05 GW m^{-1}) and reduces towards the south, becoming statistically insignificant in the Polar Front, indicating heat convergence south of the Subantarctic Front. Furthermore, the time series provide an uncommon opportunity to explore the seasonal cycle of the eddy heat flux. This chapter found that poleward eddy heat flux in the Polar Front Zone is enhanced during the austral fall-winter, suggesting a seasonal variation in eddy-driven upwelling.

Motivated by the idea that radiation and breaking of internal lee waves are thought to play an important role in the energetics of the SO, Chapter 3 estimated the linear lee-wave energy radiation and finescale turbulent mixing to quantify how much of the locally radiated lee-wave energy dissipates locally in Drake Passage. Previous studies [Trossman et al., 2015; Yang et al., 2018] suggested that lee-wave energy radiation estimates could come to a closer agreement with the local turbulent dissipation in the ACC by employing a two-dimensional anisotropic abyssal hill topography. This study found that regardless of the topography employed, less than 10% of the radiated lee-wave energy dissipates locally, which is smaller than that predicted by idealized numerical simulations [Nikurashin and Ferrari, 2010a].

Lastly, Chapter 4 estimated trends in the Drake Passage transport for the last two decades and analyzed the changes in the upper ocean temperature and salinity across Drake Passage driving these trends. To estimate trends, this chapter used the high-along-track resolution time series of velocity, temperature and salinity to estimate time series of total and geostrophic (referenced to 760 m) velocity, hence, transport. We uniquely found that the Subantarctic Front and Polar Front, the two major ACC fronts, have significantly accelerated during the last decade whereas the area between these fronts and between the Polar Front and the Southern ACC Front has decelerated. These opposite trends compensate such that no significant trend is discernible in the total and geostrophic transport integrated across Drake Passage. The temperature and salinity fields show

that the equatorward flank of the Subantarctic Front is warming whereas freshening and cooling dominates in the poleward flank of the Polar Front. We suggest the acceleration of the fronts is driven by an increase in the eddy activity in between the fronts, consistent with the eddy saturation state. The buoyancy changes in the Subantarctic Front and Polar Front increase the tilting of the front's isopycnals; therefore, the potential energy stored in the front is subsequently released from the front through baroclinic instabilities. The eddies moving in the region between the fronts could eventually accelerate the flow when moving closer to the fronts by momentum transfer from eddies to the fronts. Our results have implications for the overturning circulation. The increase in the northward Ekman transport over the last two decades is compensated by eddies through the increase of deep poleward eddy heat flux across the fronts, which potentially hints at an increase of the eddy-driven upwelling of deep warm waters in Drake Passage.

5.2 Significance and pathways of future research

This thesis work helps in our understanding of the role of the dynamics and physical processes that drive changes in the SO meridional overturning circulation and the ACC transport through Drake Passage. The results obtained from this work will provide a test-bed for future comparisons with those of global climate models. For example, the ACC transport through Drake Passage represents a metric for validating global models; finding discrepancies between observations and models will serve to identify errors or omitted physics in models, therefore model improvements may result. Additionally, this thesis work illustrates the importance of continuing sampling the Drake Passage with high-spatial resolution. Estimating upper-ocean eddy heat fluxes and trends in transport at the different fronts of the ACC with statistical significance can only be attained with continuous temporal sampling and high-spatial resolution.

Several outstanding questions that stem from this dissertation should be the focus of future research. For example, is it possible to observe and quantify a seasonal enhancement of the

eddy-driven upwelling of tracers such as heat, carbon, and other tracers in Drake Passage or other eddy hot spots? In Chapter 2, the seasonal cycle of the eddy heat flux suggests that eddy-driven upwelling in the northern half of Drake Passage is enhanced during winter. Future work ought to analyze this possible seasonal cycle of the eddy-driven upwelling in the SO, and to understand what are the possible consequences for the SO meridional global overturning and global climate. Do other hot spots of mesoscale activity in the SO show a seasonal cycle in the eddy heat flux across the ACC? Eddy-resolving data assimilation models such as the Southern Ocean State Estimate [Mazloff et al., 2010] could provide an useful tool to shed light on these questions.

Regarding the estimates of lee-wave energy in Drake Passage in Chapter 3, how does the energy radiation (loss) from the eddy flow to lee waves affect the amount of energy available for eddy growth? Is the eddy growth through baroclinic and barotropic instabilities tapered by the radiation of lee waves from the eddy flow? In this thesis chapter, it is shown that large energy from the eddy flow is converted to lee waves where baroclinic and barotropic instabilities processes are maximum in the Polar Front Zone. Therefore, it is reasonable to hypothesize that the energy conversion from the eddy flow to lee waves limits the amount energy available for eddies to grow. Idealized numerical simulations with lee-wave-resolving spatial resolution could further clarify and quantify the effect of the lee waves on the SO EKE pathways.

Additionally for Chapter 3, what percentage of the lee-wave energy can be reabsorbed back into the mean flow? What percentage goes into advection and remote dissipation? These questions are important to address as global climate models parameterize the turbulent dissipation profile and assume a constant fraction of local dissipation of lee-wave energy. Also, recent studies point out that the interaction of the slowly-variant flow with the barotropic tide over small-scale abyssal hill topography could suppress the energy radiated into lee waves [Shakespeare, 2020]. Future work using idealized numerical simulations tuned for the range of parameters found in this study, which incorporate both a slowly variant flow and the barotropic tide, could shed light on the fates of the excess of lee-wave energy radiation.

Next, our results in Chapter 4 open the debate if the acceleration of the ACC fronts is restricted to the Drake Passage area, or if the acceleration of the fronts can be seen along the path of the ACC. If the ACC streamlines around the SO converge and flow through Drake Passage, our results point out that there is indeed a clear acceleration of the ACC fronts in the SO. Global climate models with sufficient spatial resolution to resolve the ACC fronts and mesoscale length scales (run with realistic forcing) could provide a useful tool to compare this study's results and analyze whether other sectors of the SO show frontal acceleration.

Finally, the following questions stem from amalgamating the three chapters of this thesis work. How is the eddy field in Drake Passage altered due to the steepening of the isopycnals and acceleration of the ACC fronts? Has the eddy field reached a saturation state already? Also, do we expect more linear lee-wave energy generation and radiation given the acceleration of the ACC fronts? Since lee-wave radiation is the largest where the ACC fronts interact with rough topography, the expectation is that energy radiation increases as the near-bottom flow at the fronts intensifies. Moreover, have the lee-wave energy generation and radiation reached a saturation state such that lee-wave generation is insensitive to the flow speed, therefore, not removing more energy from the mean flow, such that the ACC flow has accelerated over the last decades? These questions have implications for understanding the current state of the SO meridional overturning circulation, and are pivotal to study and understand future climate scenarios.

Chapter 6

Appendices for Chapter 2: Eddy heat flux across the Antarctic Circumpolar Current

6.1 Appendix A

Here we detail three methods for rotation, binning and averaging of instantaneous eddy heat flux estimates employing a time-varying coordinate system. For the three methods, a general procedure was used for the rotation of individual eddy heat flux estimates for each transect and for the binning of data points (Fig. 6.1). For each transect, we located velocity and temperature data falling within: i) a specific pair of open streamlines Ψ_j^* and Ψ_{j+1}^* (method 1), where $j = 1, 2, \cdots, M-1$ (M is the total number of unique open streamlines), or ii) unique intersections between individual transects and open streamlines (methods 2 and 3). For methods 2 and 3, unique intersections were defined where the transect first intersects an open streamline moving in the along-transect direction. Multiple intersections for a specific open streamline were not allowed in methods 2 and 3, i.e. once the transect first intersects a streamline Ψ_j^* the along-transect direction is followed until the transect first crosses the next streamline Ψ_{j+1}^* (Figs. 6.1b,c). Next, individual heat flux estimates were calculated as in the time-mean streamwise coordinate system

(the position of each estimate was defined as the position of each temperature profile). The same procedure was used for rotating the eddy heat flux vector into along/across stream components as in the time-mean streamlines, except when data points fell inside closed contours (rings). In that case, the normal vectors found within a pair of open contours or pair of unique intersections that contained closed contours were re-interpolated using an inverse distance weighting method $\hat{\mathbf{n}}' = \frac{\sum_{i=1}^{m} \hat{\mathbf{n}} d^{-2}}{\sum_{i=1}^{m} d^{-2}}$, where $\hat{\mathbf{n}}'$ is the re-interpolated normal vector, m is the number of neighboring data and d is the distance from the m data to the point estimated (Fig. 6.1). The eddy heat flux vectors were then rotated counterclockwise by $\theta = \theta_{\hat{\mathbf{n}}'} - \frac{\pi}{2}$ where $\theta_{\hat{\mathbf{n}}'}$ is the angle of the re-interpolated normal vector. Finally, the resulting eddy heat flux components were binned and averaged first for each pair of streamlines per transect at each depth. Subsequently, each component was averaged to produce mean along-stream $\overline{u'T'}_{\Psi^*}$ and across-stream $\overline{v'T'}_{\Psi^*}$ eddy heat flux components per streamline at each depth. The following subsections list the steps undertaken for binning and averaging the eddy heat flux estimates for each method. In addition, a pair of open streamlines from Figure 6.1 is used to illustrate how the rotation was undertaken when data locations were found within closed contours (rings). These examples show how the binning was done for each method and they highlight the key differences among the methods. Lastly, the depth-integrated components calculated with methods 2 and 3 are shown in Appendix B. Method 2 yields larger values for the across-stream component in the SAF compared to methods 1 and 3 by almost a factor of 2. Methods 2 and 3 average over a much larger area covered by a pair of streamlines compared to method 1.

6.1.1 Method 1: area between a pair of streamlines

Here we outline the steps for the rotation, binning and averaging of individual eddy heat flux estimates for a pair of open streamlines defined as $\Psi^*_j \geq \Psi^* > \Psi^*_{j+1}$, with $j = 1, 2, \cdots, M-1$ (M is the number of unique streamlines used), $\Psi^*_{j+1} = \Psi^*_j - \Delta\Psi^*$ and $\Psi^*_{j=1}$ is the northernmost streamline (Fig. 6.1a). For each temperature transect:

1. Velocity and temperature data were found for each pair of streamlines and individual eddy heat flux estimates were calculated as undertaken for the time-mean streamlines.

2. Normal vectors were bilinearly interpolated to the individual heat flux positions.

3. For the cases when eddy heat flux positions were found within closed contours for a specific pair of open streamlines, all normal vectors enclosed by the pair of open streamlines were re-interpolated using the inverse distance weighting method.

4. Individual estimates were rotated using the angle θ to obtain the along-stream and across-stream components and were averaged per transect per pair of streamlines at each depth.

5. Each component was binned for the pair of streamlines and averaged per transect per pair of streamlines at each depth.

6. The eddy heat flux components were streamwise averaged to produce mean along-stream and across-stream components per pair of streamlines and depth. Standard errors were calculated similarly to the time-mean streamwise coordinate system.

6.1.2 Method 2: down-along-transect direction

In contrast to method 1, method 2 uses each transect and the maps of Ψ^* to find unique intersections with open streamlines (Fig. 6.1b). Moving in the down-along-transect direction, it was determined where each transect first intersected a particular open streamline. The same definitions for Ψ^*_j and Ψ^*_{j+1} were used as in method 1. These steps were followed for the binning, rotation and averaging of the eddy heat flux estimates:

1. Moving in the down-along-transects direction (i.e. starting from the northernmost data-position) the first intersection between the transect and the open contour Ψ^*_j and Ψ^*_{j+1} was determined.

2. Velocity and temperature data falling within each pair of intersections were found, and individual eddy heat flux estimates were calculated.

3. Normal vectors were bilinearly interpolated to the eddy heat flux positions.

4. For those positions that were found within closed contours for a specific pair of intersections, every normal vector within the pair of intersections were re-interpolated using the inverse distance weighting method.

5. Individual heat flux estimates were binned and rotated for the pair of streamlines associated with the pair of intersections, to obtain along/across-stream heat flux components.

These steps were repeated for each pair of streamlines per transect and at every depth. Finally, the streamwise rotation and averaging were carried out in the same way as in method 1.

6.1.3 Method 3: up-along-transect direction

Method 3 followed the same steps used in method 2 except moving in the up-along-transect, i.e. unique intersections between open streamlines and each transect were determined by moving from south to north (Fig. 6.1c). Consequently, $\Psi^*_{j=1}$ is the southernmost streamline and $\Psi^*_{j+1} = \Psi^*_j + \Delta\Psi^*$. The methods described above for methods 1 and 2 were used for interpolation and re-interpolation of the normal vector, as well as for the rotation, binning and averaging of the eddy heat flux estimates.

6.1.4 A case study

As an example, we use the pair of open streamlines $\Psi^* = 0.15$ and $\Psi^* = 0.25$ contoured in Figure 6.1a for method 1. Six data points are found inside these open streamlines; half of these data points are also located inside closed contours (dashed lines in Fig. 6.1a). Consequently, the normal vectors $\hat{\mathbf{n}}$ inside the pair of open streamlines were re-interpolated using the normal

vector located outside of the pair $\Psi^* = 0.15$ and $\Psi^* = 0.25$. Subsequently, the re-interpolated normal vectors $\hat{\mathbf{n}}'$ (magenta arrows in Fig. 6.1a) are used to rotate the eddy heat flux estimates into along-stream and across-stream components. These estimates (at locations with magenta arrows in Fig. 6.1a) are then binned and assigned to the average streamline $\Psi^* = 0.20$.

For method 2 (moving in the down-along-transect direction; Fig. 6.1b), multiple intersections are found for the northernmost streamline ($\Psi^* = 0.95$); however, only the first intersection ($x = 0.86$) is counted as the method disregards multiple crossings of the same streamline once the first crossing has been found. Moving down-along the transect, the next intersection for $\Psi^* = 0.85$ is found at $x = 0.65$ and the data between this pair of streamlines are rotated and binned in $\Psi^* = 0.90$. No normal vector re-interpolation is required since the transect does not intersect closed streamlines. Moving further down-along the transect, the first intersection with $\Psi^* = 0.25$ occurs at $x = 0.50$, and we intersect closed contours and $\Psi^* = 0.25$ twice again between $0.20 < x < 0.40$. However, we disregard the duplicate intersections and continue moving down-along the transect until the first intersection with an open $\Psi^* = 0.15$ is found ($x = 0.15$). More data points (8 points with magenta arrows in the area between open streamlines, Fig. 6.1a) are found between these two streamlines than in method 1. Normal vectors between these two streamlines are re-interpolated, and then their corresponding eddy heat flux estimates rotated and binned for the averaged streamline $\Psi^* = 0.20$.

Finally, the normal vector interpolation and re-interpolation and binning using method 3 is illustrated in Figure 6.1c. Moving in the up-along-transect direction, the first intersections with $\Psi^* = 0.15$ and $\Psi^* = 0.25$ are found in $0.15 < x < 0.25$. Only two data points are found inside this pair of intersections, less than the 6 data points found using method 1 and the 8 points found for method 2 for the same pair of open streamlines (Figs. 6.1a,b). These two points are binned to $\Psi^* = 0.20$. Continuing along the transect, repeated intersections for $\Psi^* = 0.25$ and closed contours are neglected until the first intersection with $\Psi^* = 0.35$ is located ($x = 0.55$). Data points between the intersections at $\Psi^* = 0.25$ and $\Psi^* = 0.35$ are re-interpolated and binned

for $\Psi^* = 0.30$ (magenta arrows in Fig. 6.1c). In contrast, the northernmost 4 of these 6 data points are binned for $\Psi^* = 0.20$ in methods 1 and 2 (Figs. 6.1a,b).

In the presence of strong meandering and shifting, method 3 excludes more data points compared to methods 1 and 2 at the northern and southernmost streamlines (Fig. 6.1c). In particular, strong meandering is present for the last pair of streamlines $\Psi^* = 0.85$ and $\Psi^* = 0.95$ (for $x > 0.60$). The meandering results in the first intersection between the transect and $\Psi^* = 0.95$ occurring at $x = 0.65$, thus the last five data points are excluded from the binning and averaging.

6.2 Appendix B

6.2.1 Eddy heat flux estimates for methods 2 and 3

The depth-integrated eddy heat flux components as a function of Ψ^* using methods 2 and 3 are shown in Figure 6.2. The spatial structure of the depth-integrated components is similar for both methods in the southern half of the ACC ($\Psi^* \leq -1.10$ m). The along-stream $\overline{u'T'}_{\Psi^*}$ component shows upstream eddy heat flux south of the PF for both methods. Also, the across-stream component $\overline{v'T'}_{\Psi^*}$ is statistically insignificant south of the PF for both methods, which agrees with the results using the time-mean streamlines and method 1 for the synoptic streamlines (Fig. 2.6). However, the spatial distribution north of the PF exhibits some discrepancies among methods. The along-stream eddy heat flux component in Method 2 is significantly downstream in the southern flank of the SAF and in the PF (Fig. 6.2a). In method 3, significant downstream eddy heat flux is only found in the PF (Fig. 6.2b). Method 2 shows significant maximum poleward eddy heat flux occurs in the SAF with a reduced but still significant amplitude in the PFZ. In contrast, $\overline{v'T'}_{\Psi^*}$ is significant and poleward only in the SAF for method 3. The overall $\overline{v'T'}_{\Psi^*}$ spatial distribution resembles the results from method 1 (Fig. 2.6); the maximum poleward peak is not statistically different among the three methods. Finally, the depth-integrated along-stream $\overline{u'T'}^{\#}_{\Psi^*}$ and across-stream $\overline{v'T'}^{\#}_{\Psi^*}$ eddy heat flux components calculated using methods 2 and 3,

where the $^{\#}$ indicates no re-interpolation of the normal vector when data locations fall within closed contours, are also shown (dashed lines in Fig. 6.2). Clearly, there is little difference in both components using either method when the normal vector is re-interpolated or not.

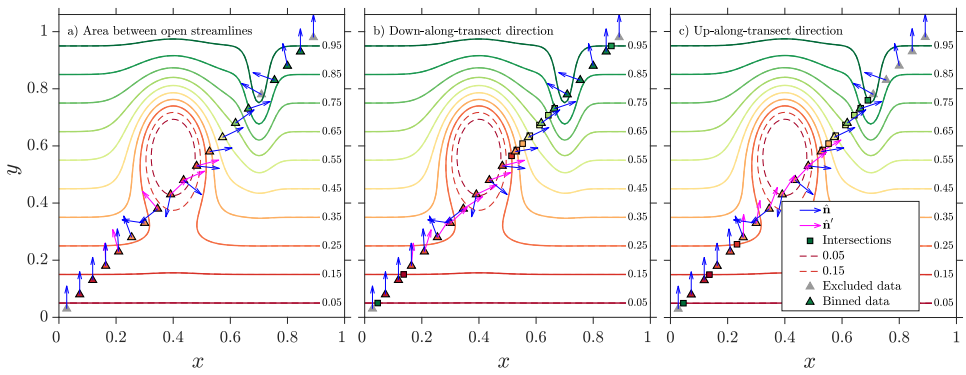

Figure 6.1: Idealized schematics illustrating how data points are binned, and the normal vectors $\hat{\mathbf{n}}$ (blue) are calculated using the inverse weighting method $\hat{\mathbf{n}}'$ (magenta) when data points fall inside closed contours (dashed lines) for a specific pair of open streamlines (solid lines) using (a) method 1 (area between open streamlines), (b) method 2 (down-along-transect direction) and (c) method 3 (up-along-transect direction). Data points are colored according to the same pair of open streamlines. Unique intersections are shown in color-coded □. Data points that fall outside of a pair of streamlines (method 1) or a pair of unique intersections (methods 2 and 3) are excluded from the binning and averaging (gray △).

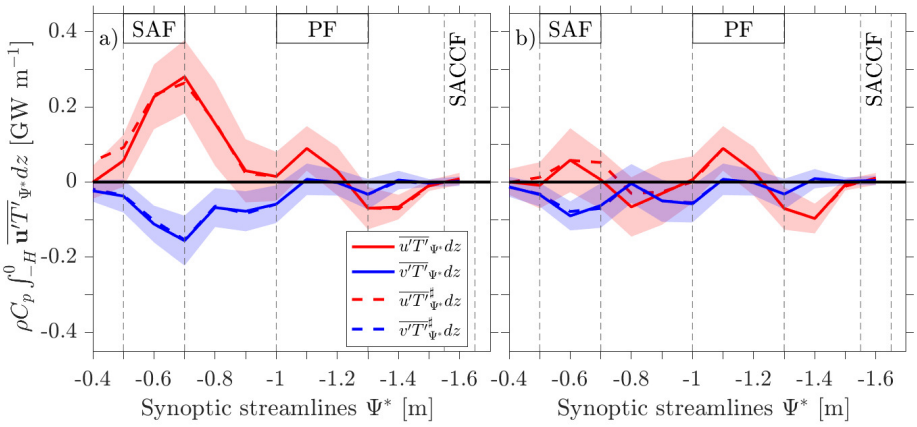

Figure 6.2: Depth-integrated eddy heat flux estimates in the upper 886 m as a function of time-varying (synoptic) geostrophic streamfunction Ψ^* calculated using (a) method 2 (moving in the down-along-transect direction) and (b) method 3 (moving in the up-along-transect direction). Solid red and blue lines show the along-stream $\overline{u'T'}_{\Psi^*}$ and across-stream $\overline{v'T'}_{\Psi^*}$ eddy heat flux components, respectively, when the normal vector is re-interpolated; shaded areas show the standard error. Dashed red and blue lines represent the depth-integrated along-stream $\overline{u'T'}^{\sharp}_{\Psi^*}$ and across-stream $\overline{v'T'}^{\sharp}_{\Psi^*}$ eddy heat flux components, respectively, calculated without re-interpolating the normal vector when eddy heat flux data locations fell within closed contours.

Chapter 7

Appendices for Chapter 3: Turbulent mixing and lee-wave radiation in Drake Passage: sensitivity to topography

7.1 Estimating finescale ε by using a strain-only parameterization

To analyze the sensitivity of the inferred turbulent dissipation rates ε to the choice of parameterization, we used the density (therefore, stratification N^2) profiles to estimate ε by employing the strain-only finescale parameterization [Kunze, 2017]:

$$\varepsilon = \varepsilon_0 \frac{<\xi_z^2>^2}{<\xi_{z\,GM}^2>^2} h(R_\omega) L(f, \overline{N}), \tag{7.1}$$

$$h(R_\omega) = \frac{1}{6\sqrt{2}} \frac{R_\omega(R_\omega+1)}{\sqrt{R_\omega - 1}}, \tag{7.2}$$

$$L(f, \overline{N}) = \frac{f \cosh^{-1}[\overline{N}/f]}{f_{30} \cosh^{-1}[N_0/f_{30}]}, \tag{7.3}$$

where $\varepsilon_0 = 6.37 \times 10^{-10}$ W kg^{-1}, $N_0 = 5.2 \times 10^{-3}$ rad s^{-1}, $V_z^2{}_{GM}/N_0^2$ are the canonical Garrett-Munk dissipation rate, stratification, and buoyancy-normalized shear variance, respectively; $f_{30} = 7.3 \times 10^{-5}$ rad s^{-1} is the inertial frequency at 30° latitude, f is the local Coriolis frequency, and $\overline{N}$ is the mean stratification (details in subsection 3.1 in main manuscript).

The GM model vertical wavenumber spectrum for strain $\xi_z^2{}_{GM}$ is given by

$$\xi_z^2{}_{GM} = \frac{\pi E_0 b}{2} \frac{m^2 j^*}{(m+m^*)^2}, \tag{7.4}$$

where $E_0 = 6.3 \times 10^{-5}$ is the canonical nondimensional spectral energy level, $b = 1300$ m is the stratification length scale, $j^* = 3$ is the peak n-mode number, and $m^* = \frac{\pi j^*/b}{\overline{N}/N_0}$ is the corresponding vertical wavenumber. It is worth noting that the canonical GM shear and strain spectra are related since $V_z^2/N_{0_{GM}}^2 = 3\xi_{z_{GM}}^2$.

To estimate strain-only ε (eq. 7.1), we set $R_\omega = 4$ and calculated GM-normalized strain variance for each 320-m window as in section 3.2. The constant R_ω stems from our analysis in subsection 4.2, where the R_ω remains quasi-constant throughout the sampled water column across Drake Passage (see blue profiles Fig. 5b,d).

Comparisons of ε inferred from using shear-strain parameterization with different limits of integration and using the strain-only parameterization are estimated as means both as a function of height above the bottom and in depth coordinates (Figs. 7.1a-c and 7.2a-c, respectively). Likewise, comparisons for R_ω calculated with different limits are also shown as function of height above the bottom (Fig. 7.1d) and depth (Fig. 7.2d).

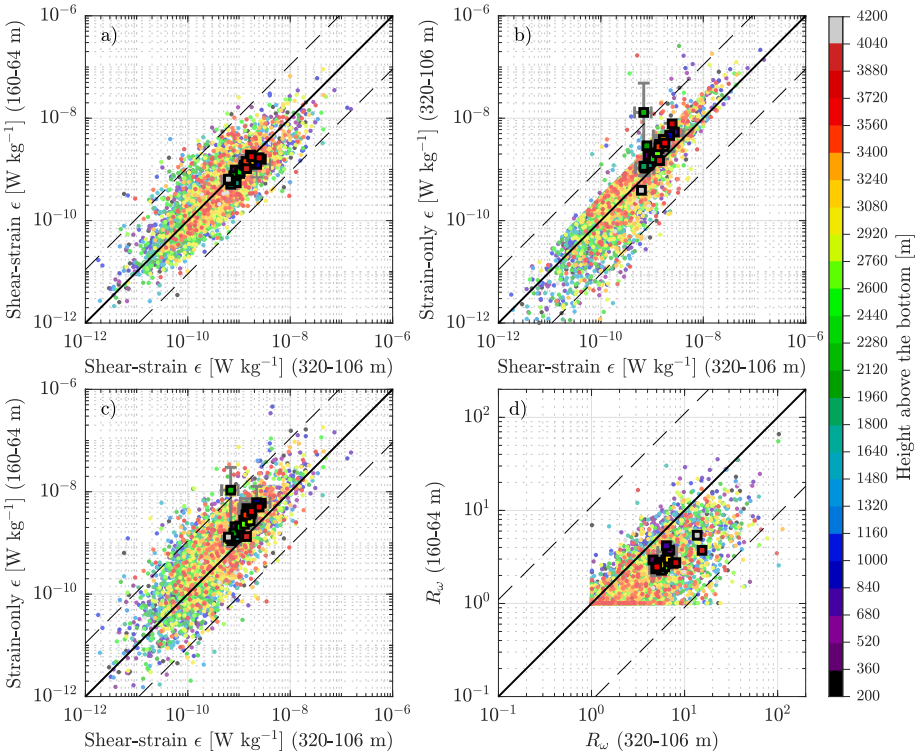

Figure 7.1: Comparison between the finescale dissipation rates of turbulent kinetic energy ε [W kg^{-1}] inferred from using the shear-strain parameterization (with wavelength limits of integration 320-106 m) and those from using the a) shear-strain (with limits 160-64 m), b) strain-only (limits 320-106 m) and c) strain-only (limits 160-64 m). d) Comparison between shear-strain ratio R_ω with limits of integration 320-106 m and 160-64 m. Dots color-coded by height above the bottom represent individual 320-m windows from five cDrake cruises. Filled squares show the mean for each height above the bottom bin; 95% bootstraped confidence intervals are shown in gray error bars at every four height above the bottom bin. Solid black line shows the 1:1 relationship. Dashed gray lines represent the one order of magnitude range.

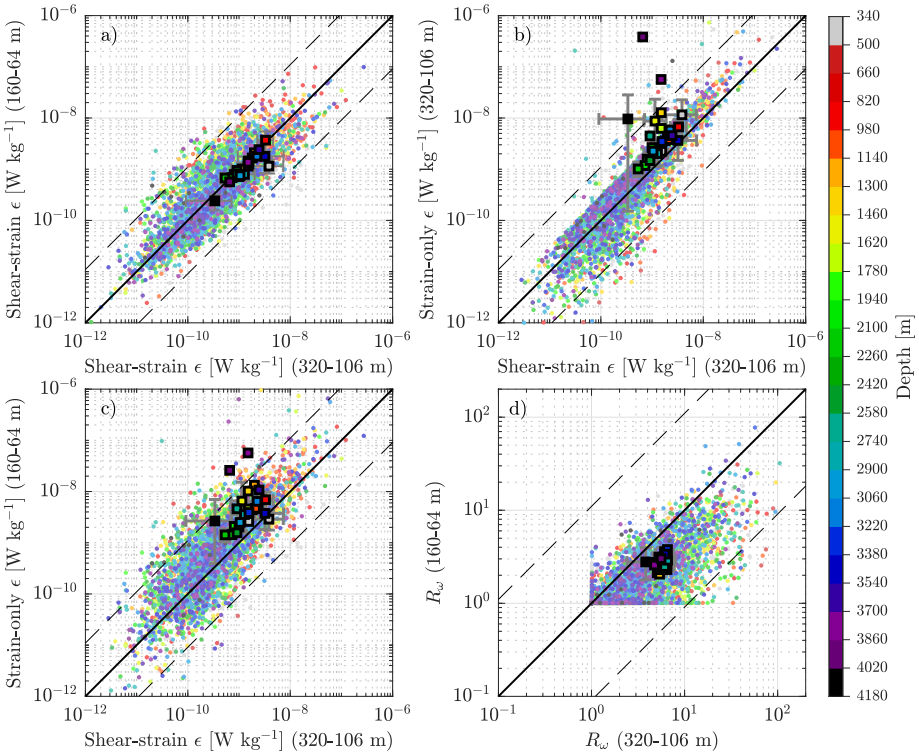

Figure 7.2: Comparison between the finescale dissipation rates of turbulent kinetic energy ε [W kg^{-1}] inferred from using the shear-strain parameterization (with wavelength limits of integration 320-106 m) and those from using the a) shear-strain (with limits 160-64 m), b) strain-only (limits 320-106 m) and c) strain-only (limits 160-64 m). d) Comparison between shear-strain ratio R_ω with limits of integration 320-106 m and 160-64 m. Dots color-coded by depth represent individual 320-m windows from five cDrake cruises. Filled squares show the mean for each depth bin; 95% bootstraped confidence intervals are shown in gray error bars at every four depth bin. Solid black line shows the 1:1 relationship. Dashed gray lines represent the one order of magnitude range.

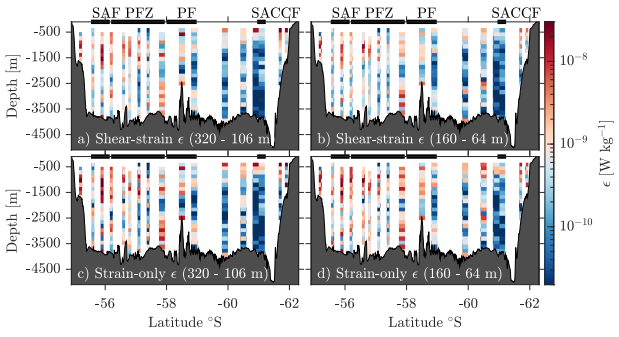

Figure 7.3: Across Drake Passage sections along the cDrake 2010 C-Line of finescale dissipation rates of turbulent kinetic energy ε [W kg^{-1}] using the (a)-(b) shear-strain and (c)-(d) strain-only parameterization. Shear and/or strain limits (wavelengths) of integration used for each section are shown in parenthesis. Dark gray patches show the MB bathymetry. Each profile corresponds to one CTD/LADCP cast. Thick black bars show the mean position of the ACC fronts (Fig. 1).

Table 7.1: Abyssal hill statistical parameters obtained from gravimetric and multibeam echosounder measurements during the full cDrake campaign.

			Gravimetric data (G2020)					Multibeam data (MB)				
	Longitude [° W]	Latitude [° S]	H_{rms} [m]	k_n [km^{-1}]	k_s [km^{-1}]	θ [°]	ν	H_{rms} [m]	k_n [km^{-1}]	k_s [km^{-1}]	θ [°]	ν
A01	-65.08	-57.00	118.05	0.4121	0.0767	18.93	0.95	-	-	-	-	-
A02	-64.92	-57.32	160.37	0.383	0.0924	8.03	0.95	-	-	-	-	-
A03	-64.49	-57.61	261.45	0.3272	0.1081	8.13	0.95	-	-	-	-	-
B01	-64.45	-56.91	148.99	0.3742	0.0928	9.42	0.95	-	-	-	-	-
B02	-64.28	-57.23	226.78	0.3336	0.0936	9.49	0.95	121.48	0.8359	0.2739	23.61	0.89
B03	-63.82	-57.50	177.95	0.2815	0.0866	10.81	0.95	-	-	-	-	-
C04	-64.30	-55.92	182.02	0.1916	0.0729	9.87	0.95	-	-	-	-	-
C05	-64.16	-56.34	183.57	0.2433	0.0811	9.92	0.95	-	-	-	-	-
C06	-63.82	-56.84	126.82	0.3053	0.0731	10.3	0.95	89.26	1.3523	0.2487	22.91	0.89
C07	-63.63	-57.14	127.11	0.2808	0.0733	10.67	0.95	89.26	1.3523	0.2487	22.91	0.89
C08	-63.46	-57.44	121.99	0.2741	0.0743	11.74	0.95	-	-	-	-	-
C09	-63.14	-57.95	194.39	0.318	0.0872	15.60	0.95	-	-	-	-	-
C10	-62.75	-58.50	129.76	0.4148	0.0807	13.67	0.95	75.92	1.8417	0.1634	37.49	0.89
C11	-62.44	-58.99	98.97	0.4252	0.0772	11.05	0.95	180.10	0.5378	0.0980	28.37	0.89
C12	-62.05	-59.59	106.32	0.3742	0.0707	8.41	0.95	-	-	-	-	-
C13	-61.76	-60.09	75.49	0.3818	0.0648	5.30	0.95	54.91	0.6800	0.2077	50.17	0.89
C14	-61.37	-60.60	119.09	0.2971	0.0661	5.30	0.95	45.08	0.5141	0.1700	52.78	0.89
C15	-61.04	-61.11	187.25	0.2715	0.0678	5.30	0.95	89.41	0.6571	0.2024	63.33	0.89
C18	-63.30	-57.69	115.52	0.2842	0.0781	12.96	0.95	-	-	-	-	-
C19	-63.91	-56.69	165.92	0.3001	0.0785	10.12	0.95	113.71	0.7342	0.1475	23.47	0.89
C20	-64.22	-56.13	175.22	0.2087	0.0754	9.94	0.95	-	-	-	-	-
C21	-64.20	-56.21	174.41	0.2177	0.0769	9.93	0.95	-	-	-	-	-
C23	-61.06	-61.02	130.32	0.2802	0.0672	5.30	0.95	-	-	-	-	-
D01	-63.18	-56.72	80.35	0.3062	0.0664	10.83	0.95	-	-	-	-	-
D02	-63.00	-57.03	111.88	0.2921	0.0675	18.85	0.95	-	-	-	-	-
D03	-62.81	-57.35	119.85	0.2758	0.0691	18.37	0.95	112.83	0.7429	0.1738	40.83	0.89
E01	-62.55	-56.63	74.14	0.3455	0.0686	19.93	0.95	-	-	-	-	-
E02	-62.42	-56.95	106.89	0.2931	0.0682	19.40	0.95	-	-	-	-	-
E03	-62.17	-57.25	127.4	0.2699	0.0698	18.82	0.95	-	-	-	-	-
F01	-61.91	-56.53	104.2	0.2714	0.0701	20.48	0.95	-	-	-	-	-
F02	-61.71	-56.85	134.71	0.2392	0.0717	19.94	0.95	-	-	-	-	-
F03	-61.52	-57.17	132.51	0.2368	0.0719	19.38	0.95	-	-	-	-	-
G01	-61.28	-56.44	142.99	0.2279	0.0719	21.05	0.95	-	-	-	-	-
G02	-61.08	-56.76	162.23	0.1962	0.0722	20.54	0.95	-	-	-	-	-
G03	-60.88	-57.07	226.04	0.1738	0.0756	28.01	0.95	-	-	-	-	-
H01	-63.10	-58.44	209.45	0.3822	0.093	11.40	0.95	-	-	-	-	-
H02	-63.05	-58.37	139.58	0.3807	0.093	11.95	0.95	-	-	-	-	-
H03	-63.03	-58.35	192.05	0.374	0.0946	12.48	0.95	-	-	-	-	-
H04	-63.30	-58.28	227.58	0.3484	0.105	12.35	0.95	-	-	-	-	-
H05	-63.40	-58.26	194.79	0.3524	0.1056	11.66	0.95	-	-	-	-	-

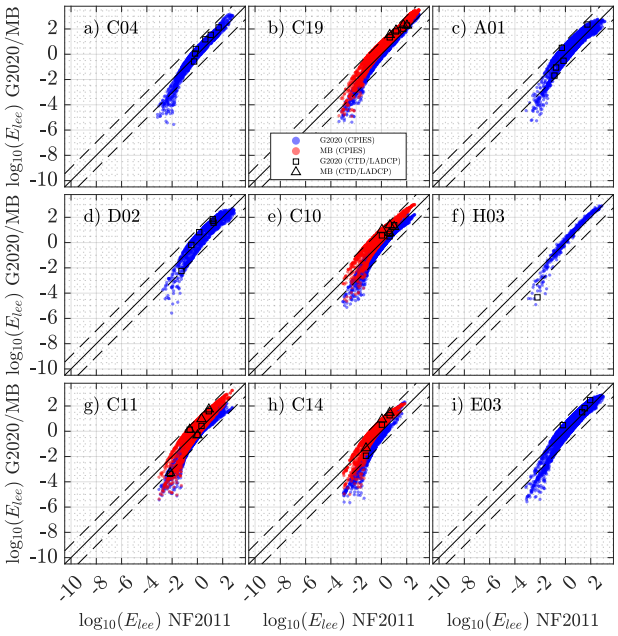

Figure 7.4: Log_{10} lee wave energy radiation (E_{lee}) [mW m^{-2}] calculated using the NF2011 1D isotropic abyssal topography vs $\log_{10}$ lee wave energy radiation calculated using a 2D anisotropic abyssal topography for different CPIES locations (Fig. 1). Filled circles are energy estimates using the CPIES bottom current meters and stratification time series. Blue and red circles indicate that E_{lee} (y axis) was calculated using the G2020 and MB statistical parameters, respectively. Open black squares and triangles are E_{lee} (y axis) calculated using the G2020 and MB statistical parameters, respectively, using the CTD/LADCP stratification and velocity averaged in the 1000 m closest to the bottom. Solid diagonal shows the 1:1 relationship. Dashed diagonals show the one order of magnitude limits.

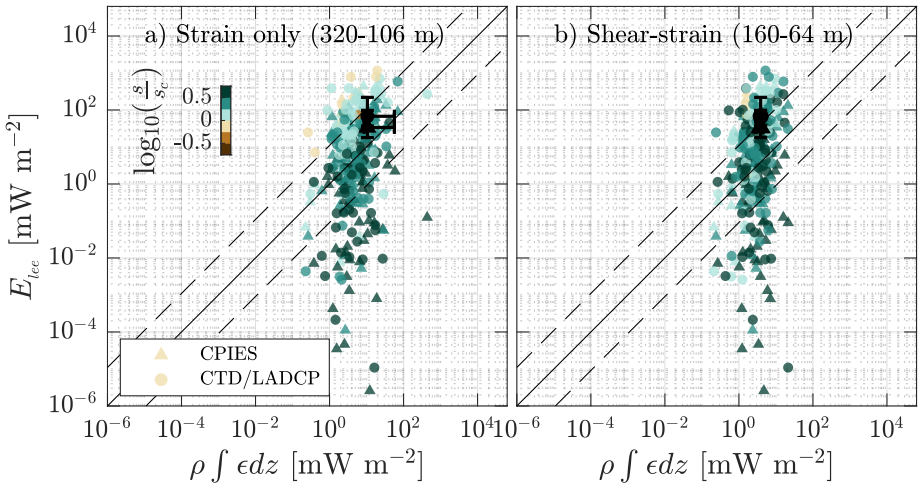

Figure 7.5: Lee-wave energy radiation (E_{lee}) [mW m^{-2}] vs finescale turbulent kinetic energy dissipation ε integrated from the bottom to the base of the mixed layer in Drake Passage [mW m^{-2}] using the (a) strain-only and (b) shear-strain parameterization. Lee-wave energy radiation is calculated using the G2020 topography. Wavelengths limits of integration for shear and strain are indicated in parenthesis. Filled circles show the energy radiation estimated using the CPIES near-bottom current meter and stratification closest in time to the CTD/LADCP cast. Colorbar shows the $\log_{10}(\frac{s}{s_c})$. CTD/LADCP-based energy estimates are shown in colored filled triangles. Mean and bootstrapped 95% confidence limits for both CPIES and CTD/LADCP-based estimates are shown in black symbols (filled circles and triangles, respectively), and vertical and horizontal bars. Solid diagonal shows the 1:1 relationship. Dashed diagonals show the one order of magnitude limits.

References

Abernathey, R. and Cessi, P. (2014). Topographic enhancement of eddy efficiency in baroclinic equilibration. *J. Phys. Oceanogr.* 44: 2107–2126, doi: 10.1175/JPO-D-14-0014.1.

Auger, M., Morrow, R., Kestenare, E., Sallée, J.-B. and Cowley, R. (2021). Southern Ocean in-situ temperature trends over 25 years emerge from interannual variability. *Nat. Communic.* 12: 1–9, doi: https://doi.org/10.1038/s41467-021-22318-6.

Baker, L. and Mashayek, A. (2021). Surface reflection of bottom generated oceanic lee waves. *J. Fluid Mech.* 924: A17, doi: 10.1017/jfm.2021.627.

Barthel, A., McC. Hogg, A., Waterman, S. and Keating, S. (2017). Jet–topography interactions affect energy pathways to the deep Southern Ocean. *J. Phys. Oceanogr.* 47: 1799–1816, doi: 10.1175/JPO-D-16-0220.1.

Bell Jr, T. (1975). Topographically generated internal waves in the open ocean. *J. Geophys. Res.* 80: 320–327, doi: https://doi.org/10.1029/JC080i003p00320.

Bindoff, N. L. and McDougall, T. J. (1994). Diagnosing climate change and ocean ventilation using hydrographic data. *J. Phys. Oceanogr.* 24: 1137–1152, doi: doi.org/10.1175/1520-0485(1994)024⟨1137:DCCAOV⟩2.0.CO;2.

Bishop, S. P., Watts, D. R. and Donohue, K. A. (2013). Divergent eddy heat fluxes in the Kuroshio extension at 144–148 E. Part I: Mean structure. *J. Phys. Oceanogr.* 43: 1533–1550, doi: 10.1175/JPO-D-12-0221.1.

Böning, C. W., Dispert, A., Visbeck, M., Rintoul, S. and Schwarzkopf, F. U. (2008). The response of the Antarctic Circumpolar Current to recent climate change. *Nature Geosc.* 1: 864, doi: 10.1038/ngeo362.

Boyer Montégut, C. de, Madec, G., Fischer, A. S., Lazar, A. and Iudicone, D. (2004). Mixed layer depth over the global ocean: An examination of profile data and a profile-based climatology. *J. Geophys. Res. Oceans* 109, doi: https://doi.org/10.1029/2004JC002378.

Brearley, J. A., Sheen, K. L., Naveira Garabato, A. C., Smeed, D. A., Speer, K. G., Thurnherr, A. M., Meredith, M. P. and Waterman, S. (2014). Deep boundary current disintegration in Drake

Passage. *Geophys. Res. Lett.* 41: 121–127, doi: https://doi.org/10.1002/2013GL058617.

Brearley, J. A., Sheen, K. L., Naveira Garabato, A. C., Smeed, D. A. and Waterman, S. (2013). Eddy-induced modulation of turbulent dissipation over rough topography in the Southern Ocean. *J. Phys. Oceanogr.* 43: 2288–2308, doi: 10.1175/JPO-D-12-0222.1.

Bryden, H. L. (1979). Poleward heat flux and conversion of available potential energy in Drake Passage. *J. Mar. Res.* 37: 1–22.

Cairns, J. L. and Williams, G. O. (1976). Internal wave observations from a midwater float, 2. *J. Geophys. Res.* 81: 1943–1950, doi: https://doi.org/10.1029/JC081i012p01943.

Chapman, C. and Sallée, J.-B. (2017). Can we reconstruct mean and eddy fluxes from Argo floats? *Ocean Modell.* 120: 83–100, doi: 10.1016/j.ocemod.2017.10.004.

Chelton, D. B., deSzoeke, R. A., Schlax, M. G., El Naggar, K. and Siwertz, N. (1998). Geographical variability of the first baroclinic Rossby radius of deformation. *J. Phys. Oceanogr.* 28: 433–460, doi: 10.1175/1520-0485(1998)028⟨0433:GVOTFB⟩2.0.CO;2.

Chereskin, T., Donohue, K., Watts, D., Tracey, K., Firing, Y. and Cutting, A. (2009). Strong bottom currents and cyclogenesis in Drake Passage. *Geophys. Res. Lett.* 36, doi: 10.1029/2009GL040940.

Chereskin, T. K., A, K. A. D., Watts, D. R., Tracey, K. L., Firing, Y. L. and Cutting, A. L. (2012). cDrake: Dynamics and transport of the Antarctic Circumpolar Current in Drake Passage. *Oceanography* 25: 134–135, doi: 10.5670/oceanog.2012.86.

Chidichimo, M. P., Donohue, K. A., Watts, D. R. and Tracey, K. L. (2014). Baroclinic transport time series of the Antarctic Circumpolar Current measured in Drake Passage. *J. Phys. Oceanogr.* 44: 1829–1853, doi: https://doi.org/10.1175/JPO-D-13-071.1.

Colin de Verdière, A. and Ollitrault, M. (2016). A Direct Determination of the World Ocean Barotropic Circulation. *J. Phys. Oceanogr.* 46: 255 – 273, doi: 10.1175/JPO-D-15-0046.1.

Cronin, M. and Watts, D. R. (1996). Eddy–mean flow interaction in the Gulf Stream at 68 W. Part I: Eddy energetics. *J. Phys. Oceanogr.* 26: 2107–2131, doi: 10.1175/1520-0485(1996)026⟨2107:AEFIITG⟩2.0.CO;2.

Cunningham, S. A., Alderson, S. G., King, B. A. and Brandon, M. A. (2003). Transport and variability of the Antarctic Circumpolar Current in Drake Passage. *J. Geophys. Res. Oceans* 108, doi: https://doi.org/10.1029/2001JC001147.

Cusack, J. M., Naveira Garabato, A. C., Smeed, D. A. and Girton, J. B. (2017). Observation of a large lee wave in the Drake Passage. *J. Phys. Oceanogr.* 47: 793–810, doi: https://doi.org/10.1175/JPO-D-16-0153.1.

Dong, S., Gille, S. T. and Sprintall, J. (2007). An assessment of the Southern Ocean mixed layer heat budget. *J. Clim.* 20: 4425–4442, doi: 10.1175/JCLI4259.1.

Donohue, K. A., Tracey, K. L., Watts, D. R., Chidichimo, M. P. and Chereskin, T. K. (2016). Mean Antarctic Circumpolar Current transport measured in Drake Passage. *Geophys. Res. Lett.* 43: 11,760–11,767, doi: https://doi.org/10.1002/2016GL070319.

Ducet, N., Le Traon, P.-Y. and Reverdin, G. (2000). Global high-resolution mapping of ocean circulation from TOPEX/Poseidon and ERS-1 and-2. *J. Geophys. Res.* 105: 19477–19498, doi: 10.1029/2000JC900063.

Durack, P. J. and Wijffels, S. E. (2010). Fifty-Year Trends in Global Ocean Salinities and Their Relationship to Broad-Scale Warming. *J. Clim.* 23: 4342 – 4362, doi: 10.1175/2010JCLI3377.1.

Egbert, G. D., Bennett, A. F. and Foreman, M. G. (1994). TOPEX/Poseidon tides estimated using a global inverse model. *J. Geophys. Res.* 99: 24821–24852, doi: 10.1029/94JC01894.

Farneti, R., Delworth, T. L., Rosati, A. J., Griffies, S. M. and Zeng, F. (2010). The Role of Mesoscale Eddies in the Rectification of the Southern Ocean Response to Climate Change. *J. Phys. Oceanogr.* 40: 1539 – 1557, doi: 10.1175/2010JPO4353.1.

Fay, A. R., McKinley, G. A. and Lovenduski, N. S. (2014). Southern Ocean carbon trends: Sensitivity to methods. *Geophys. Res. Lett.* 41: 6833–6840, doi: http://dx.doi.org/10.1002/2014GL061324.

Ferrari, R., Provost, C., Park, Y.-H., Sennéchael, N., Koenig, Z., Sekma, H., Garric, G. and Bourdallé-Badie, R. (2014). Heat fluxes across the Antarctic Circumpolar Current in Drake Passage: Mean flow and eddy contributions. *J. Geophys. Res. Oceans* 119: 6381–6402, doi: 10.1002/2014JC010201.

Firing, E., Hummon, J. M. and Chereskin, T. K. (2012). Improving the quality and accessibility of current profile measurements in the Southern Ocean. *Oceanography* 25: 164–165, doi: 10.5670/oceanog.2012.91.

Firing, Y., Chereskin, T., Watts, D., Tracey, K. and Provost, C. (2014). Computation of geostrophic streamfunction, its derivatives, and error estimates from an array of CPIES in Drake Passage. *J. Atmos. Oceanic Technol.* 31: 656–680, doi: 10.1175/JTECH-D-13-00142.1.

Firing, Y. L., Chereskin, T. K. and Mazloff, M. R. (2011). Vertical structure and transport of the Antarctic Circumpolar Current in Drake Passage from direct velocity observations. *J. Geophys. Res.* 116, doi: 10.1029/2011JC006999.

Firing, Y. L., Chereskin, T. K., Watts, D. R. and Mazloff, M. R. (2016). Bottom pressure torque and the vorticity balance from observations in Drake Passage. *J. Geophys. Res. Oceans* 121: 4282–4302, doi: 10.1002/2016JC011682.

Fogt, R. L. and Bromwich, D. H. (2006). Decadal variability of the ENSO teleconnection to the high-latitude South Pacific governed by coupling with the southern annular mode. *J. Clim.* 19: 979–997, doi: 10.1175/JCLI3671.1.

Fogt, R. L. and Marshall, G. J. (2020). The Southern Annular Mode: Variability, trends, and climate impacts across the Southern Hemisphere. *WIREs Clim. Chg.* 11: e652, doi: https://doi.org/10.1002/wcc.652.

Foppert, A. (2019). Observed storm track dynamics in Drake Passage. *J. Phys. Oceanogr.* 49: 867–884, doi: 10.1175/JPO-D-18-0150.1.

Foppert, A., Donohue, K. A. and Watts, D. R. (2016). The Polar Front in Drake Passage: A composite-mean stream-coordinate view. *J. Geophys. Res. Oceans* 121: 1771–1788, doi: 10.1002/2015JC011333.

Foppert, A., Donohue, K. A., Watts, D. R. and Tracey, K. L. (2017). Eddy heat flux across the Antarctic Circumpolar Current estimated from sea surface height standard deviation. *J. Geophys. Res. Oceans* 122: 6947–6964, doi: 10.1002/2017JC012837.

Frants, M., Damerell, G. M., Gille, S. T., Heywood, K. J., MacKinnon, J. and Sprintall, J. (2013). An assessment of density-based finescale methods for estimating diapycnal diffusivity in the

Southern Ocean. *J. Atmos. Oceanic Tech.* 30: 2647–2661, doi: 10.1175/JTECH-D-12-00241.1.

Freeman, N. M., Munro, D. R., Sprintall, J., Mazloff, M. R., Purkey, S., Rosso, I., DeRanek, C. A. and Sweeney, C. (2019). The observed seasonal cycle of macronutrients in Drake Passage: relationship to fronts and utility as a model metric. *J. Geophys. Res. Oceans* 124: 4763–4783, doi: 10.1029/2019JC015052.

Garabato, A. C. N., Polzin, K. L., King, B. A., Heywood, K. J. and Visbeck, M. (2004). Widespread intense turbulent mixing in the Southern Ocean. *Science* 303: 210–213, doi: 10.1126/science.1090929.

Gargett, A. E. (1990). Do we really know how to scale the turbulent kinetic energy dissipation rate ε due to breaking of oceanic internal waves? *J. Geophys. Res. Oceans* 95: 15971–15974, doi: https://doi.org/10.1029/JC095iC09p15971.

Gille, S. T. (2002). Warming of the Southern Ocean since the 1950s. *Science* 295: 1275–1277, doi: 10.1126/science.1065863.

Gille, S. T. (2003). Float observations of the Southern Ocean. Part II: Eddy fluxes. *J. Phys. Oceanogr.* 33: 1182–1196, doi: 10.1175/1520-0485(2003)033⟨1182:FOOTSO⟩2.0.CO;2.

Gille, S. T. (2008). Decadal-Scale Temperature Trends in the Southern Hemisphere Ocean. *J. Clim.* 21: 4749 – 4765, doi: 10.1175/2008JCLI2131.1.

Gille, S. T., Lombrozo, A., Sprintall, J., Stephenson, G. and Scarlet, R. (2009). Anomalous spiking in spectra of XCTD temperature profiles. *J. Atmos. Ocean. Tech.* 26: 1157–1164, doi: https://doi.org/10.1175/2009JTECHO668.1.

Goff, J. A. (2010). Global prediction of abyssal hill root-mean-square heights from small-scale altimetric gravity variability. *J. Geophys. Res. Solid Earth* 115, doi: https://doi.org/10.1029/2010JB007867.

Goff, J. A. (2020). Identifying characteristic and anomalous mantle from the complex relationship between abyssal hill roughness and spreading rates. *Geophy. Res. Lett.* 47: e2020GL088162, doi: https://doi.org/10.1029/2020GL088162.

Goff, J. A. and Jordan, T. H. (1988). Stochastic modeling of seafloor morphology: Inversion of sea beam data for second-order statistics. *J. Geophys. Res. Solid Earth* 93: 13589–13608, doi: https://doi.org/10.1029/JB093iB11p13589.

Griesel, A., Mazloff, M. R. and Gille, S. T. (2012). Mean dynamic topography in the Southern Ocean: Evaluating Antarctic Circumpolar Current transport. *J. Geophys. Res. Oceans* 117, doi: https://doi.org/10.1029/2011JC007573.

Gutierrez-Villanueva, M. O., Chereskin, T. K. and Sprintall, J. (2020). Upper-ocean eddy heat flux across the Antarctic Circumpolar Current in Drake Passage from observations: time-mean and seasonal variability. *J. Phys. Oceanogr.* 50: 2507–2527, doi: 10.1175/JPO-D-19-0266.1.

Gutierrez-Villanueva, M. O., Chereskin, T. K., Sprintall, J. and Goff, J. A. (2022). Turbulent Mixing and Lee-Wave Radiation in Drake Passage: Sensitivity to Topography. *J. Geophys. Res. Oceans* 127: e2021JC018103, doi: https://doi.org/10.1029/2021JC018103.

Hall, A. and Visbeck, M. (2002). Synchronous Variability in the Southern Hemisphere Atmosphere, Sea Ice, and Ocean Resulting from the Annular Mode. *J. Clim.* 15: 3043–3057, doi: 10.2307/26249474.

Hallberg, R. and Gnanadesikan, A. (2001). An Exploration of the Role of Transient Eddies in Determining the Transport of a Zonally Reentrant Current. *J. Phys. Oceanogr.* 31: 3312 – 3330, doi: 10.1175/1520-0485(2001)031⟨3312:AEOTRO⟩2.0.CO;2.

Hamed, K. H. and Rao, A. R. (1998). A modified Mann-Kendall trend test for autocorrelated data. *J. Hydr.* 204: 182–196, doi: https://doi.org/10.1016/S0022-1694(97)00125-X.

Hanawa, K., Rual, P., Bailey, R., Sy, A. and Szabados, M. (1995). A new depth-time equation for Sippican or TSK T-7, T-6 and T-4 expendable bathythermographs (XBT). *Deep–Sea Res. I.* 42: 1423–1451, doi: 10.1016/0967-0637(95)97154-Z.

Hersbach, H., Bell, B., Berrisford, P., Hirahara, S., Horányi, A., Muñoz-Sabater, J., Nicolas, J., Peubey, C., Radu, R., Schepers, D., Simmons, A., Soci, C., Abdalla, S., Abellan, X., Balsamo, G., Bechtold, P., Biavati, G., Bidlot, J., Bonavita, M., De Chiara, G., Dahlgren, P., Dee, D., Diamantakis, M., Dragani, R., Flemming, J., Forbes, R., Fuentes, M., Geer, A., Haimberger, L., Healy, S., Hogan, R. J., Hólm, E., Janisková, M., Keeley, S., Laloyaux, P., Lopez, P., Lupu, C., Radnoti, G., Rosnay, P. de, Rozum, I., Vamborg, F., Villaume, S. and Thépaut, J.-

N. (2020). The ERA5 global reanalysis. *Q. J. R. Meteorol. Soc.* 146: 1999–2049, doi: https://doi.org/10.1002/qj.3803.

Hogg, A. M. (2010). An Antarctic Circumpolar Current driven by surface buoyancy forcing. *Geophys. Res. Letts.* 37, doi: https://doi.org/10.1029/2010GL044777.

Jackett, D. R. and McDougall, T. J. (1997). A Neutral Density Variable for the World's Oceans. *J. Phys. Oceanogr.* 27: 237 – 263, doi: 10.1175/1520-0485(1997)027⟨0237:ANDVFT⟩2.0.CO;2.

Kilbourne, B. F. and Girton, J. B. (2015). Quantifying high-frequency wind energy flux into near-inertial motions in the southeast Pacific. *J. Phys. Oceanogr.* 45: 369–386, doi: 10.1175/JPO-D-14-0076.1.

Kim, Y. S. and Orsi, A. H. (2014). On the variability of Antarctic Circumpolar Current fronts inferred from 1992–2011 altimetry. *J. Phys. Oceanogr.* 44: 3054–3071, doi: 10.1175/JPO-D-13-0217.1.

Klymak, J. M. (2018). Nonpropagating form drag and turbulence due to stratified flow over large-scale abyssal hill topography. *J. Phys. Oceanogr.* 48: 2383–2395, doi: https://doi.org/10.1175/JPO-D-17-0225.1.

Klymak, J. M., Balwada, D., Garabato, A. N. and Abernathey, R. (2021). Parameterizing Nonpropagating Form Drag over Rough Bathymetry. *J. Phys. Oceanogr.* 51: 1489–1501, doi: https://doi.org/10.1175/JPO-D-20-0112.1.

Koenig, Z., Provost, C., Ferrari, R., Sennéchael, N. and Rio, M.-H. (2014). Volume transport of the Antarctic Circumpolar Current: Production and validation of a 20 year long time series obtained from in situ and satellite observations. *J. Geophys. Res. Oceans* 119: 5407–5433, doi: https://doi.org/10.1002/2014JC009966.

Kunze, E. (1985). Near-inertial wave propagation in geostrophic shear. *J. Phys. Oceanogr.* 15: 544–565, doi: 10.1175/1520-0485(1985)015⟨0544:NIWPIG⟩2.0.CO;2.

Kunze, E. (2017). Internal-wave-driven mixing: Global geography and budgets. *J. Phys. Oceanogr.* 47: 1325–1345, doi: 10.1175/JPO-D-16-0141.1.

Kunze, E., Firing, E., Hummon, J. M., Chereskin, T. K. and Thurnherr, A. M. (2006). Global abyssal mixing inferred from lowered ADCP shear and CTD strain profiles. *J. Phys. Oceanogr.* 36: 1553–1576, doi: 10.1175/JPO2926.1.

Kunze, E. and Lien, R.-C. (2019). Energy sinks for lee waves in shear flow. *J. Phys. Oceanogr.* 49: 2851–2865, doi: 10.1175/JPO-D-19-0052.1.

Ledwell, J. R., St. Laurent, L. C., Girton, J. B. and Toole, J. M. (2011). Diapycnal mixing in the Antarctic Circumpolar Current. *J. Phys. Oceanogr.* 41: 241–246, doi: 10.1175/2010JPO4557.1.

Lenn, Y.-D., Chereskin, T., Sprintall, J. and Firing, E. (2007). Mean jets, mesoscale variability and eddy momentum fluxes in the surface layer of the Antarctic Circumpolar Current in Drake Passage. *J. Mar. Res.* 65: 27–58, doi: 10.1357/002224007780388694.

Lenn, Y.-D. and Chereskin, T. K. (2009). Observations of Ekman Currents in the Southern Ocean. *J. Phys. Oceanogr.* 39: 768 – 779, doi: 10.1175/2008JPO3943.1.

Lenn, Y.-D., Chereskin, T. K. and Sprintall, J. (2008). Improving estimates of the Antarctic Circumpolar Current streamlines in Drake Passage. *J. Phys. Oceanogr.* 38: 1000–1010, doi: 10.1175/2007JPO3834.1.

Lenn, Y.-D., Chereskin, T. K., Sprintall, J. and McClean, J. L. (2011). Near-surface eddy heat and momentum fluxes in the Antarctic Circumpolar Current in Drake Passage. *J. Phys. Oceanogr.* 41: 1385–1407, doi: 10.1175/JPO-D-10-05017.1.

Marshall, G. J. (2003). Trends in the Southern Annular Mode from Observations and Reanalyses. *J. Clim.* 16: 4134 – 4143, doi: 10.1175/1520-0442(2003)016⟨4134:TITSAM⟩2.0.CO;2.

Marshall, J. and Radko, T. (2003). Residual-mean solutions for the Antarctic Circumpolar Current and its associated overturning circulation. *J. Phys. Oceanogr.* 33: 2341–2354, doi: 10.1175/1520-0485(2003)033⟨2341:RSFTAC⟩2.0.CO;2.

Marshall, J. and Shutts, G. (1981). A note on rotational and divergent eddy fluxes. *J. Phys. Oceanogr.* 11: 1677–1680, doi: 10.1175/1520-0485(1981)011⟨1677:ANORAD⟩2.0.CO;2.

Maximenko, N., Niiler, P., Centurioni, L., Rio, M.-H., Melnichenko, O., Chambers, D., Zlotnicki,

V. and Galperin, B. (2009). Mean dynamic topography of the ocean derived from satellite and drifting buoy data using three different techniques. *J. Atmos. Oceanic Technol.* 26: 1910–1919, doi: 10.1175/JPO-D-10-05017.1.

Mazloff, M. R., Heimbach, P. and Wunsch, C. (2010). An Eddy-Permitting Southern Ocean State Estimate. *J. Phys. Oceanogr.* 40: 880 – 899, doi: 10.1175/2009JPO4236.1.

Meehl, G. A., Arblaster, J. M., Chung, C. T., Holland, M. M., DuVivier, A., Thompson, L., Yang, D. and Bitz, C. M. (2019). Sustained ocean changes contributed to sudden Antarctic sea ice retreat in late 2016. *Nat. Communic.* 10: 1–9, doi: 10.1038/s41467-018-07865-9.

Meredith, M. P. and Hogg, A. M. (2006). Circumpolar response of Southern Ocean eddy activity to a change in the Southern Annular Mode. *Geophys. Res. Lett.* 33: L16608, doi: https://doi.org/10.1029/2006GL026499.

Meredith, M. P., Woodworth, P. L., Chereskin, T. K., Marshall, D. P., Allison, L. C., Bigg, G. R., Donohue, K., Heywood, K. J., Hughes, C. W., Hibbert, A. et al. (2011). Sustained monitoring of the Southern Ocean at Drake Passage: Past achievements and future priorities. *Rev. Geophys.* 49, doi: 10.1029/2010RG000348.

Meyer, A., Sloyan, B. M., Polzin, K. L., Phillips, H. E. and Bindoff, N. L. (2015). Mixing variability in the Southern Ocean. *J. Phys. Oceanogr.* 45: 966–987, doi: 10.1175/JPO-D-14-0110.1.

Morrison, A. K., Frölicher, T. L. and Sarmiento, J. L. (2015). Upwelling in the Southern Ocean. *Physics Today* 68: 27.

Naveira Garabato, A. C., Nurser, A. G., Scott, R. B. and Goff, J. A. (2013). The impact of small-scale topography on the dynamical balance of the ocean. *J. Phys. Oceanogr.* 43: 647–668, doi: 10.1175/JPO-D-12-056.1.

Nikurashin, M. and Ferrari, R. (2010a). Radiation and dissipation of internal waves generated by geostrophic motions impinging on small-scale topography: Application to the Southern Ocean. *J. Phys. Oceanogr.* 40: 2025–2042, doi: 10.1175/2010JPO4315.1.

Nikurashin, M. and Ferrari, R. (2010b). Radiation and dissipation of internal waves generated by geostrophic motions impinging on small-scale topography: Theory. *J. Phys. Oceanogr.* 40:

1055–1074, doi: 10.1175/2009JPO4199.1.

Nikurashin, M. and Ferrari, R. (2011). Global energy conversion rate from geostrophic flows into internal lee waves in the deep ocean. *Geophys. Res. Lett.* 38, doi: https://doi.org/10.1029/2011GL046576.

Nikurashin, M. and Ferrari, R. (2013). Overturning circulation driven by breaking internal waves in the deep ocean. *Geophys. Res. Lett.* 40: 3133–3137, doi: https://doi.org/10.1002/grl.50542.

Nikurashin, M., Ferrari, R., Grisouard, N. and Polzin, K. (2014). The impact of finite-amplitude bottom topography on internal wave generation in the Southern Ocean. *J. Phys. Oceanogr.* 44: 2938–2950, doi: 10.1175/JPO-D-13-0201.1.

Nowlin Jr., W. D., Worley, S. J. and Whitworth III, T. (1985). Methods for making point estimates of eddy heat flux as applied to the Antarctic Circumpolar Current. *J. Geophys. Res.* 90: 3305–3324, doi: 10.1029/JC090iC02p03305.

Orsi, A. H., Whitworth III, T. and Nowlin Jr, W. D. (1995). On the meridional extent and fronts of the Antarctic Circumpolar Current. *Deep–Sea Res. I.* 42: 641–673, doi: 10.1016/0967-0637(95)00021-W.

Palóczy, A., Gille, S. T. and McClean, J. L. (2018). Oceanic Heat Delivery to the Antarctic Continental Shelf: Large-Scale, Low-Frequency Variability. *J. Geophys. Res. Oceans* 123: 7678–7701, doi: https://doi.org/10.1029/2018JC014345.

Patara, L., Böning, C. W. and Biastoch, A. (2016). Variability and trends in Southern Ocean eddy activity in 1/12° ocean model simulations. *Geophys. Res. Lett.* 43: 4517–4523, doi: https://doi.org/10.1002/2016GL069026.

Peña-Molino, B., Rintoul, S. and Mazloff, M. (2014). Barotropic and baroclinic contributions to along-stream and across-stream transport in the Antarctic Circumpolar Current. *J. Geophys. Res. Oceans* 119: 8011–8028, doi: 10.1002/2014JC010020.

Phillips, H. E. and Rintoul, S. R. (2000). Eddy variability and energetics from direct current measurements in the Antarctic Circumpolar Current south of Australia. *J. Phys. Oceanogr.* 30: 3050–3076, doi: 10.1175/1520-0485(2000)030⟨3050:EVAEFD⟩2.0.CO;2.

Polzin, K., Garabato, A. C. N., Huussen, T. N., Sloyan, B. M. and Waterman, S. (2014). Finescale parameterizations of turbulent dissipation. *J. Geophys. Res. Oceans* 119: 1383–1419, doi: https://doi.org/10.1002/2013JC008979.

Polzin, K., Kunze, E., Hummon, J. and Firing, E. (2002). The finescale response of lowered ADCP velocity profiles. *J. Atmos. Oceanic Tech.* 19: 205–224, doi: 10.1175/1520-0426(2002)019⟨0205:TFROLA⟩2.0.CO;2.

Renault, L., McWilliams, J. C. and Masson, S. (2017). Satellite observations of imprint of oceanic current on wind stress by air-sea coupling. *Sci. Rep.* 7: 17747, doi: 10.1038/s41598-017-17939-1.

Rintoul, S. R. (2018). The global influence of localized dynamics in the Southern Ocean. *Nature* 558: 209–218, doi: https://doi.org/10.1038/s41586-018-0182-3.

Rio, M.-H. and Hernandez, F. (2004). A mean dynamic topography computed over the world ocean from altimetry, in situ measurements, and a geoid model. *J. Geophys. Res.* 109, doi: 10.1175/JPO-D-10-05017.1.

Rocha, C. B., Chereskin, T. K., Gille, S. T. and Menemenlis, D. (2016). Mesoscale to submesoscale wavenumber spectra in Drake Passage. *J. Phys. Oceanogr.* 46: 601–620, doi: 10.1175/JPO-D-15-0087.1.

Roemmich, D. and Gilson, J. (2009). The 2004–2008 mean and annual cycle of temperature, salinity, and steric height in the global ocean from the Argo Program. *Prog. Oceanogr.* 82: 81–100, doi: 10.1016/j.pocean.2009.03.004.

Ryan, W. B., Carbotte, S. M., Coplan, J. O., O'Hara, S., Melkonian, A., Arko, R., Weissel, R. A., Ferrini, V., Goodwillie, A., Nitsche, F. et al. (2009). Global multi-resolution topography synthesis. *Geochemistry, Geophysics, Geosystems* 10, doi: https://doi.org/10.1029/2008GC002332.

Scott, R., Goff, J., Naveira Garabato, A. and Nurser, A. (2011). Global rate and spectral characteristics of internal gravity wave generation by geostrophic flow over topography. *J. Geophys. Res. Oceans* 116, doi: https://doi.org/10.1029/2011JC007005.

Sekma, H., Park, Y.-H. and Vivier, F. (2013). Time-mean flow as the prevailing contribution to the poleward heat flux across the southern flank of the Antarctic Circumpolar Current: A case study in the Fawn Trough, Kerguelen Plateau. *J. Phys. Oceanogr.* 43: 583–601, doi: 10.1175/

JPO-D-12-0125.1.

Sen, P. K. (1968). Estimates of the regression coefficient based on kendall's tau. *Journal of the American statistical association* 63: 1379–1389, doi: 10.1080/01621459.1968.10480934.

Shakespeare, C. J. (2020). Interdependence of Internal Tide and Lee Wave Generation at Abyssal Hills: Global Calculations. *J. Phys. Oceanogr.* 50: 655–677, doi: 10.1175/JPO-D-19-0179.1.

Sheen, K., Brearley, J., Garabato, A. N., Smeed, D., Laurent, L. S., Meredith, M., Thurnherr, A. and Waterman, S. (2015). Modification of turbulent dissipation rates by a deep Southern Ocean eddy. *Geophys. Res. Lett.* 42: 3450–3457, doi: https://doi.org/10.1002/2015GL063216.

Sheen, K., Brearley, J., Naveira Garabato, A. C., Smeed, D., Waterman, S., Ledwell, J. R., Meredith, M. P., St. Laurent, L., Thurnherr, A. M., Toole, J. M. et al. (2013). Rates and mechanisms of turbulent dissipation and mixing in the Southern Ocean: Results from the Diapycnal and Isopycnal Mixing Experiment in the Southern Ocean (DIMES). *J. Geophys. Res. Oceans* 118: 2774–2792, doi: https://doi.org/10.1002/jgrc.20217.

Sheen, K., Garabato, A. N., Brearley, J., Meredith, M., Polzin, K., Smeed, D., Forryan, A., King, B., Sallée, J.-B., Laurent, L. S. et al. (2014). Eddy-induced variability in Southern Ocean abyssal mixing on climatic timescales. *Nat. Geo.* 7: 577–582, doi: https://doi.org/10.1038/ngeo2200.

Shi, J.-R., Talley, L. D., Xie, S.-P., Liu, W. and Gille, S. T. (2020). Effects of Buoyancy and Wind Forcing on Southern Ocean Climate Change. *J. Clim.* 33: 10003 – 10020, doi: 10.1175/JCLI-D-19-0877.1.

Shi, J.-R., Talley, L. D., Xie, S.-P., Peng, Q. and Liu, W. (2021). Ocean warming and accelerating Southern Ocean zonal flow. *Nat. Clim. Chg.* 11: 1090–1097, doi: https://doi.org/10.1038/s41558-021-01212-5.

Smith, W. H. and Sandwell, D. T. (1997). Global sea floor topography from satellite altimetry and ship depth soundings. *Science* 277: 1956–1962, doi: 10.1126/science.277.5334.1956.

Sokolov, S. and Rintoul, S. R. (2009). Circumpolar structure and distribution of the Antarctic Circumpolar Current fronts: 1. Mean circumpolar paths. *J. Geophys. Res.* 114, doi: 10.1029/2008JC005108.

Sprintall, J. (2003). Seasonal to interannual upper-ocean variability in the Drake Passage. *J. Marine Res.* 61: 27–57, doi: 10.1357/002224003321586408.

Sprintall, J. (2008). Long-term trends and interannual variability of temperature in Drake Passage. *Progr. Oceanogr.* 77: 316–330, doi: https://doi.org/10.1016/j.pocean.2006.06.004.

St. Laurent, L., Naveira Garabato, A. C., Ledwell, J. R., Thurnherr, A. M., Toole, J. M. and Watson, A. J. (2012). Turbulence and diapycnal mixing in Drake Passage. *J. Phys. Oceanogr.* 42: 2143–2152, doi: 10.1175/JPO-D-12-027.1.

Stephenson, G. R., Gille, S. T. and Sprintall, J. (2012). Seasonal variability of upper ocean heat content in Drake Passage. *J. Geophys. Res.* 117, doi: 10.1029/2011JC007772.

Stephenson, G. R., Gille, S. T. and Sprintall, J. (2013). Processes controlling upper-ocean heat content in Drake Passage. *J. Geophys. Res.* 118: 4409–4423, doi: 10.1002/jgrc.20315.

Sun, C. and Watts, D. R. (2002). Heat flux carried by the Antarctic Circumpolar Current mean flow. *J. Geophys. Res. Oceans* 107: 2–1, doi: https://doi.org/10.1029/2001JC001187.

Swart, N. C., Gille, S. T., Fyfe, J. C. and Gillett, N. P. (2018). Recent Southern Ocean warming and freshening driven by greenhouse gas emissions and ozone depletion. *Nat. Geosc.* 11: 836–841, doi: https://doi.org/10.1038/s41561-018-0226-1.

Takahashi, A. and Hibiya, T. (2019). Assessment of finescale parameterizations of deep ocean mixing in the presence of geostrophic current shear: Results of microstructure measurements in the Antarctic Circumpolar Current region. *J. Geophys. Res. Oceans* 124: 135–153, doi: https://doi.org/10.1029/2018JC014030.

Theil, H. (1992). *A Rank-Invariant Method of Linear and Polynomial Regression Analysis*. Dordrecht: Springer Netherlands. 345–381, doi: 10.1007/978-94-011-2546-8_20.

Thompson, A. F., Gille, S. T., MacKinnon, J. A. and Sprintall, J. (2007). Spatial and temporal patterns of small-scale mixing in Drake Passage. *J. Phys. Oceanogr.* 37: 572–592, doi: 10.1175/JPO3021.1.

Thompson, A. F. and Naveira Garabato, A. C. (2014). Equilibration of the Antarctic Circumpolar

Current by standing meanders. *J. Phys. Oceanogr.* 44: 1811–1828, doi: 10.1175/JPO-D-13-0163.1.

Thompson, A. F. and Sallée, J.-B. (2012). Jets and topography: Jet transitions and the impact on transport in the Antarctic Circumpolar Current. *J. Phys. Oceanogr.* 42: 956–972, doi: 10.1175/JPO-D-11-0135.1.

Tracey, K. L., Donohue, K. A., Watts, D. R. and Chereskin, T. (2013). cDrake CPIES data report. Tech. rep., GSO Tech. Rep.

Trossman, D., Waterman, S., Polzin, K., Arbic, B., Garner, S., Naveira-Garabato, A. and Sheen, K. (2015). Internal lee wave closures: Parameter sensitivity and comparison to observations. *J. Geophys. Res. Oceans* 120: 7997–8019, doi: https://doi.org/10.1002/2015JC010892.

Vallis, G. K. (2017). *Atmospheric and oceanic fluid dynamics*. Cambridge University Press.

Visbeck, M. (2002). Deep velocity profiling using lowered acoustic Doppler current profilers: Bottom track and inverse solutions. *J. Atmos. Oceanic Tech.* 19: 794–807, doi: 10.1175/1520-0426(2002)019⟨0794:DVPULA⟩2.0.CO;2.

Walkden, G. J., Heywood, K. J. and Stevens, D. P. (2008). Eddy heat fluxes from direct current measurements of the Antarctic Polar Front in Shag Rocks Passage. *Geophys. Res. Lett.* 35, doi: 10.1029/2007GL032767.

Waterhouse, A. F., MacKinnon, J. A., Nash, J. D., Alford, M. H., Kunze, E., Simmons, H. L., Polzin, K. L., St. Laurent, L. C., Sun, O. M., Pinkel, R. et al. (2014). Global patterns of diapycnal mixing from measurements of the turbulent dissipation rate. *J. Phys. Oceanogr.* 44: 1854–1872, doi: 10.1175/JPO-D-13-0104.1.

Waterman, S., Meyer, A., Polzin, K. L., Naveira Garabato, A. C. and Sheen, K. L. (2021). Antarctic Circumpolar Current impacts on internal wave life cycles. *Geophys. Res. Lett.* 48: e2020GL089471, doi: https://doi.org/10.1029/2020GL089471.

Waterman, S., Naveira Garabato, A. C. and Polzin, K. L. (2013). Internal waves and turbulence in the Antarctic Circumpolar Current. *J. Phys. Oceanogr.* 43: 259–282, doi: 10.1175/JPO-D-11-0194.1.

Waterman, S., Polzin, K. L., Naveira Garabato, A. C., Sheen, K. L. and Forryan, A. (2014). Suppression of internal wave breaking in the Antarctic Circumpolar Current near topography. *J. Phys. Oceanogr.* 44: 1466–1492, doi: 10.1175/JPO-D-12-0154.1.

Watts, D. R., Tracey, K. L., Donohue, K. A. and Chereskin, T. K. (2016). Estimates of eddy heat flux crossing the Antarctic Circumpolar Current from observations in Drake Passage. *J. Phys. Oceanogr.* 46: 2103–2122, doi: 10.1175/JPO-D-16-0029.1.

Whalen, C., Talley, L. and MacKinnon, J. (2012). Spatial and temporal variability of global ocean mixing inferred from Argo profiles. *Geophys. Res. Lett.* 39, doi: https://doi.org/10.1029/2012GL053196.

Whitworth, T. and Peterson, R. (1985). Volume transport of the Antarctic Circumpolar Current from bottom pressure measurements. *J. Phys. Oceanogr.* 15: 810–816.

Wu, L., Jing, Z., Riser, S. and Visbeck, M. (2011). Seasonal and spatial variations of Southern Ocean diapycnal mixing from Argo profiling floats. *Nat. Geosc.* 4: 363–366, doi: https://doi.org/10.1038/ngeo1156.

Xu, X., Chassignet, E. P., Firing, Y. L. and Donohue, K. (2020). Antarctic Circumpolar Current Transport Through Drake Passage: What Can We Learn From Comparing High-Resolution Model Results to Observations? *J. Geophys. Res. Oceans* 125: e2020JC016365, doi: https://doi.org/10.1029/2020JC016365.

Yang, L., Nikurashin, M., Hogg, A. M. and Sloyan, B. M. (2018). Energy loss from transient eddies due to lee wave generation in the Southern Ocean. *J. Phys. Oceanogr.* 48: 2867–2885, doi: 10.1175/JPO-D-18-0077.1.

Yang, Y. and San Liang, X. (2018). On the seasonal eddy variability in the Kuroshio extension. *J. Phys. Oceanogr.* 48: 1675–1689, doi: 10.1175/JPO-D-18-0058.1.

Youngs, M. K., Thompson, A. F., Lazar, A. and Richards, K. J. (2017). ACC meanders, energy transfer, and mixed barotropic–baroclinic instability. *J. Phys. Oceanogr.* 47: 1291–1305, doi: 10.1175/JPO-D-16-0160.1.

Zheng, K. and Nikurashin, M. (2019). Downstream propagation and remote dissipation of internal waves in the Southern Ocean. *J. Phys. Oceanogr.* 49: 1873–1887, doi: 10.1175/JPO-D-18-0134.1.